"Imperfect" Block Polymers:

Effects of Dispersity and Morphological Defects on

Block Polymer Properties

A DISSERTATION SUBMITTED TO THE FACULTY OF THE GRADUATE

SCHOOL OF THE UNIVERSITY OF MINNESOTA

BY

Hongyun Xu

IN PARTIAL FULFILLMENT OF THE REQUIREMENTS

FOR THE DEGREE OF

Doctor of Philosophy

Advisor: Mahesh K. Mahanthappa

July 2020

Acknowledgement

The Ph.D. study has been a precious experience that shaped part of my personality or even became part of me. The graduate school won't be possible at all if not with all the support from a great number of people that has helped me along the way.

First and foremost, I would like to thank my husband, En Wang. As always being one year ahead of me from undergraduate to graduate school, he provided a tremendous amount of support and guidance, as husband and coworker. I appreciate the criticism he gave as an in-field scientist and cherish the encouragement as partner. I look forward to our future to share ice-cream in summer and to overcome obstacles in life.

In terms of graduate life, I could not thank my advisor, Dr. Mahesh Mahanthappa more. His enthusiasm in science is invaluable and the width and breadth of his knowledge is always impressive. Through his mentorship, I learned many important skills from presenting a good science story to being safe in lab along the way to be a qualified scientist. While moving on to future challenges (soon), I'll definitely miss his guidance.

It has been a great experience to work in the Mahanthappa group. I want to especially thank Dr. Grayson Jackson, who helped me assembling my first Schleck line and watched me doing my first experiment. I thank Dr. Ashish Jayaraman, who defended 2 months ahead of me. After being lab mates for 5 years, I appreciate his willingness to constantly offer help and advice, and I cherish the random talks on random things that light up the day. My experience in science and graduate school can be totally different without Gray and Ashish, being the two person who know (almost) everything and willing to teach everything. I also thank all the help and kindness from our previous group members, Dr.

Tyler Mann, Dr. Sung A Kim, Dr. Carlos M. Báez-Cotto who helped me tremendously when I was starting out in lab. I thank Eric Greve, who is my collaborator and the pioneer in my first project and his detailed lab records definitely helped me to start. I thank Beth for her accompany in lab throughout the graduate years and all the beautiful dessert from her. And I wish the best to her remaining work that needs to be finished before graduation. I thank all group members Aditya Banerji, Mike Karavolias, Andreas Muller, Parth Bhide, Ankita Naik, Jack Elder, Michelle Hoard, Dr. Yongliang Zhang and Johnathan O'Donnell, who has overlapped with me for short or long times. From different backgrounds and with different cultures, I learned and benefited a lot in and out science.

I would like to thank Han Xiao and Prof. Chris Ellison, for a good time with a recent collaboration. The ideas that we generated during the meetings in Chris' office is an unforgettable memory and I cherish all the bright insights. Also, I don't know how to express my love to the polymer group in UMN, that allows me to meet and interact with so many brilliant people at one time. I thank Shuyi Xie, Dr. Piril Ertem, Aaron Lindsay, Dr. Nick Hampu, Dr. Mihee Kim, Dr. Kailong Jin, Dr. Boran Zhao, Xiayu Peng, Yangming Kou, Dr. Heonjoo Ha, Dr. Rob Hickey, Dr. Jun Xu, Dr. Tuoqi Li, Dr. Jiuyang Zhang, Dr. Dan Zhao, Dr. Qile (Paul) Chen, Athena Metaxas, Charles McCutcheon, Dr. Ron Lewis and Dr. Alice Chang for helps in various aspects during my science journey in graduate school. It always feels good to know that there are so many experts nearby on nearly anything. I appreciate the collaboration with Hongbo Chen and Prof. Calvin Sun from the Department of Pharmaceutics. This is a valuable experience to communicate with out-field experts and get a taste of a different area.

I thank the welcoming environment from the CEMS department in UMN. Integrating different cultures and diversities is more difficult to take into action than to advertise as a slogan. I appreciate all the efforts that the departments had paid to include minority voices. I would like to thank Julie Prince and Teresa Bredahl for their constant support even before I got the offer as a graduate student in UMN.

I would like to thank my parents, Yuming Xu and Hong Zhu, for supporting my decision to study abroad for 5 years. I enjoyed being close friends with my parents and I benefited a lot by exchanging opinions on almost everything and constantly getting energy from my parents. I would also like to thank my grandparents on both sides for supporting me constantly. Especially, I want to thank my grandfather, Shunlin Xu, who has become a master of remote meeting software in his eighties. I respect his ability to learn and accept new things in life.

Finally, I would like to thank my committee members, Professor Chris Ellison, Marc Hillmyer and Tim Lodge. I appreciate their feedback and guidance during my preliminary exam and over the dissertation defense.

Financial Support

We acknowledge the financial support from the University of Minnesota-Twin Cities and National Science Foundation grants DMR–1307606 and DMR–1708874. We gratefully acknowledge synchrotron small angle X-ray scattering resources at the 12-ID-B beamline of the Advanced Photon Source. The Advanced Photon Source is a U.S. Department of Energy (DOE) Office of Science User Facility operated by Argonne National Laboratory under contract no. DE-AC02-06CH11357. Some preliminary small angle X-ray scattering characterization was carried out in the Characterization Facility in University of Minnesota, which is partially supported from NSF through the MRSEC program under Award Number DMR-1420013. We also acknowledge the scanning electron microscopy offered by the Characterization Facility in University of Minnesota.

To My Family

Abstract

The chemically distinct segments of block polymers drive the formation of various microphase separated morphologies such as lamellae, cylinders packed on a hexagonal lattice and double gyroid. Previous experimental and computational studies have explored the phase behaviors of model, near-perfect block polymers with narrow molar mass distributions of the constituent blocks. However, recent reports have shown that broad block dispersity notably alters the thermodynamic phase behavior of block polymers and have explored the efficacy of using polymer dispersity to enhance performance in various applications such as nanolithography and thermoplastic elastomers. Lithium salt-doped polyether-based block polymers present an attractive system to combine desirable mechanical properties with high ionic conductivities to enable design of safe, high performance electrolytes in solid-state lithium batteries, while the effect of block dispersity in polymer electrolytes has not been studied.

In this thesis, we investigate how Li salt-doped block polymer phase behavior and ion conductivities are affected by increased dispersity in the conductive poly(ethylene oxide) (PEO) domains of poly(styrene-*block*-ethylene oxide-*block*-styrene) (bSOS) polymers. We blend a series of bSOS triblock polymers with lithium bis(trifluoromethanesulfonyl)imide (LiTFSI) and construct the corresponding morphology portraits as a function of Li^+ loading using small-angle X-ray scattering analyses. We investigate the shift of the lamellar phase boundaries and dilation of the domain spacing caused by the increased O block dispersity. We observe that bSOS affords higher ionic conductivities than the narrow dispersity diblock control samples, as characterized by electrochemical impedance spectroscopy. We

rationalize this observation based on a decreased extent of long-range ordering of the lamellar phase in the salt-doped bSOS that reduces ion diffusion pathway torturosity. In other words, the PEO domain continuity is preserved across morphological defects such as grain boundaries.

We further explore the idea of continuity through grain boundaries by successfully fabricating mechanically stable nanoporous materials by etching away the matrix domain from a cylindrical phase. We utilize polystyrene/polylactide and polyisoprene/polylactide block polymers to establish the versatility of this matrix etching method, and find that highly interconnected cylinders are present in both cases. We further assess the continuity and size selectivity of the fibril network composed of cross-linked polyisoprene through a permeation experiment as a proof-of concept for future applications as ultrafiltration membranes. This thesis provides new insights into using the ‘imperfections’ in the block polymer architecture and microphase separated morphologies to realize real-world applications as Li-ion battery electrolytes and separation membranes.

Table of Contents

List of Tables

List of Figures

List of Schemes

Chapter 1. Introduction

1.1. Block Polymer Self-Assembly

Block copolymers are comprised of two or more chemically different polymer segments covalently bonded together. The free energy penalty of mixing the monomers leads to microphase separation at length scales comparable to the radius of gyration of the macromolecules (*ca.* 5-50 nm).[1] The tendency for microphase separation is quantified by segregation strength (χN), where χ is the effective interaction parameter representing the interaction energy between dissimilar monomers and N is the normalized degree of polymerization as defined in the lattice theory.[2, 3] The nanostructured morphology with various interfacial curvature is dependent on the volume fraction of each block ($f_A = 1 - f_B$). Figure 1.1a illustrates the common self-assembled morphologies of A/B block polymers with increasing f_A, which include body-centered-cubic spheres (S), hexagonally-packed cylinders (C), double gyroid (G) and lamellae (L).[4, 5]

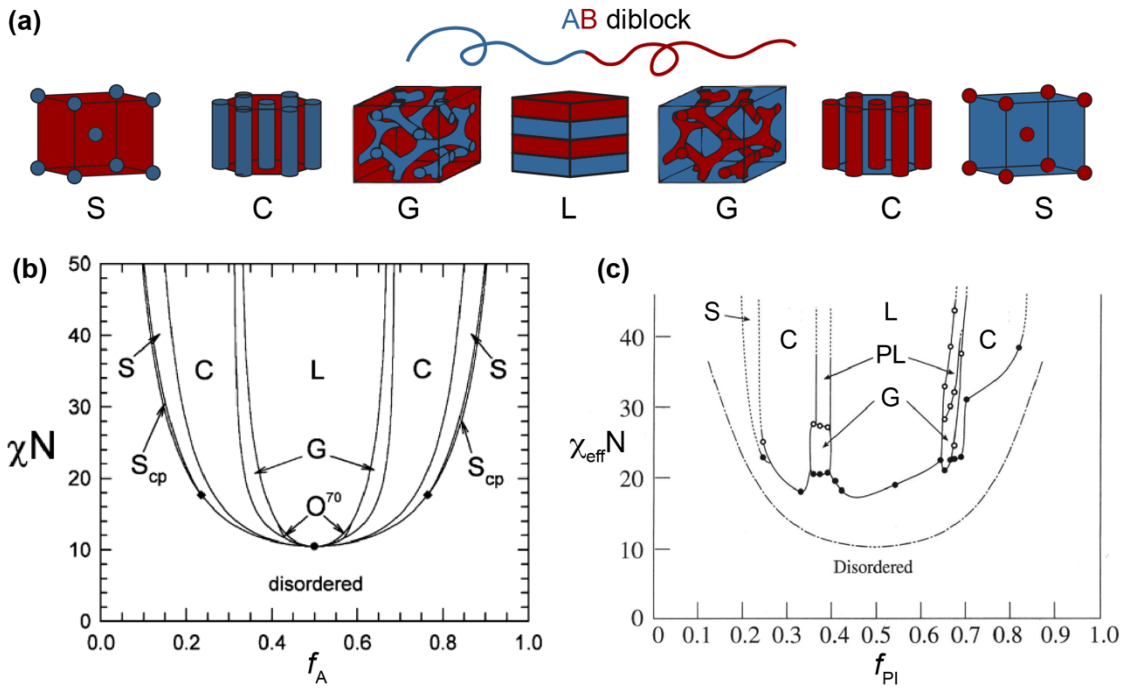

Figure 1. 1. (a) Common morphologies observed in self-assembled A/B diblock polymer: S = BCC spheres, C = hexagonally packed cylinders, G = double gyroid and L = lamellae. (b) Simulated morphology diagram of AB diblock polymer via mean-field theory, where O^{70} is the *Fddd* network phase. Reprinted (adapted) with permission from Matsen, M. W. Effect of Architecture on the Phase Behavior of AB-Type Block Copolymer Melts. *Macromolecules* **2012**, *45*, 2161–2165. Copyright (2012) American Chemical Society. (c) Experimental morphology diagram of poly(isoprene-block-styrene) diblock polymer. PL denotes the perforated lamellae network structure. The dashed line at bottom is the order-disorder transition boundary predicted by SCFT. Reprinted (adapted) with permission from Khandpur, A. K.; Förster, S.; Bates, F. S.; Hamley, I. W.; Ryan, A. J.; Bras, W.; Almdal, K.; Mortensen, K. Polyisoprene-Polystyrene Diblock Copolymer Phase Diagram near the Order-Disorder Transition. *Macromolecules* **1995**, *28*, 8796–8806. Copyright (1995) American Chemical Society.

Phase behaviors of block polymers are parameterized as functions of segregation strength (χN) and volume fraction (f). Figures 1.1B and C compare the theoretical phase diagram of "ideal" AB diblock polymers obtained from self-consistent mean-field theory (SCFT) to a representative experimental morphology diagram constructed from poly(isoprene-*block*-styrene) diblock polymers.[6, 7] While the simulation results capture most of the experimentally observed phase behaviors, a number of differences are apparent. First, the order-order (OOT) and order-disorder transition (ODT) boundaries do not exactly coincide between the theory and experiment. Compared to the symmetric phase diagram from simulation in Figure 1.1b, the phase diagram in Figure 1.1c is slightly skewed towards the lower f_{PI}, as evidenced by the position and width of the double gyroid and cylinder phase windows. Meanwhile, the critical segregation strength (χN_{ODT}) upon order-disorder transition appears at a higher value as compared to predictions from SCFT (dashed line in Figure 1.1c). The discrepancy between the experimental observations and the theoretical predictions for the poly(isoprene-*block*-styrene) system has been attributed to differences in conformational asymmetry and composition fluctuation effects near χN_{ODT}.[6, 8-11] Increased segment dispersity has been shown to affect order-order phase boundaries and order-disorder transitions,[12-14] which is a major topic to be discussed in this thesis.

Second, bicontinuous network phases has been a targeted morphology due to the desirable percolating co-continuous structure that leads to better mechanical properties and higher interconnectivity within domains. But as shown in Figure 1.1, network structures, such as the double gyroid (G), *Fddd* (O^{70}) and hexagonally perforated lamellae (PL) either form in a narrow morphology windows or are non-equilibrium morphologies due to the

significant packing frustration associated with their non-constant mean interfacial curvatures.[15, 16] On the other hand, the thermodynamically stable lamellar and cylinder phases occupy > 50 vol% of the morphology diagram, but their 1D and 2D unit cell indicates poor interconnectivity in at least one direction. In this thesis, we aim to elucidate co-continuities in lamellae and cylinder phases that are achieved through interconnected inter-grain structures, and the underestimated interconnectivity may break the barrier between network and non-network phases.

1.2. Broad Dispersity in Block Polymer Melts

When studying block polymer phase behaviors and their structure property relationships, most model systems aim to prepare block polymers with narrow dispersity, preferably by anionic polymerization such that $Đ < 1.1$. However, different polymerization methods utilized to incorporate functional monomers[17-22] and mass transport limitations during synthesis[23-25] can inherently yield broad dispersity polymers. Although block polymers with broad dispersity were believed to forbid its self-assembly, Bendejacq et al. reported well-ordered lamellae and cylinder morphologies in a series of poly(styrene-*block*-acrylic acid) PS-PAA diblock polymers with overall $Đ \gtrsim 2.0$.[26] This observation inspired studies over the past two decades to understand the impact of segmental dispersity in block polymer phase behaviors.[12-14] We first review the polymerization techniques to synthesize block polymer architectures with controllably increased dispersity.

1.2.1. Synthesis of Broad Dispersity Block Polymer Model Systems

A representative model system to study block polymer dispersity was designed by Lynd and Hillmyer, where sets of poly(ethylene-*alt*-propylene-*block*-lactide) PEP-PLA diblock

polymers were synthesized with narrowly dispersed PEP segments $Đ \leq 1.06$ and PLA of increased dispersity from 1.2 to 2.0, at the same M_n.[27-29] Utilizing the transesterification equilibrium in ring opening polymerization of lactide, the dispersities of the PLA segments progressively increased with longer reaction times. Thus, sets of block polymers with near-identical volume fractions and molecular weights but varied dispersity of the PLA block, were synthesized to systematically explore the effect of block dispersity on the diblock polymer phase behavior.

Apart from the diblock polymers with asymmetrically increased dispersity, the Mahanthappa group synthesized a series of ABA triblock polymers, containing a broad dispersity B midblock attached to narrow dispersity A blocks.[30-34] Polybutadiene (1,4-PB) with a unimodal dispersity $Đ \sim 1.8$ and well-controlled end group functionalities ($F_n \approx 2.0$) were prepared from ring-opening metathesis polymerization with the presence of symmetric chain transfer agents. From the bromo (-Br) or hydroxyl (-OH) terminated telechelic PB segments, narrow dispersity endblocks of various chemistries can be attached through controlled or living polymerization. For example, poly(styrene-*block*-butadiene-*block*-styrene) (SBS) triblock polymers were synthesized from atom transfer radical polymerization (ATRP) of styrene via bromo terminated PB center block.[30, 31] Narrow dispersity end blocks of poly(ethylene oxide-*block*-butadiene-*block*-ethylene oxide) (OBO) and poly(lactide-*block*-butadiene-*block*-lactide) (LBL) were grown from broad hydroxyl-capped PB center blocks through living anionic polymerization and ring opening polymerization respectively.[32-34] The above block polymers that paired with different end block chemistry allow exploration of the phase behaviors at different segregation strengths.

Controlled radical polymerization, which was originally developed to synthesize narrow dispersity polymers, can also be modified to access greater dispersities in block polymers.[19, 20] Ruzette et al. synthesized high molecular weight acrylic diblock and triblock polymers comprised of poly(butyl acrylate) (PBA) and poly(methyl methacrylate) (PMMA) via nitroxide-mediated polymerization.[35] In contrast to the controlled polymerization of PBA, which yields relatively narrow dispersity blocks, the PMMA macroradicals initiated from nitroxide have a greater tendency to self-terminate leading to a broader distribution in PMMA end blocks. Using activators regenerated by electron transfer (ARGET) ATRP, Listak et al. reported the synthesis of poly(styrene-*block*-methyl acrylate) diblock polymers with broad dispersed poly(methyl acrylate) (PMA) blocks.[36] By reducing the concentration of the copper catalyst from 50 ppm to 5 ppm, dispersity of the PMA segments can be increased from $Đ$ = 1.11 to 1.77 due to increased chain termination caused by insufficiency of the Cu catalyst. Apart from radical polymerizations, olefin polymerization incorporating chain shuttling agents[21, 37] or segment interchange olefin metathesis catalysts[38] has been utilized to synthesis broad dispersity olefin block polymers (OBCs). These polymerization strategies effectively broaden the selection of monomers for block polymer dispersity studies.

From the above-mentioned synthetic methods, the molar mass distributions increase symmetrically. An engineering approach was developed by Fors and co-workers to prepare broad dispersity block polymers with skewed molar mass distributions via regulated initiator addition.[23, 25, 39-41] In a living anionic polymerization, the initiator was added at a pre-programed rate to initiate monomer addition at different times. Broad dispersity

polymers with skewed dispersity to the high and low molar mass portion can be synthesized through this method, which provides another means to tailor broad dispersity block polymer phase behaviors.

Through continuous efforts to modify and combine polymerization strategies, well-controlled broad dispersity block polymers have been synthesized and reported. The model polymers with selectively increased dispersity in the midblock or endblock are especially valuable to elucidate the impact of dispersity in block polymer self-assembly.

1.2.2. Domain Dilation

Increased domain spacing with increased polymer dispersity has been reported in numerous literatures.[13, 27, 31, 33, 37, 40] These observations confirm the simulation results and have been argued to stem from 1) the synergistic packing of chains with different chain length that relieves the entropic cost of chain stretching and 2) desorption of short chains from the interface that swells the opposite domain.[42-45] For an AB diblock polymer with $Đ_A$ = 2.0, Matsen calculated the distribution of the A segments of varied chain length (σ) in the segregated domains using SCFT as shown in Figure 1.2a.[46] Figure 1.2b graphically illustrates the simulation results, where the long A segments extend to fill the spaces in the domain center, while the shorter A blocks are crowded at the interface to shield the unfavorable interactions between A/B domains.[31] This coordinated packing of broad dispersity segments enables a larger A domain without additional stretching penalties.[28, 44] Meanwhile, diblock polymers with the shortest A blocks are expelled from the interface to reside in the B domain, which is energetically favorable as these chains can relax from chain stretching at the interface.[31, 47] Figure 1.2c displays the SCFT calculation of the block

polymer free energy with varied dispersity, performed by Cooke and Shi.[45] The entropic cost to increase the domain spacing is significantly lowered at higher block dispersity, which corroborates the above mechanisms on the dilated domain size. Moreover, the reduced entropic energy with increased $Đ$ indicates that the self-assembled segments can elongate or contract more easily under deformation, which apparently makes the broad dispersity domain more elastic and leads to decreased modulus in broad dispersity polymers as reported by Fors and coworkers.[23, 48]

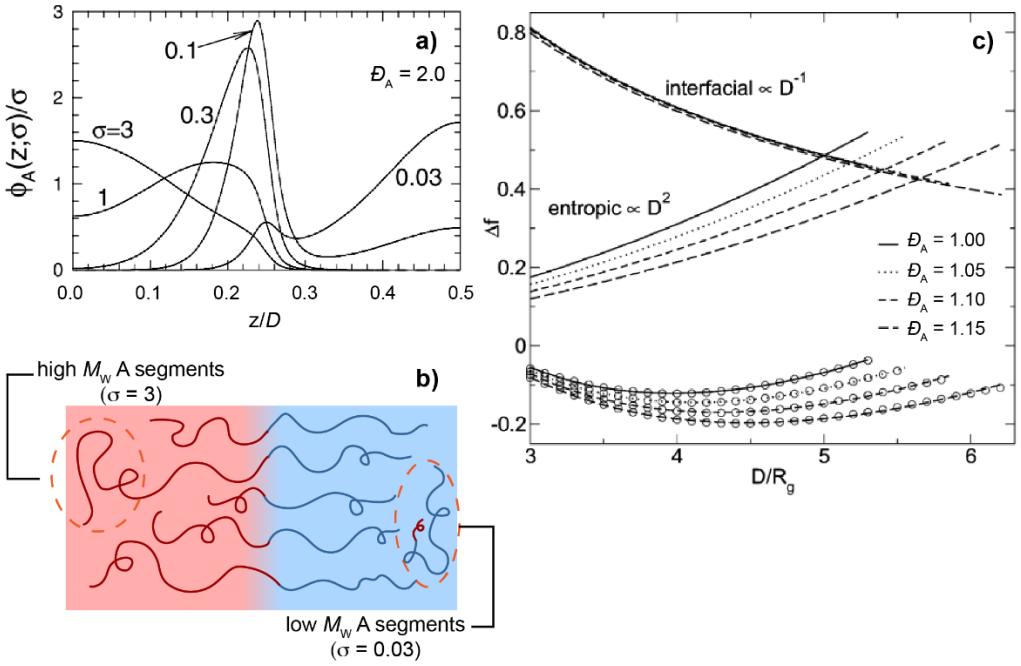

Figure 1. 2. (a) Distribution of the broad disperse A segments ϕ_A (σ, z) of various A block lengths (σ) across the domain interface where z = 0 represents the center of the A domain and z/D = ½ is the middle of the B domain, calculated based on diblock polymers with f_A = 0.50 and χN = 100 via SCFT. Reprinted by permission from Springer Nature: Springer, *The European Physical Journal E*, Effect of Large Degrees of Polydispersity on Strongly Segregated Block Copolymers, Matsen, M. W., Copyright 2006. (b) Illustration of synergistically packed broad dispersity A blocks where the high molar mass segments fill the A domain center and the short A segments are pulled out into the B domain; (c) Free energy change of self-assembled diblock polymers with increased dispersity with separated interfacial and entropic portion simulated from AB diblock polymer model with f_A = 0.35, χN = 13.5. (○) denotes simulated results and lines represent fittings to the data. Reprinted (adapted) with permission from Cooke, D. M.; Shi, A. C. Effects of Polydispersity on Phase Behavior of Diblock Copolymers. *Macromolecules* **2006**, *39*, 6661–6671. Copyright 2006, American Chemical Society.

In addition to $Đ$ of a block polymer, the extent of domain dilation can depend on other parameters. For example, the extent of domain dilation is higher at lower segregation strength (χN)[27, 49] and when molar mass distribution is skewed towards the low molecular weights.[40] Lynd and Hillmyer calculated the critical chain length (σ_{cr}) of the broadly disperse A block to lie in the B domain by balancing the increased enthalpy cost of A/B interactions versus the entropy gain from releasing the stretched polymer chain from the interface.[47] The critical chain length σ_{cr} scales to the segregation strength as $(\chi N)^{-2/3}$, implying that a larger fraction of low molar mass segments would contribute to a larger lattice spacing.

A universal model to predict the domain spacing of a broad dispersity polymer based on polymer characteristics such as molar mass distribution $Đ$ and segregation strength χN has been elusive. For example, the SBS and LBL triblock polymers reported by Widin et al.[31] and Schmitt et al.,[33] show dramatically different extents of domain dilation, even between samples at comparable segregation strength (χN ~ 25-30) with similar midblock dispersities ($Đ_B$ ~ 1.90). The SBS triblock polymers with a lower interaction parameter (χ) exhibited domain dilation of 2 ~ 2.5 times, which is similar to the 3-fold swelling reported from the olefin diblock polymers containing large $Đ$ in both domains.[37] On the other hand, lamellar *d*-spacings of the high χ/low N broad dispersity LBL triblock polymers are only ~ 3–32% higher than its narrow dispersity counterparts.[33] Similarly, PEP-PLA diblocks, reported by Lynd and Hillmyer, showed a 20-40% increase in domain size with $Đ_{PLA}$ ~ 1.8.[27] Hence, the observed domain dilation difference between the high χ *vs.* low χ block polymers is more apparent than the change of domain dilation within the same polymer

system at different segregation strength. And the large extent of swelling present in the low χ/high N polymers is beyond what predicted by most theories.[44] These discrepancies might originate from a different shape of the chain length distributions from different synthetic approaches.[44, 47] and non-Gaussian behavior of low N segments.[34, 50]

1.2.3. Shifted Morphology Boundaries and Morphology Changes

When the dispersity of one block is significantly higher than that of the other block(s), the microphase separated morphologies are found in different volume fraction ranges from their narrow dispersity counterparts. Using small-angle X-ray scattering, a comprehensive morphology diagram of broad dispersity polymers (Figure 1.3) was derived from symmetric SBS triblock polymers with a broadly disperse PB midblock.[31] The phase diagram is highly asymmetric with morphology windows skewed towards higher f_B. The lamellar phase, which is usually expected around f = 0.35–0.65 for narrow dispersity block polymers, is shifted to f_B = 0.57 – 0.75 for broad dispersity SBS polymers. A consistent trend of morphological shift to higher f_B was observed in successive studies of other broad midblock OBO and LBL triblock polymers[32, 34] and reported from several broad dispersity diblock polymers.[27, 35, 39] For example, PMMA-*b*-PBA diblock polymers with a broad dispersed PMMA block synthesized by Ruzette et al. adopt cylinder morphologies when f_{MMA}~ 0.5 and lamellae is observed with f_{MMA} > 0.60.[35]

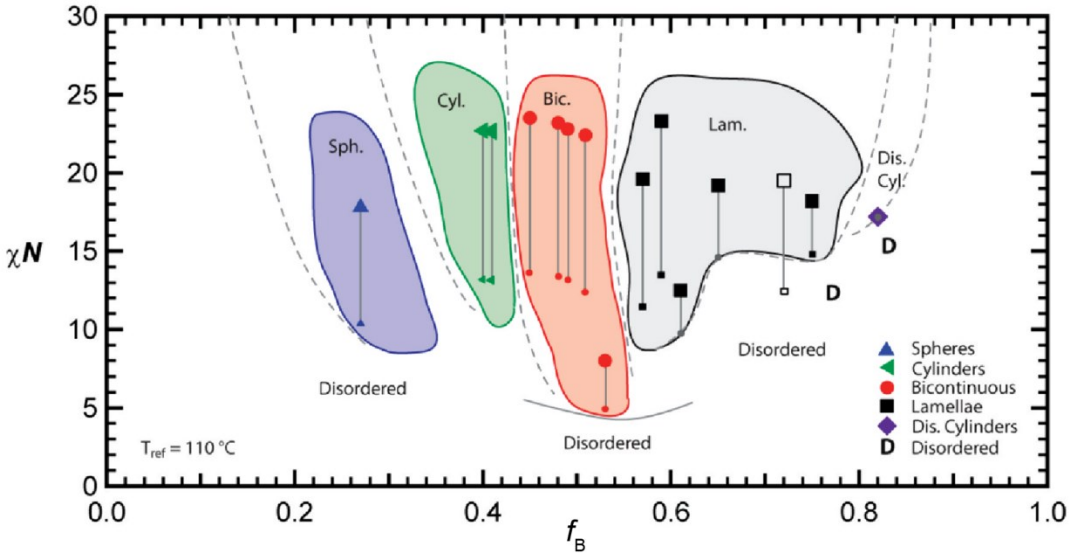

Figure 1. 3. Morphology diagram of SBS triblock polymer with broad dispersity midblock ($Đ_{PB}$ ~ 1.9) capped by narrow dispersity endblocks ($Đ_{PS}$ ~ 1.2). With increasing PB volume fraction (f_B), the progression of the morphologies is: spheres (up triangles), cylinders (left-pointed triangles), bicontinuous (circles), lamellae (squares) and cylinders with poor long-range ordering (diamonds). The gray dashed lines outline the approximate morphology boundaries. Reprinted with permission from Widin, J. M.; Schmitt, A. K.; Schmitt, A. L.; Im, K.; Mahanthappa, M. K. Unexpected Consequences of Block Polydispersity on the Self-Assembly of ABA Triblock Copolymers. *J. Am. Chem. Soc.* **2012**, *134*, 3834–3844. Copyright 2012 American Chemical Society.

Given the shifted phase boundaries to higher f_B in Figure 1.3, the microdomain with increased dispersity appears to occupy a smaller "effective" volume with preferred interfacial curvature towards the broad dispersity domain. This morphology change conforms with predictions from SCFT and Monte Carlo simulations.[43-46, 51] Figure 1.4a is a theoretical morphology diagram of a broad midblock ABA triblock polymer with $Đ_B$ =1.5 simulated from SCFT and Figure 1.4b is an equivalent morphology map showing the right shifted morphology boundaries with increased dispersity as the ordinate.[44] The mechanism of this transition is closely related to the physical picture of domain dilation as discussed in Figure 1.2. As the lower molar mass chains crowd the interface as surfactants, the relieved entropic energy in chain stretching would alter the interface to curve towards the broad dispersity domain.[31, 44, 52] An analogous example of correlated morphology shift and chain stretching is observed in conformational asymmetric narrow dispersity block polymers, where the domain interface curves towards the polymer block with higher statistical segment length (b) with lower stretching energy.[8, 9]

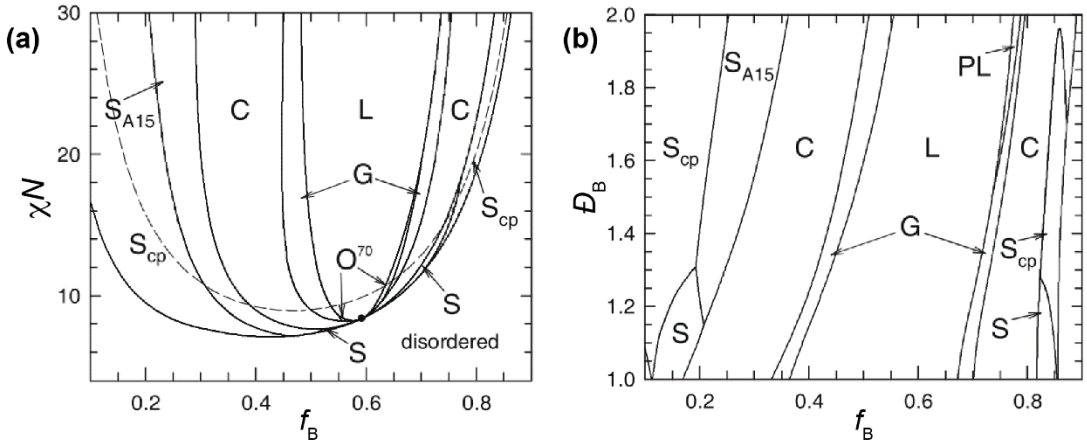

Figure 1. 4. Morphology diagrams of broad midblock ABA triblock polymer (a) with $Đ_B$ = 1.5 as a function of f_B; the dashed line represents the order-disorder boundary for monodisperse triblock polymers. (b) with increased midblock dispersity at fixed segregation strength $\chi N = 30$. The listed morphologies are BCC spheres (S), close packed spheres (S_{cp}), A15 spheres (S_{A15}), cylinders (C), gyroid (G), *Fddd* network phase (O^{70}), perforated lamellae (PL) and lamellae (L). Possibilities of forming macrophase separated two phase regions are ignored. Note that N is the degree of polymerization of half of the ABA triblock polymer ($N = N_{tri}/2$) in order to increase simulation efficiency. Reprinted by permission from Springer Nature: Springer, *The European Physical Journal E - Soft Matter*, Comparison of A-block polydispersity effects on BAB triblock and AB diblock copolymer melts, Matsen, M. W., Copyright 2013.

An intriguing observation from Figure 1.4b is an enlarged stability window of the bicontinuous network gyroid (G) with increased dispersity and the presence of another network morphology, perforated lamellae (PL) when $Đ_B \rightarrow 2.0$. These network phases are usually hard to access due to the high degree of packing frustration from the uneven domain thickness and non-constant mean interfacial curvatures.[15] Apparently, the deviation in interfacial mean curvatures can be stabilized by packing segments of different chain lengths and thus reduce the packing frustration of this network morphologies. The gyroid[27, 49] and PL[36] phases have been observed in broad dispersity diblock and triblock polymers, but they only persist in relatively small morphology windows even in broad dispersity polymers.

High molecular weight, broad dispersity block polymers also show decreased long-range order at segregation strengths comparable to their narrow dispersity homologs. Ruzette et al. observed liquid like packings of cylindrical and spherical micelles that persisted even after extended annealing of the high molecular weight, broad dispersity PBA-PMMA block polymers.[35] Apart from these classical morphologies, a disorganized bicontinuous phase (BIC), which is a disordered interpenetrating network observed in several broad dispersity block polymers. Shown in Figure 1.3, the bicontinuous morphology forms over a wide volume fraction from $f_B = 0.45–0.53$ in the SBS triblock polymers with a broad dispersity PB center block.[30, 31] The BIC phase appeared to be stable after prolonged annealing at high temperatures and attempts to induce alignment by shearing did not result in any periodic long-range order. Similar BIC structures have been reported in poly(lactide-*block*-ethylene-*block*-lactide) with a broad dispersity polyethylene midblock[53] and in blends of

poly(styrene-*block*-isoprene) diblock polymers of different molecular weights.[52, 54] Increased segmental dispersity apparently relieves the large packing frustration of the irregular BIC phase, so that it can be reproducibly accessed as a stable morphology. However, the wide BIC phase window in SBS triblock polymer is not pervasive across broad dispersity block polymers. Schmitt and Mahanthappa studied the phase behavior of high χ/low N broad midblock LBL triblock polymers and found a much smaller BIC window as shown in Figure 1.5.[34] Instead, a two-phase coexistence region of LAM and HEX, identified as intermediate phase (INT), was observed at lower segregation strength. The presence of a two-phase region is predicted by SCFT simulations as a means to relieve packing frustration by fractionating polymer chains of different molar mass to form the LAM and HEX phases, respectively.[43] The fractionation process requires diffusion of the macromolecules and thus is more kinetically feasible for low N polymer chains. Furthermore, it suggests that the BIC morphology might be a transient kinetically-trapped morphology accessible due to slow chain diffusion and implies its structural relationship to non-network structures (LAM and HEX). Apparently, the competition between thermodynamic inclination to constant interfacial curvatures and kinetic limitation that restricts fractionation of different chain lengths complicates the phase behavior of broad dispersity block polymers, but at the same time, it promotes the opportunity to access new microstructures.

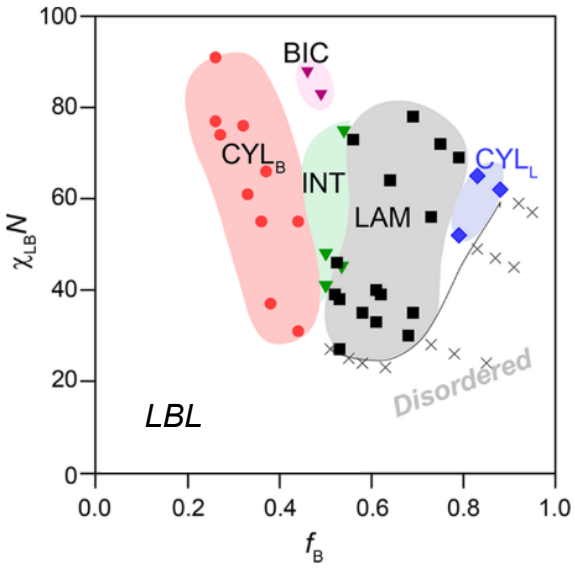

Figure 1. 5. Morphology diagram of broad midblock LBL triblock polymers, where the colored areas outline the approximate morphology boundaries. The observed morphologies are lamellae (LAM), cylinder (CYL), disorganized bicontinuous phase (BIC) and intermediate phase of LAM coexist with CYL (INT). Reprinted (adapted) with permission from Schmitt, A. K.; Mahanthappa, M. K. Order and Disorder in High χ/Low *N*, Broad Dispersity ABA Triblock Polymers. *Macromolecules* **2017**, *50*, 6779–6787. Copyright 2017 American Chemical Society.

1.2.4. Altered Order-Disorder Transition

The transition from an ordered morphology to the disorder state can be determined from the disappearance of Bragg reflection in the SAXS pattern or a steeply decreased elastic modulus of the material.[55] The change of order-disorder transition (ODT) affected by increased dispersity does not have a consistent trend and appears to be dependent on the polymer pair. The first comprehensive study of the effect of dispersity on ODT was conducted by Lynd and Hillmyer in two diblock polymer systems.[29] In a series of PS-PI diblock polymers, the change of critical segregation strength $(\chi N)_{ODT}$ with increased dispersity in PS segment ($Đ_{PS}$ = 1.04–1.21) was compared at three different volume fractions. From Figure 1.6a and b, at $f_{PS} \leq 0.51$, the decreased $(\chi N)_{ODT}$ accompanied by increased dispersity indicates that ordered morphologies are more favorable in broad dispersity polymer melts. While at $f_{PS} = 0.64$ in Figure 1.6c, the critical segregation strength does not change significantly with dispersity. Another pair of polymers with lower N, PLA-PEP, are synthesized with $Đ_{PLA}$ = 1.20–2.05 as comparison to PS-PI. In Figure 1.6d and e, for $f_{PLA} < 0.5$, $(\chi N)_{ODT}$ changes modestly with increased $Đ_{PLA}$. When $f_{PLA} = 0.64$, a more prominent increase is observed in Figure 1.6f showing that increased dispersity leads to stabilization of the disordered state. A special example of low N polymers was a series of nearly mono-disperse oligo poly(dimethylsiloxane-*block*-methyl methacrylate) diblock polymers at symmetric volume fraction ($f \sim 0.5$) prepared by Oschmann and co-workers.[56] A minimal dispersity increment from mono ($Đ = 1.00$) to narrow ($Đ \sim 1.14$) dispersity is found to lower the order-disorder transition temperature by 5–15 ºC that corroborates with a stabilized disorder state for broad dispersity low N polymers.

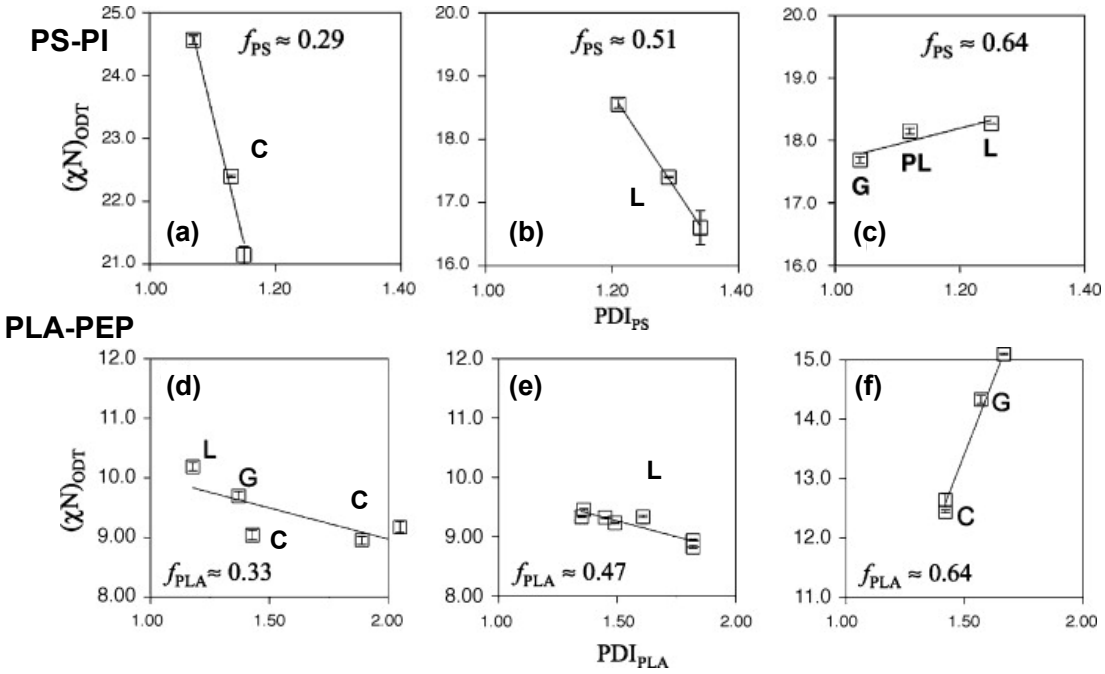

Figure 1. 6. Change of $(\chi N)_{ODT}$ as a function of (A-C) increased dispersity in PS block of the PS-PI diblock high N ($N \sim 250$) polymers and (D-E) increased dispersity in PLA segments of the PLA-PEP diblock low N ($N \sim 30$) system. The morphologies of the samples are marked in the plot where L = lamellae, C = cylinder, G = gyroid and PL = perforated lamellae. Reprinted (adapted) with permission from Lynd, N. A.; Hillmyer, M. A. Effects of Polydispersity on the Order-Disorder Transition in Block Copolymer Melts. *Macromolecules* **2007**, *40*, 8050–8055. Copyright 2007 American Chemical Society.

The effect of increased dispersity on the critical segregation strength has also been investigated for tri- and multiblock polymers. As compared to the SCFT prediction of $(\chi N)_{ODT} = 17.9$ for ABA symmetric triblock polymers at $f_B = 0.5$,[57] the critical segregation strength of SBS triblock polymers with broad dispersity PB midblock appears at a much lower value.[31] At near symmetric volume fraction ($f_B = 0.53$) with BIC morphology,

microphase separation persists even at $\chi_{SB}N$ = 4.5. For f_B = 0.61, where the ordered morphology is LAM, the critical segregation strength $(\chi_{SB}N)_{ODT}$ = 9.5, which corresponds to ~ 50% drop in comparison to the narrow dispersity counterparts. The dramatic decrease of $(\chi N)_{ODT}$ is apparent for $0.27 < f_B < 0.82$, suggesting stabilization of block polymer melts as a result of increased dispersity in the PB midblock. Similar trends were observed for an olefin multiblock polymer synthesized via chain shuttling chemistry, where microphase separation persists at low segregation strengths $(\chi N)_{eff} < 4$ in all block polymers with f = 0.36 – 0.48.[37] Contrary to what was observed in these olefin block polymers, increased $(\chi N)_{ODT}$ to 27 is observed in the high χ/low N LBL triblock polymers with midblock dispersity $Đ_{PB}$ = 1.84 at near symmetric volume fraction f_B = 0.53.[34] Figure 1.5 shows the full morphology diagram of the strongly segregated LBL triblock polymer system, where the order-disorder boundary near f_B = 0.5 ~ 0.6 is consistently higher than that for the narrow dispersity control triblock polymer system.

SCFT predicts decreased $(\chi N)_{ODT}$ over the entire composition range with increasing dispersity for both di- and triblock polymers.[44, 45, 51, 58] The dashed and the solid order-disorder boundary lines in Figure 1.7a compare the critical segregation strengths between narrow dispersity diblock and the broad dispersity counterpart with $Đ_B$ = 1.5, showing $(\chi N)_{ODT}$ drops from 10.5 to ~ 8.7 at f_B = 0.5.[43] The decreased $(\chi N)_{ODT}$ stems from the mid-high molecular weight portions in the broad dispersed polymer melt that favors microphase separation due to relieved chain stretching by synergistic chain packing. Even though the result qualitatively agrees with that observed in low χ/high N block polymers, the SCFT fails to explain the increased $(\chi N)_{ODT}$ in other high χ polymer systems. This discrepancy

originates from the assumption in SCFT that the disordered state is treated as a homogeneous mixture of A/B segments. Due to the more prominent composition fluctuations in short diblock polymers, the disordered state near ODT forms irregularly packed A-rich and B-rich domains and the packing frustration of this transient morphology is relieved by increased segmental dispersity to fit in the irregular domains.[34, 44, 51, 59] Hence, low N polymers with increased dispersity favor the disordered state as shown from an increased $(\chi N)_{ODT}$ as supported by Monte Carlo simulations in Figure 1.7b.[51]

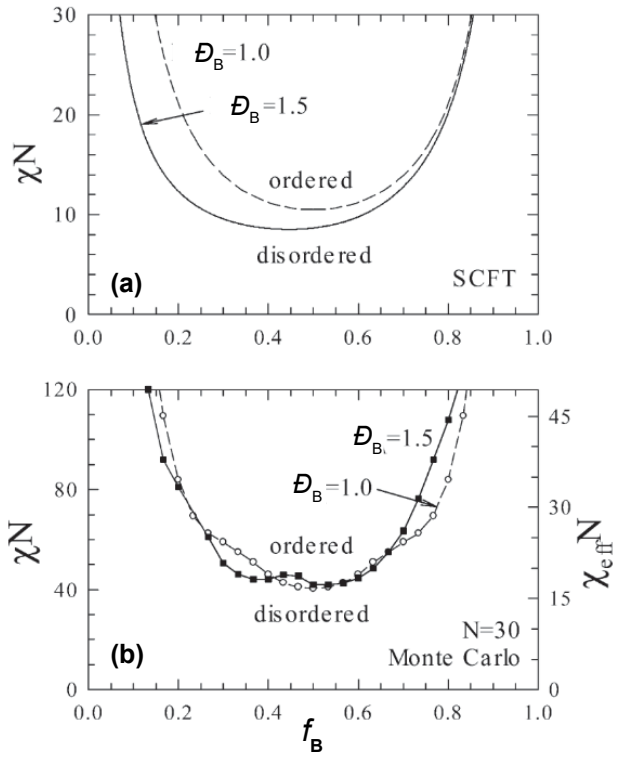

Figure 1. 7. Order to disorder transition of narrow dispersity AB diblocks (dashed line) and broad dispersity AB diblock polymers with $Đ_B$ = 1.5 (solid line) calculated by (a) mean-field theory and (b) Monte Carlo simulations. Reprinted (adapted) with permission from Beardsley, T. M.; Matsen, M. W. Monte Carlo Phase Diagram for a Polydisperse Diblock Copolymer Melt. *Macromolecules* **2011**, *44*, 6209–6219. Copyright 2011 American Chemical Society.

In summary, the χ dependent shift of $(\chi N)_{ODT}$ from broad dispersity block polymers reflects the competition between relieved chain stretching that stabilizes microphase separation in high N polymers and amplified monomer concentration fluctuation that favors disorder state in low N polymers. Although, computational studies further affirm the experimental observations, the origin of the large increase and decrease in $(\chi N)_{ODT}$

observed in the broad dispersity ABA triblock polymers and multiblock polymers remains unclear. The mean-field theory accounts for a slightly greater decrease of $(\chi N)_{ODT}$ in ABA triblock versus AB diblock with broad dispersed B chains,[43, 44] but not as significant as the drop of $(\chi N)_{ODT} < 5$ observed in the SBS and the olefin block polymers. Note that much larger domain spacings are also observed in these two low χ block polymers. These enlarged effects of broad dispersity might originate from the exact shape of the chain distribution[47] and different chain configurations (i.e. looping and bridging) in multi/tri block polymers[44] that is not fully accounted for in simulation studies.

1.3. Salt-Doped Block Polymers

The field of polymer/salt complex electrolyte was initiated from a short communication from Fenton et al. in 1973, discovering the solvation of alkali salts in polyethylene oxide (PEO).[60] This inexpensive method to prepare ion conducting polymers was the bridge between polymer science and electrochemical technologies, which innovated the design of all solid-state polymer electrolytes as safer alternatives to flammable liquid electrolytes. Currently, ignition of the volatile solvents accompanied with battery short-circuit due to the formation of lithium dendrites during repeated charge-discharge cycles hinders the commercialization of high-energy density lithium metal anodes in rechargeable battery packs.[61-65] This catastrophic battery failure hinders the commercialization of high-energy density lithium metal anodes in rechargeable battery packs. Improving the mechanical properties of the polymer electrolyte to afford a modulus comparable to lithium metal (~1 GPa) has been theoretically shown to suppress the lithium dendrite growth.[66, 67] Although the exact criteria varies with polymer system and battery operation conditions,[68-71] the

modulus of salt-doped PEO is far from meeting the requirement.[72] As lithium ions are solvated by coordinating with 5-6 oxygen sites on the PEO chains, lithium ion transport mostly relies on polymer segmental motion.[73-75] The low glass transition temperature (T_g ~ −40 ºC) of the PEO/salt complex is necessary to access practical conductivities on the order of 10^{-3} S/cm.[72, 76] Meanwhile, the dichotomy of the efficient polymer-based electrolytes is apparent as increasing the modulus to suppress dendrite growth leads to a decrease in ion conductivity due to restricted polymer chain motion.[77]

PEO-based block polymers can provide an effective route to solve this dilemma by incorporating the two orthogonal properties in disparate domains of a nanostructured electrolyte.[78-80] Poly(styrene-*block*-ethylene oxide) (SEO) doped with lithium bis(trifluoromethylsulfonyl)amide (LiTFSI) is a model system, where the salt-doped PEO domain acts as the ion-conducting channel and the glassy PS domain provides mechanical strength.[68, 69, 81-84] Due to the presence of a non-conducting block, conductivity of the block copolymer electrolyte $\sigma(T)$ relates to the PEO homopolymer conductivity $\sigma_c(T)$ as:

$$\sigma(T) = f \cdot \phi_c \cdot \sigma_c(T)$$

where ϕ_c corresponds to the conducting phase volume fraction and the entity f is the morphology factor, which specifies the influence of different morphologies on lithium ion conductive pathways. Higher f correlates with a less tortuous conductive pathway[79, 80] and ϕ_c is preferred to be $\lesssim 0.5$ to achieve better mechanical integrity so that the modulus of the polymer electrolyte is dominated by the glassy PS domain.[81] Therefore, improvements in the ion conductivity of block polymer electrolytes have been approached by increasing the

intrinsic conductivity of the salt-doped polymer $\sigma_c(T)$ or by achieving a better nanostructure with higher morphology prefactor *f*.

1.3.1. Ion Conductivity of the PEO/Salt Polymer Blend

The conductivity of PEO/LiTFSI at room temperature can be as low as 10^{-5} S/cm due to the crystallinity of the PEO that retards effective Li-ion conduction.[72] Hence, the PEO-based electrolytes are either blended with plasticizers or synthetically modified to form branched architectures to reduce the crystallinity for room temperature use.[85-88] To avoid complications of additional components and PEO crystallinity, we have limited the discussion to comparing ion conductivity of PEO/LiTFSI electrolytes at elevated temperatures ($T > T_{m,PEO}$) in the molten phase.

Lithium salt concentration is expressed as: $r = [Li^+]/[EO]$, which is the molar ratio of lithium ions to ethylene oxide monomers. The ionic conductivity of LiTFSI-doped PEO peaks near $r = 0.09$ and then drops rapidly with increased ion concentration as shown in Figure 1.8a.[72, 76] The increase of ion conductivity within $r = 0–0.09$ can be attributed to the increased effective ion concentration, while the decrement at $r > 0.09$ mainly stems from the increased glass transition temperature of the electrolyte ($T_{g,\ O/Salt}$) at large LiTFSI concentrations. Due to the transient cross-linking of the PEO segments by Li-ions, $T_{g,\ O/Salt}$ increases linearly in the range of $0.03 \leq r \leq 0.40$ that can be empirically fitted as $T_{g,O/Salt} = -51.4 + 131\ r$ (°C) and plateaus at $r > 0.40$ where LiTFSI becomes over-saturated in PEO and begins to precipitate.[76] As ion conductivity sensitively depends on the glass transition temperature of the conductive phase, a common strategy to improve $\sigma_c(T)$ is to plasticize

the PEO block with ionic liquids, oligo poly(ethylene glycol) and other compatible plasticizers.[70, 77, 85, 89, 90]

Figure 1.8b reveals that the electrolyte conductivity increases exponentially at low molecular weights, whereas it is invariant to PEO molar mass when $M_{n,\,PEO} \gtrsim 3$ kg/mol. As previously mentioned, ion diffusion in the PEO/salt complex is mainly facilitated by PEO segmental motion. At high molecular weights, the long PEO chain is almost immobilized due to entanglement and the local segmental motion is independent on chain length. For low molar mass PEO chains, diffusion of the ion complex of the entire polymer chain ("vehicular diuffsion") under an applied electric field can contribute to the total ion flux and leads to increased conductivity.[75] In a microphase separated SEO block polymer, the vehicular diffusion of the block polymer/salt complex can be ignored for all molecular weights since the PEO segments are tethered to the glassy segments at $T < T_{g,PS}$.[91]

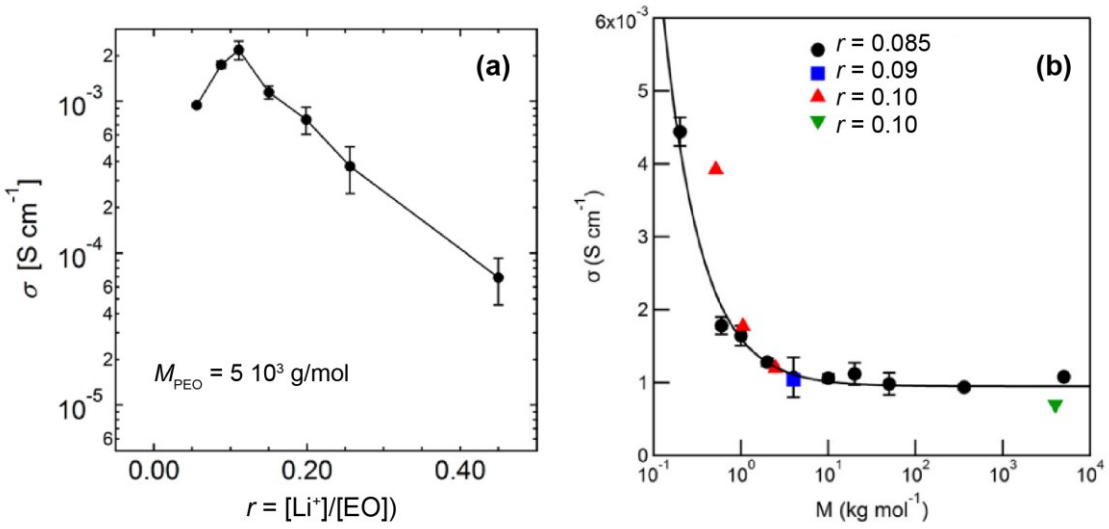

Figure 1. 8 (a) Ionic conductivity (σ) of PEO homopolymer as a function of LiTFSI salt concentration (r) at 90 ºC. Reprinted (adapted) with permission from Chintapalli, M.; Le, T. N. P.; Venkatesan, N. R.; Mackay, N. G.; Rojas, A. A.; Thelen, J. L.; Chen, X. C.; Devaux, D.; Balsara, N. P. Structure and Ionic Conductivity of Polystyrene-*block*-Poly(ethylene oxide) Electrolytes in the High Salt Concentration Limit. *Macromolecules* **2016**, *49*, 1770–1780. Copyright 2016 American Chemical Society. (b) Ionic conductivity (σ) of LiTFSI doped PEO plotted against PEO molar mass (M) at 76 ± 1 ºC with salt concentrations (r) denoted in the legend. Reprinted from *Solid State Ionics*, **2011**, *203*, Teran, A. A.; Tang, M. H.; Mullin, S. A.; Balsara, N. P., Effect of molecular weight on conductivity of polymer electrolytes, 18-21, Copyright 2011, with permission from Elsevier.

1.3.2. Change of Phase Behaviors with Ion Solvation in Block Polymers

On mixing SEO diblock polymer with LiTFSI, the lithium salt is selectively solvated in the PEO domain and thus increases incompatibility between PEO/LiTFSI and PS.[92-94] Figure 1.9 shows the transition from disordered to ordered morphologies with increased lithium salt concentration r at the same segment molar mass obtained from a SCFT calculation developed for ion-solvating block polymers.[95] The phase behavior is analogous to salt-free block polymers with except for the asymmetric shift in the morphology diagram due to the solvation of Li^+. The tendency toward microphase separation at increased salt concentration can be quantified by the change of effective interaction parameter χ_{eff} with r. Teran et al.[96] and Loo et al.[97] worked on determining χ_{eff} of LiTFSI doped O and S blocks by fitting the absolute scattering intensity profile of the disordered state obtained from SEO/LiTFSI using the random phase approximation. Using the same fitting method and the same block polymer system, these two publications derived two distinctly different expressions of salt concentration-dependent χ_{eff}. Based on a series of SEO block polymer with $\phi_c \sim 0.5$ under salt concentration range $0 < r < 0.09$, Teran and Balsara proposed the fitting of χ_{eff} as a function of diblock chain length N, temperature T and salt concentration r ($\chi_{eff} = f(N, T, r)$) and found that χ_{eff} correlates exponentially with $[Li^+]$. Loo and co-workers investigated the composition dependence of $\chi_{eff} = f(N, \phi_{PEO}, r)$ at a fixed temperature T = 100 °C of SEO diblock polymers that covers ϕ_{PEO} = 0.18 – 0.84. The researchers found that χ_{eff} only increases linearly with r within $0 < r < 0.03$.

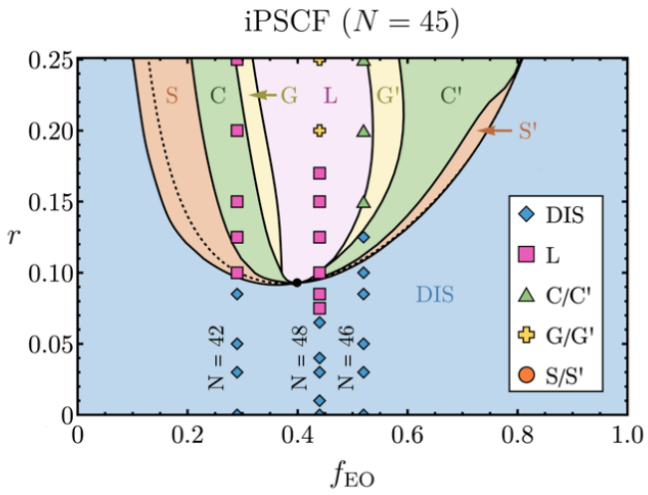

Figure 1. 9 Morphology diagram of LiTFSI doped SEO diblock polymer with increased LiTFSI salt concentration r. The colored areas are the stable morphology windows predicted from ionic polymer SCFT (iPSCF) calculation with a block polymer chain length N = 45. The symbols mark the experimentally determined morphologies with matched colors in the phase diagram. Reprinted (adapted) with permission from Hou, K. J.; Loo, W. S.; Balsara, N. P.; Qin, J. Comparing Experimental Phase Behavior of Ion-Doped Block Copolymers with Theoretical Predictions Based on Selective Ion Solvation. *Macromolecules* **2020**, *53*, 3956–3966. Copyright 2020 American Chemical Society.

Obviously, the two empirically obtained models for χ_{eff} deviate from the traditional form ($\chi = A/T + B$).[98, 99] As the fitting methodology gathers the non-idealities stemming from change in chain statistics (i.e., statistical segment length) with salt loading, the derived χ_{eff} represents more than the pure interaction energy (χ) used in the RPA theory.[1, 100, 101] Additionally, the fitting in both studies is less reliable at high salt loading ($r > 0.05$) and

high block molar mass due to limited accessibility to disorder states. Despite the shortcomings, the current χ_{eff} expressions still provide useful and usable expressions for practical salt doped S/O block polymer studies that agrees with experimental observations within certain salt concentration and volume fraction range.[102]

While the influence of preferential solvation of salt ions and increased segment dispersity on the phase behavior of block polymers has been intensively discussed, no previous study has elucidated the convoluted effect of selective solvation and broad segment dispersity. We sought to prepare a series of broad dispersity PEO with $Đ \sim 1.5$ via polycondensation of PEO oligomers that yields broad midblock poly(styrene-*block*-ethylene oxide-*block*-styrene) (bSOS) triblock polymers.[49] The bSOS polymers were blended with LiTFSI at different concentrations to access different segregation strengths. Shifted morphology diagrams to higher $f_{O/Salt}$ and dilated lamellar domain spacings are observed at all salt concentrations in accordance with the broad dispersity effect as described earlier,[31, 32, 34] suggesting the synergistic chain packing of broad dispersity segments is not affected by the presence of salt ions. The order-disorder transition of these salty bSOS polymers are found to be predominantly influenced by the salt concentration r. Using the χ_{eff} expression derived by Teran et al.,[96] we found that the critical segregation strength only marginally increased from $(\chi_{eff}N/2)_{ODT} = 10.3$ to 11.1 from $r = 0.01$ to 0.05, which is comparable the narrow dispersity counterparts. Although the high salt concentration limit resembles the high χ/low N broad dispersity polymer system, where strong fluctuation effects are expected to significantly increase $(\chi N)_{ODT}$ of the polymers, the selective solvation of ions competes to stabilize the ordered morphology and suppresses the effect of block dispersity

on the change in critical segregation strength. The detailed phase behavior of salt-doped broad dispersity SOS polymer is presented in Chapter 2.

1.3.3. Ion Conductivities of Block Polymer Electrolytes

Salt-doped block polymers that adopt the canonical morphologies such as lamellae, cylinders and gyroid are most frequently documented in literature. For each morphology, an ideal morphology factor (f_{ideal}) can be calculated based on the geometry and connectivity of the randomly oriented unit cells, which enables a quantitative comparison by which one can select the best morphology for ion conduction. Sax and Ottino used effective medium theory to calculate f_{ideal} by averaging the transport properties of randomly oriented lamellae (Figure 1.10a) and HEX grains, which yields f_{ideal} equals to 2/3 and 1/3 respectively.[103] The gyroid network seems to be the best suited morphology to simultaneously achieve good conductivity and mechanical integrity. By considering the tortuosity of the twisted gyroid cable, Shen et al. calculated the morphology factor of the gyroid phase, which equals to $f_{ideal} \approx 0.8$ when the conductive phase is the matrix and $f_{ideal} \approx 0.5$ when the conductive domain comprises gyroid cables as the minority phase.[104] Similarly, the irregular bicontinous morphology (BIC) has been shown to afford a morphology factor $f_{ideal} \sim 2/3$.[90, 105, 106] Figure 1.10b depicts a plot of f_{ideal} for different morphologies as a function of the volume fraction of the conductive phase ϕ_c.[79] To obtain structures with practically viable mechanical properties with $\phi_c \lesssim 0.5$, lamellae and BIC present the highest morphology factors.

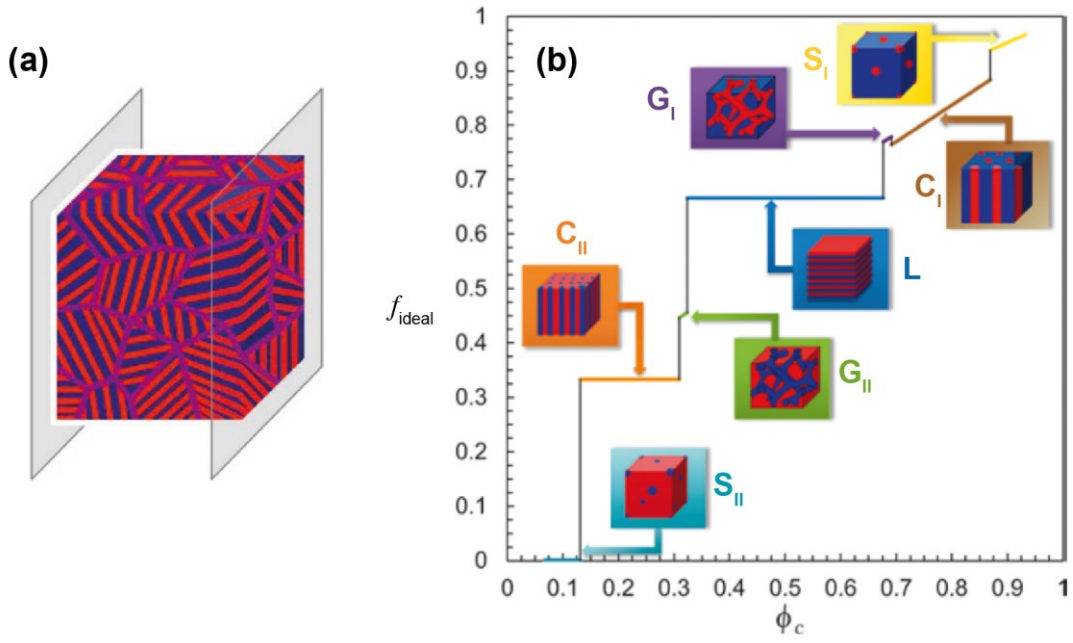

Figure 1. 10 (a) Illustration of bulk block polymer electrolyte with randomly oriented lamellar grains. (b) The ideal morphology factor (f_{ideal}) as a function of conductive phase volume fraction (ϕ_c, blue domain) with the expected morphology. Reprinted by permission from Cambridge University Press: Hallinan, D. T.; Villaluenga, I.; Balsara, N. P. Polymer and Composite Electrolytes. *MRS Bulletin* **2018**, *43*, 775–781. Copyright 2018, Materials Research Society.

For salt-doped block polymers that adopt the lamellar phase, the actual conductivity can vary due to block polymer molecular weight,[81, 82, 91] chain architecture,[107-109] or even end group chemistry.[110, 111] The experimentally derived morphology factor f of LiTFSI-doped SEO via $f = \sigma_{SEO}/(\phi_O \cdot \sigma_{PEO})$ appears much lower than f_{ideal} at low molar mass, and it increases rapidly when $M_{SEO} \gtrsim 40$ kg/mol as shown in Figure 1.11a.[82, 91] The morphology factor f does not approach f_{ideal} until the diblock molar mass reaches ~100 kg/mol. We observe similar trends in SOS triblock polymers, except that the morphology factor f increment is more abrupt with increased chain length, as compared to the SEO diblock polymers shown in Figure 1.11b. The nonideal conductivity of low molecular weight block polymers stems from two main effects. First, due to the low segregation strength at low M, ion transport can be retarded due to unfavorable contact with the insulating PS segments through interfacial mixing that can decrease ion association and ion motion at low segregation strengths.[112-116] The effect from the PS domain weakens as the interface starts to sharpen with increased segregation strengths. However, this argument fails to explain the onset of diblock polymer conductivity increment in the strongly segregated region with $M_{SEO} \sim 40$ kg/mol. Furthermore, this reasoning cannot explain the different conductivities between salt-doped SO diblocks and their equivalent triblock polymers with $M_{n,SOS} = 2\ M_{n,SO}$ as a SOS triblock polymer is conceptually analogous to two diblocks connected at the O-domain center. Chintapalli et al. first illustrated the correlation between high morphology factors and small lamellar grain sizes, that were achieved through thermal quenching and increased extent of dynamic cross-linking with increased salt concentration.[76, 117] The enhanced morphology factor f with bSOS and nSOS polymers in

Figure 1.11b is also accompanied with reduced long-range ordering due to the incorporation of broad chain dispersity and the situation of conductive segment between two glassy PS endblocks. As illustrated in Figure 1.11c, a smaller grain size effectively decreases the tortuosity of the ion diffusion route and decreases the probability of encountering dead ends, which leads to increased *f*. The above studies highlight the importance of grain structure in block polymer electrolytes, and provide a strong indication that the grain boundaries in randomly oriented lamellae are mostly continuous and conductive.

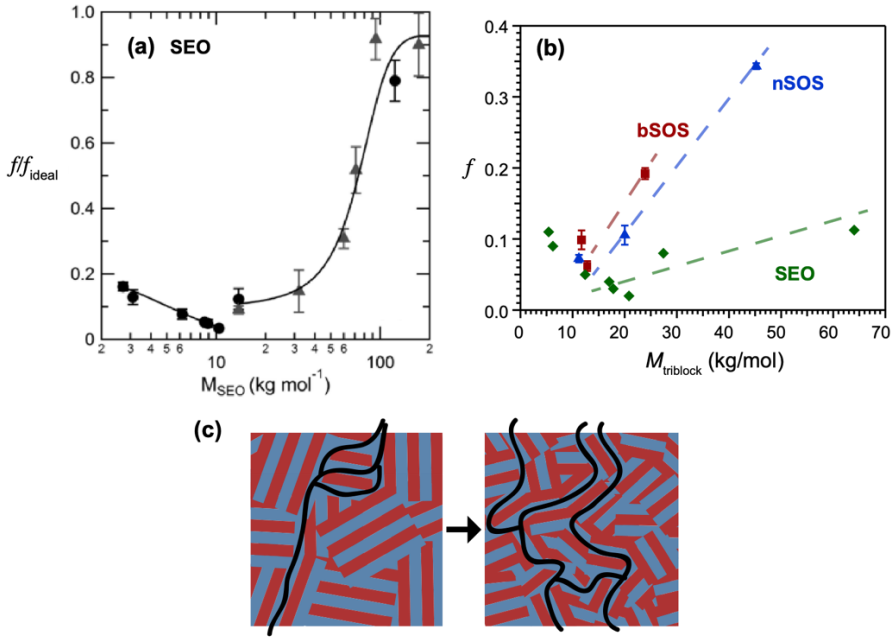

Figure 1. 11 For LiTFSI-doped S/O block polymers with $\phi_c \approx 0.5$ at $r = 0.09$, (a) morphology factor f of SEO diblock polymers plotted against the diblock molar mass (M_{SEO}) and reduced to the ideal morphology factor $f_{ideal} = 2/3$ for lamellae. Data combined results from Yuan et al.[91] (*circles*) and Panday et al.[82] (*triangles*). Reprinted (adapted) with permission from Yuan, R.; Teran, A. A.; Gurevitch, I.; Mullin, S. A.; Wanakule, N. S.; Balsara, N. P. Ionic Conductivity of Low Molecular Weight Block Copolymer Electrolytes. *Macromolecules* **2013**, **46**, 914–921. Copyright 2013 American Chemical Society; and (b) morphology factor f of bSOS (*red*), nSOS (*blue*) co-plotted with SEO (*green*), where M_{SEO} are doubled to facilitate comparisons with the triblock polymers ($M_{triblock}$) and dashed lines are intended for guide to eye. (c) Schematic of ion transport routes in a lamellar electrolyte showing enhanced interconnectivity with smaller grain size.

1.4. Domain Continuity through Grain Boundaries

The continuity across adjacent lamellar microdomains is expected from the intergrain structure. In the early 90s, Gido et al.[118, 119] and Nishikawa et al.[120] pioneered systematic characterizations of the lamellar grain boundary structures using transmission electron microscopy and categorized the most commonly observed boundary structures as twist and tilt boundaries. Twist boundaries, named after a relative rotation between adjacent lamellae, are always co-continuous as the local boundary interface adopts a Scherk's first minimal surface structure. A recent characterization by Liu et al. corroborates the continuity and local Scherk's surface from a manually fabricated 90º twist boundary by two orthogonally overlaid lamellar thin films.[121] Tilt boundaries refers to bent lamellar layers across the grain boundary, which also preserve the connectivity unless the bending angle reaches 90º. This "T" shaped junction disrupts the continuity in one domain, but it is energetically less favorable due to increased chain stretching required to fill the domain at the high tilt angle.[119] Therefore, majority of the grain boundaries in lamellae are conductive. Increasing the density of grain boundaries can effectively increase the bicontinuity such that it resembles a prototypical network morphology such as the BIC phase.

Inspired by the above observation in lamellae, we sought to probe the interconnectivity between the minority cylinders in a randomly-oriented HEX morphology. In efforts to fabricate nanoporous materials by selectively sacrificing one block from a self-assembled block polymer,[122-125] network morphologies such as gyroid[126-128] and irregular co-continuous phases[129-133] are usually preferred due to a higher void fraction and the isotropic

continuity of the resulting nanoporous structure. From this perspective, if we were to remove the matrix of a HEX morphology, the high volume fraction of the matrix domain would give rise to a higher porosity and better percolation as evident from the high morphology factor *f* in Figure 1.10b. Based on the intuitive physical picture of discrete cylinders hexagonally-arranged in space, the idea of matrix etching would likely result in a collection of nanofibrils rather than a nanoporous network.[134-137] Contrary to this conventional wisdom, we successfully fabricated a high porosity polymeric material from crosslinked polyisoprene cylinders self-assembled in an etchable polylactide matrix as shown in Figure 1.12. This observation is especially exciting since the preparation process is simple and scalable: given a block polymer of appropriate volume fraction that yields a HEX phase, the directly melt-processed polymer film or monolith is subjected to matrix etching to yield a percolating network. Supported by electron micrographs of the porous material, we attribute the retention of the fibril network to the fact that the cylinders are indeed connected through boundaries.

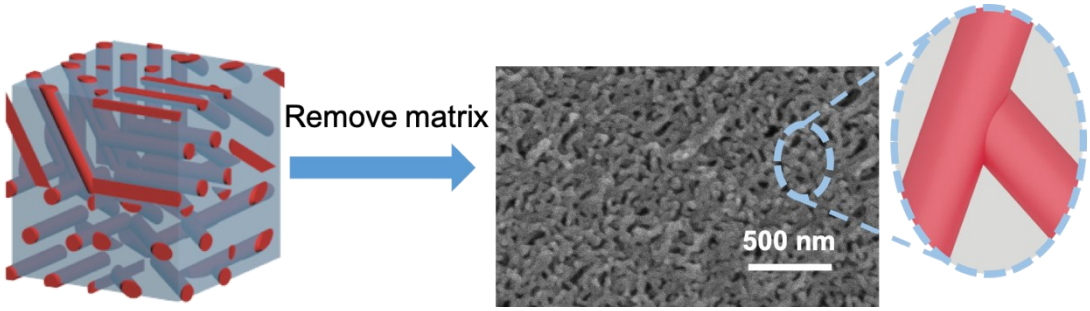

Figure 1. 12 A mechanically stable percolated nanoporous network obtained from removing the matrix domain of randomly oriented cylinder, which highlights the continuity through cylinder grain boundaries.

The conclusion of enhanced continuity through grain boundaries in both LAM and HEX phases may seem counterintuitive, especially, when aligning block polymer microdomians into a 'single crystal' presents a well-documented strategy to optimize block polymer properties. For salt-doped block polymers with lamellar morphologies, ion conductivity is shown to increase by either a significant or modest amount through preferred orientation to the direction of ion transport.[138-141] From HEX phases, ultrafiltration membranes with perpendicularly aligned pores have been successfully fabricated by etching the minority cylinders.[142-144] To bridge the seemly contradictory design criteria, the relative length scale between grain size and material dimension should not be ignored. In two-dimension thin film geometries, grain boundaries are more likely to cause deviation from the intended direction for application.[145-148] However, most macroscopic block polymer samples are comprised of randomly-oriented microdomains that are several orders of magnitude smaller than the macroscopic dimension. In this case, an increased 'defect' density would

offer desirable continuity akin to bicontinuous networks due to the interconnected nature of inter-grain structures.[76, 117, 148, 149] We anticipate that these findings will inspire new design ideas for continuous and percolating microstructures by taking advantage of the 'imperfections' of block polymer self-assembly in simple morphologies such as LAM and HEX.

Chapter 2. Morphological Impact of Segment Dispersity in Lithium Salt-Doped Poly(styrene)/Poly(ethylene oxide) Triblock Polymers[†, *]

† *Reprinted (adapted) with permission from* Xu, H.; Greve, E. M.; Mahanthappa, M. K. Morphological Impact of Segment Dispersity in Lithium Salt-Doped Poly(Styrene)/Poly(Ethylene Oxide) Triblock Polymers. *Macromolecules* ***2019****, 52,* 5722–5734. *Copyright* 2019 *American Chemical Society.*

** This work was done in collaboration with Eric M. Greve.*

2.1. Synopsis

We investigate the impact of center segment dispersity on the phase behaviors of 17 lithium salt-doped poly(styrene-*block*-ethylene oxide-*block* styrene) (bSOS) triblock polymers, in which broad dispersity O blocks ($Đ_O = M_w/M_n \approx 1.45$) are situated between narrow dispersity S segments ($Đ_S \leq 1.18$) with volume fractions $f_O = 0.33–0.69$ and total $M_n = 11.6–43.8$ kg/mol. Broad dispersity bSOS triblocks are synthesized by a tandem polycondensation and atom transfer radical polymerization (ATRP) reaction sequence. Using temperature-dependent small-angle X-ray scattering (SAXS), we map the morphology diagrams for bSOS samples variously doped with lithium bis(trifluoromethylsulfonyl)imide (LiTFSI) with r = (mol Li^+)/(mol ethylene oxide) = 0.00–0.09. As compared to the phase behaviors exhibited by 13 LiTFSI-doped, narrow dispersity SOS triblocks (nSOS) with $f_O = 0.30–0.58$ and $M_n = 7.1–45.2$ kg/mol, we demonstrate that O segment dispersity shifts the lamellar morphology window to higher

$f_{O/salt}$ and the lamellar microdomains dilate at each r-value. The critical segregation strength for microphase separation is calculated to be $(\chi N/2)_{ODT}$ = 10.3–11.1 for r = 0.01–0.05 as compared to the mean-field theory prediction $(\chi N/2)_{ODT}$ = 8.95. These findings are interpreted in terms of a competition between amplified monomer concentration fluctuations due to O segment dispersity in these high χ/low N triblocks and ordered morphologies stabilization due to preferential lithium salt solvation in the O domains.

2.2. Introduction

Block polymers afford exciting opportunities to design nanostructured materials with hybrid functionalities for established and emerging technologies, including separation membranes,[122, 150, 151] organic solar cells,[152-154] and nanolithography templates.[155-157] The microstructured morphologies of narrow dispersity A/B di- and multi- block polymers depend on volume composition ($f_A = 1 - f_B$) and the segregation strength χN, where χ is the effective segmental interaction parameter that quantifies the unfavorable A/B monomer contact energy and N is the degree of polymerization.[2, 3] Microphase separated A/B block polymers typically form lamellar (LAM), hexagonally-packed cylinders (HEX), spherical micelle packings (SPH), and bicontinuous network phases such as the double gyroid (GYR).[5, 158] For model narrow dispersity materials ($Đ = M_w/M_n \leq 1.2$), the consistency between experimental results[6, 159] and various mean-field theory calculations[7, 160, 161] enables flexible design of self-assembling A/B block polymers with high degrees of morphology control.

Over the last two decades, various reports have assessed the impacts of continuous segmental dispersity in both A/B di- and tri-block polymers on their phase behaviors as

compared to their narrow dispersity analogues.[12] These studies were spurred by the development of polymer synthesis methodologies for producing functional block polymers with variable degrees of molar mass dispersity control.[17, 18, 21, 22, 40, 162, 163] Contrary to the notion that block polymers with broad segmental dispersities exhibit molecular-level "disorder" that forbids their thermodynamically-driven self-organization,[35] these materials experimentally assemble into microphase separated morphologies with varying degrees of long-range translational order.[26-29, 31, 36, 37, 40, 164] In AB diblocks comprising narrow dispersity A segments and broad dispersity B segments, Lynd and Hillmyer documented modest shifts in the observed phase windows and changes in the composition-dependent critical $(\chi N)_{ODT}$ for microphase separation at the order-disorder transition (ODT).[12, 27-29, 47] The groups of Leibler[35] and Mahanthappa[30-34] further studied the impacts of broad A or broad B segment dispersity on the thermodynamics of ABA triblock polymer self-assembly, respectively.

Morphology diagrams for poly(styrene-*block*-1,4-butadiene-*block*-styrene) (SBS)[30, 31] and poly(lactide-*block*-1,4-butadiene-*block*-lactide) (LBL)[33, 34] triblocks with broad dispersity center segments ($Đ \sim 1.7–2.0$) exhibit both commonalties and differences in their phase behaviors. Widin *et al*. demonstrated that broad B segment dispersity in SBS triblocks lowers the critical segregation strength required for microphase separation to $(\chi N)_{ODT} \geq 4.5$ when $f_A \sim 0.5$, dilates the LAM microdomain spacing (d) by as much as two times, and shifts the LAM phase composition window to $0.55 \lesssim f_B \lesssim 0.75$.[31] In other words, the broad dispersity center segment apparently occupies a smaller than expected volume, favors interfacial curvature towards it, and stabilizes the ordered melt.[12] While the LAM

composition window is similarly shifted in high χ/low N LBL triblocks, the LAM d-spacing and minimum $(\chi N)_{ODT}$ for microphase separation exhibit different trends. Schmitt and Mahanthappa showed that disperse B segments drive only 5–32% domain dilation in LBL triblocks, with a large increase in the critical segregation strength to $(\chi N)_{ODT} \geq 27$.[33] The d-spacing differences were ascribed to segregation strength differences, while the increased $(\chi N)_{ODT}$ was rationalized in terms of dispersity-amplified monomer concentration fluctuations at low N. These studies together suggest enticing opportunities to manipulate polymer morphology and thermodynamics by segmental dispersity control.[165, 166]

Toward solvent-free, solid-state electrolytes for advanced lithium-ion batteries, Balsara and co-workers have extensively studied the phase behaviors of poly(styrene-*block*-ethylene oxide) (SO) diblock polymers doped with lithium salts.[81, 96, 167] In these SO diblocks, lithium bis(trifluoromethylsulfonyl)imide (LiTFSI) selectively partitions into the O domains and drives an overall increase in χ between the S and O/salt domains. Varying the amount of added LiTFSI in SO diblocks tunes χ over a wide range, leading to microphase separation in low N diblocks with increasing salt (*i.e.*, increasing χN).[81, 84, 92] These studies establish that variable salt doping provides a facile means for tuning segmental interaction strength in a given block polymer samples.[96] Thus, salt doping of broad dispersity block polymers offers a means for investigating apparent discrepancies in the phase behaviors of broad dispersity triblocks over a range segmental interaction strengths.

Herein, we report the syntheses and morphological studies of LiTFSI-doped poly(styrene-*block*-ethylene oxide-*block*-styrene) triblock polymers with broad dispersity O segments (bSOS) with $Đ_O = M_w/M_n \approx 1.45$ and narrow dispersity S segments ($Đ_S \leq 1.18$). Using a tandem polycondensation and atom transfer radical polymerization (ATRP) sequence, we synthesized 17 bSOS samples with $0.33 \leq f_O \leq 0.69$. Upon doping bSOS triblocks with varying amounts of LiTFSI, we mapped their morphology diagrams by temperature-dependent small-angle X-ray scattering (SAXS) as a function of Li-salt concentration. We compare these results to those from salt-doping 13 narrow dispersity SOS (nSOS) triblock control samples. These comparative studies reveal that the LAM phase window shifts to asymmetric volume compositions independent of salt-doping level, whereas the extent of LAM microdomain dilation in the bSOS samples decreases with increasing salt. Our studies further reveal that increased LiTFSI-doping of bSOS triblocks modestly increases the $(\chi N)_{ODT}$. We rationalize these findings in terms of the competing effects of O segment dispersity that amplifies monomer concentration fluctuations and ordered state stabilization by preferential ion solvation in the O domains.

2.3. Experimental Methods

Materials. All reagents were purchased from Sigma-Aldrich Chemical Co. (Milwaukee, WI) and used as received unless otherwise noted. *N,N,N',N'',N''*-pentamethyldiethylenetriamine (PMDETA), Et_3N, and 2-bromoisobutyryl bromide were stirred over CaH_2 overnight, distilled under vacuum, and stored under nitrogen. Narrow dispersity poly(ethylene oxide) (PEO) with M_n = 1.4, 3.3, 4.6, 10, 20, 31 kg/mol and respective dispersities $Đ = M_w/M_n$ = 1.12, 1.01, 1.02 1.03, 1.01, and 1.02 were freeze-dried

from C_6H_6 and stored in a glovebox under inert atmosphere. Styrene was stirred over Brockman Type I basic alumina for 1 h at 25 °C and gravity filtered to remove inhibitors immediately prior to polymerization. CuBr was purified by a literature procedure.[168] Anhydrous and anaerobic tetrahydrofuran (THF) and CH_2Cl_2 were obtained by sparging analytical grade solvent with dry N_2(g) for 30 min, followed by cycling through a column of activated molecular sieves for 12 h in a Vacuum Atmospheres Co. (Hawthorne, CA) solvent purification system.

^{1}H Nuclear Magnetic Resonance (NMR) Spectroscopy. ^{1}H NMR spectra were acquired on a Bruker Avance III HD 400 MHz spectrometer in $CDCl_3$ and referenced to the residual protiated solvent resonance (δ 7.26 ppm). Polymer ^{1}H NMR spectra were acquired with a pulse repetition delay of 10-15 s to ensure quantitative peak integration accuracy for composition analyses.

Size-Exclusion Chromatography (SEC). SEC analyses for polyether and SOS block polymers relied on an Agilent 1200 Series GPC equipped with two Viscotek I-series columns (MBMMW-3078), a Wyatt Optilab T-rEX differential refractometer, and a Wyatt DAWN HELEOS II multi-angle laser light scattering detector operating at 50 °C in *N,N*-dimethylformamide (DMF) containing 0.05 M LiBr with a flow rate of 1.0 mL/min. For each narrow dispersity sample, the refractive index increment (*dn/dc*) was calculated assuming 100% mass recovery upon sample elution. Polystyrene SEC analyses employed a Viscotek GPCMax System equipped with two Polymer Labs Resipore columns (250 mm x 4.6 mm) and a differential refractometer, running in THF at 40 °C with a flow rate of 0.8 mL/min. A polystyrene calibration curve was constructed with 10 narrow molar mass

dispersity standards with M_n = 580-377,400 g/mol from Polymer Laboratories (Amherst, MA).

Representative Synthesis of Broad Dispersity α,ω-Di(bromoisobutyryl)-Poly(ethylene oxide) Carbonate (bPEOC-Br$_2$). Freeze-dried PEO (15.00 g, M_n = 1.4 kg/mol and $Đ$ = 1.12, 10.7 mmol) and NaH (60 *wt*% dispersion in mineral oil, 0.0436 g, 10.9 mmol) were combined in a 100 mL Schlenk tube in a glovebox. Outside of the glovebox on a vacuum line, diallyl carbonate (4.5 mL, 31.4 mmol) was added to the flask by syringe and a water-cooled distillation head with receiving flask was attached under a N_2(*g*) flush. The reaction tube was heated to 120 °C for 2 h under atmospheric pressure, after which the pressure was carefully reduced to 0.08 Torr and the reaction temperature was increased to 180 °C. The receiving flask was then chilled using a dry ice/2-propanol bath to condense the C_3H_5OH reaction byproduct and unreacted diallyl carbonate. The condensation reaction was continued for 20 min under these conditions. The resulting polymer was dissolved in CH_2Cl_2 (50 mL), precipitated into Et_2O (500 mL) twice, and dried under vacuum. $M_{n,\,SEC}$ = 13.5 kg/mol, $Đ$ = 1.56 and $M_{n,\,NMR}$ = 14.0 kg/mol.

The allyloxycarbonyl end groups of the resulting α,ω-diallylpoly(ethylene oxide) carbonate (5.00 g, 14.0 kg/mol, 0.36 mmol) were removed by treatment with $Pd(PPh_3)_4$ (0.0430 g, 0.037 mmol), PPh_3 (0.0385 g, 0.147 mmol) and 95 wt% formic acid (260 μL, 6.5 mmol) in anaerobic THF (150 mL) at 22 °C for 4 h.[169] Following solvent removal by rotary evaporation, the resulting α,ω-dihydroxy-poly(ethylene oxide) carbonate was redissolved in CH_2Cl_2 (50 mL), precipitated in Et_2O (500 mL) twice, and freeze-dried from minimal C_6H_6 to remove residual water.

The resulting α,ω-di(hydroxy)-poly(ethylene oxide) carbonate (bPEOC) was dissolved in anhydrous CH_2Cl_2 (80 mL) and reacted with an excess of α-bromoisobutyryl bromide (270 μL, 2.2 mmol per –OH end group) and Et_3N (350 μL, 2.5 mmol per –OH end group). After solvent removal by rotary evaporation, the reaction mixture was redissolved in C_6H_6, filtered through a plug of Brockman Type I basic alumina, and precipitated into cold hexanes twice (500 mL). The resulting solids were freeze-dried from C_6H_6 to yield **bPEOC-Br$_2$**. $M_{n,\,SEC}$ = 12.8 kg/mol, $Đ$ = 1.48 and $M_{n,\,NMR}$ = 12.5 kg/mol.

Narrow dispersity α,ω-di(bromoisobutyryl)-poly(ethylene oxide) telechelics (**nPEO-Br$_2$**) were prepared from commercial, narrow dispersity PEO as previously reported.[170]

Representative Synthesis of bSOS Block Polymers. In an oven-dried 100 mL Schlenk flask, a mixture of styrene (30 mL, 262 mmol) and PMDETA (140 μL, 0.67 mmol) was subjected to three freeze-thaw degassing cycles. During the third freezing step, CuBr (0.096 g, 0.67 mmol) was quickly added to the frozen mixture under a flush of $N_2(g)$, after which the final evacuation and thaw cycle were completed. This mixture was stirred at 45 °C for 1 h under $N_2(g)$ to form the Cu-catalyst complex. 4.3 mL of this solution was added by syringe to a 25 mL Schlenk tube charged with **bPEOC-Br$_2$** (0.296 g, 0.0237 mmol) under $N_2(g)$ at 22 °C. The Schlenk tube was then heated to 90 °C in an oil bath. After 120 min, the reaction was stopped by cooling the Schlenk tube under cold running water. The reaction product was precipitated into rapidly stirred CH_3OH (20 mL) and stirred for 1 h. Residual solvent was removed from the solids by rotary evaporation, after which they were dissolved in CH_2Cl_2 (5 mL), eluted through a short plug of basic $Al_2O_3(s)$ to remove Cu-

catalyst residues, and precipitated into hexanes (30 mL). The isolated bSOS was freeze-dried from C_6H_6 and stored in a glovebox.

Narrow dispersity nSOS triblock polymers were similarly synthesized from **nPEO-Br$_2$.**

Representative SOS Block Polymer Degradation. bSOS_23.9_0.51 (50 mg) was dissolved in THF (0.5 mL) and treated with 2.5 M KOH in 50% *v*/*v* THF/ CH_3OH (2 mL). After reaction at 40 ºC for 12 h, the solution was precipitated into CH_3OH (10 mL) to isolate the S homopolymer. The solid polymer was freeze-dried from C_6H_6. $M_{n,SEC}$ = 5.4 kg/mol, $Đ$ = 1.11 (versus PS standards), and $M_{n,\,NMR}$ = 5.6 kg/mol.

Sample preparation. Block polymer samples (~30 mg) were dissolved in CH_2Cl_2 (0.5 mL), and measured amounts of LiTFSI in a 10% *v*/*v* solution THF/CH_2Cl_2 were added to achieve the desired r = [LiTFSI]/[EO units] based on M_n for each sample. Each solution was homogenized by sonication for 5 min and solvent cast into hermetic aluminum DSC pan bottoms (TA Instruments, Newcastle, DE) at 60 ºC. Samples were then heated to 140 °C under vacuum for 12 h to effect residual solvent and moisture removal, after which the DSC pans were hermetically sealed with the corresponding lids in a glovebox with [H_2O] ≤ 1 ppm.

Small Angle X-Ray Scattering (SAXS). Synchrotron SAXS measurements were conducted at the 12-ID-B beamline of the Advanced Photon Source (Argonne, IL). Using an incident beam energy of either 13.3 keV or 14.0 keV and a 3.605 m sample–to–detector distance, 2D–SAXS patterns were recorded on a Pilatus 2M area detector (25.4 cm × 28.9 cm active area with 1475 × 1679 pixel resolution) using exposure times of ~1 s. Block polymer samples were thermally equilibrated at each desired temperature in a multi-array

sample stage for at least 10 min prior to X-ray analysis. All SAXS patterns were calibrated using a silver behenate standard (d = 58.38 Å), and reduced one-dimensional intensity $I(q)$ versus scattering wavevector q profiles were obtained using data reduction tools available at the beamline.

2.4. Results & Analysis

2.4.1. Synthesis and Molecular Characterization of bSOS

Unimodal bSOS triblock polymers with broad dispersity O segments were synthesized by a tandem polycondensation/atom transfer radical polymerization sequence (Scheme 2.1a and Figure 2.1a). By analogy to a reported polycarbonate synthesis,[171] condensation polymerization of an oligo(ethylene oxide) (M_n = 1.4 kg/mol) with diallyl carbonate catalyzed by NaH produced broad dispersity α,ω-diallylpoly(ethylene oxide) carbonates with reaction time-dependent M_n values. The allyloxycarbonyl polymer end groups were removed by Pd(0)-catalyzed hydrogenolysis with HCOOH to furnish α,ω-dihydroxy-poly(ethylene oxide) carbonate (bPEOC).[169] Esterification of bPEOC with α-bromoisobutyryl bromide yielded **bPEOC–Br$_2$** with M_n = 5.7–14.8 kg/mol and $Đ$ = 1.43–1.48. Number-average molecular weights calculated from ^{1}H NMR end group analyses concur with those obtained from SEC (within 15%), indicating a high degree of telechelic chain end functionality.[17] **bPEOC–Br$_2$** telechelics served as macroinitiators for (PMDETA)CuBr–catalyzed ATRP of styrene at 90 ºC to yield unimodal yet broad dispersity bSOS (Figure 2.1a). Block polymer compositions and polystyrene end segment molar masses were determined by quantitative ^{1}H NMR analyses based on the O midblock M_n's. Alkaline degradation of the bSOS triblocks with KOH in THF/CH_3OH (50:50 *v/v*) at

40 °C further enabled isolation and direct SEC characterization of the S end block M_n and $Đ$ (see Figure 2.1a for SEC trace overlay). By this method, we found that the S segments exhibit $Đ \leq 1.18$ and that the molar masses deduced by ^{1}H NMR and SEC agree within ~10%. Taken together, these data suggest the absence of unreacted bPEOC or any broad dispersity SO diblock contaminants.

The molecular characteristics of the bSOS triblock polymers produced by the above method are summarized in Table 1. Volume fractions for neat bSOS were calculated using the homopolymer melt densities ρ_{PS} = 1.032 g/cm^3 and ρ_{PEO} = 1.073 g/cm^3 at 90 ºC.[172] Note that our use of the latter homopolymer melt density for PEO neglects the presence of carbonate linkages in the **bPEOC** (≤ 5.5 wt% per chain). The segment density-normalized degree of polymerization (N) based on a reference volume V_{ref} = 0.1 nm^3 was calculated as:[44]

$$N = \left(\frac{M_{n,\,PEO}}{\rho_{PEO}} + 2\frac{M_{n,\,PS}}{\rho_{PS}}\right)\Big/ N_A V_{ref}$$

where N_A is Avogadro's number. Samples are identified as bSOS_x_y, where x is the total $M_{n,SOS}$ (kg/mol) for the triblock and y is the O midblock volume fraction. Narrow dispersity SOS triblock polymers (nSOS) were synthesized via analogous Cu-mediated ATRP from narrow dispersity **nPEO-Br$_2$** (Scheme 2.1b). SEC characterization (Figure 2.1b) established the narrow dispersities of all constituent segments in these nSOS samples, for which molecular characteristics are also provided in Table 2.1.

Scheme 2. 1. Syntheses of (a) bSOS Triblock Polymers via Tandem Polycondensation and ATRP and (b) nSOS Triblocks by ATRP.

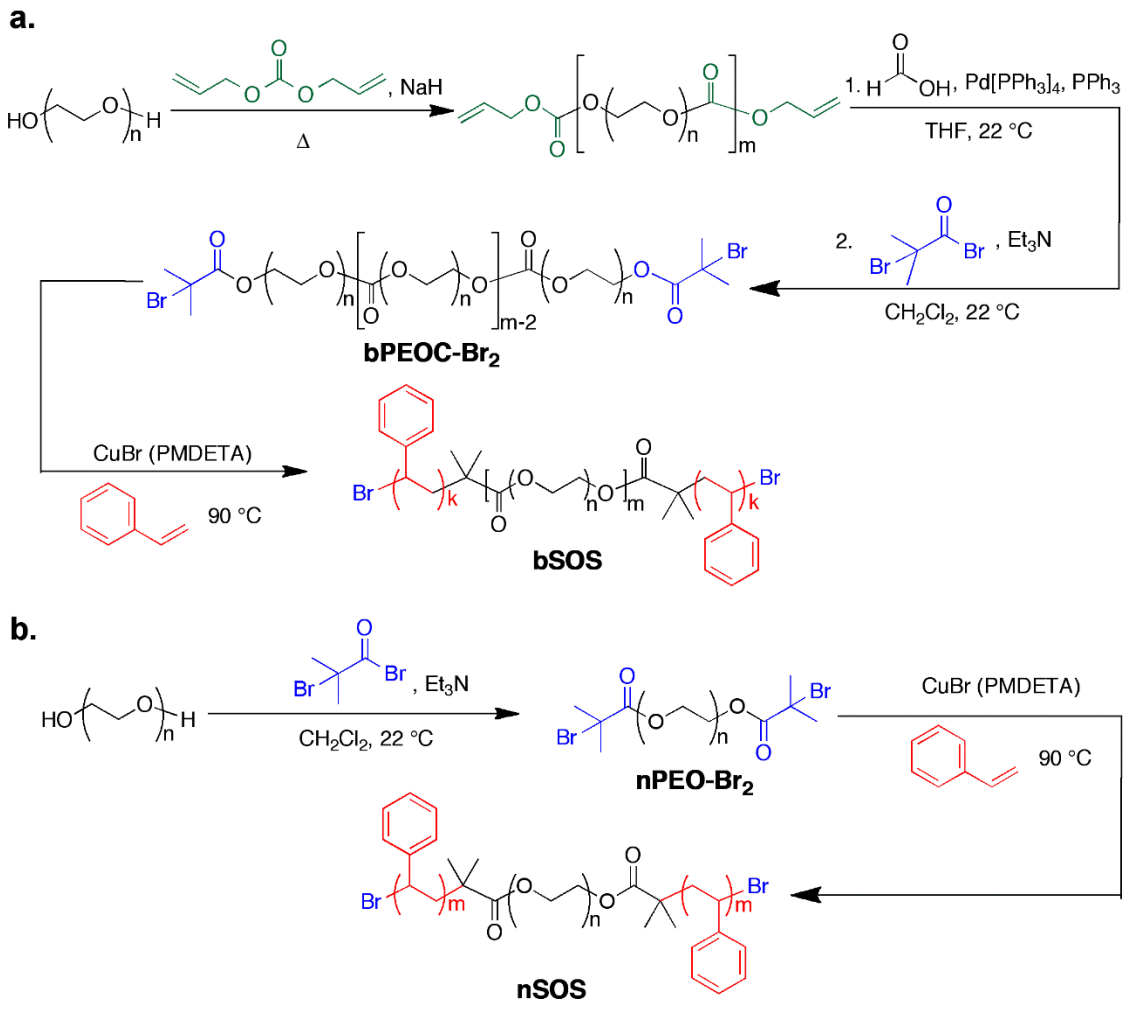

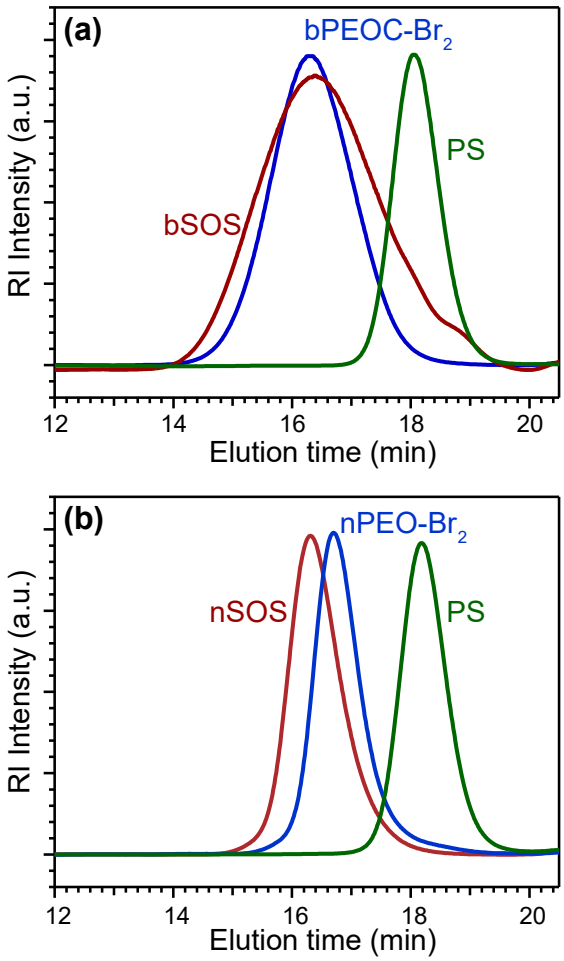

Figure 2. 1. Representative SEC traces for (a) bSOS_23.9_0.51 and (b) nSOS_20.0_0.49 triblock polymers (*red*), the **bPEOC-Br$_2$** or **nPEO-Br$_2$** from which they derive (*blue*), and the PS homopolymer end segments derived from center block degradation (*green*).

Table 2. 1. Molecular Characteristics of bSOS and nSOS Triblock Polymers.

		O midblock		S endblock		Block Polymer	
Sample	$M_{n\ SOS}$[c]	$M_{n,NMR}$[a]	$Đ_{PEO}$[b]	$M_{n,NMR}$[c]	$Đ_{PS}$[d]	f_{EO}	N[e]
bSOS_43.8_0.33	43.8	14.8	1.45	14.5	1.12	0.33	696
bSOS_36.9_0.33	36.9	12.5	1.48	12.2	1.10	0.33	586
bSOS_32.9_0.37	32.9	12.5	1.48	10.2	1.12	0.37	522
bSOS_14.9_0.37	14.9	5.7	1.43	4.6	1.15	0.37	236
bSOS_38.0_0.38	38.0	14.8	1.45	11.6	1.13	0.38	603
bSOS_30.9_0.40	30.9	12.5	1.48	9.2	1.11	0.40	490
bSOS_11.7_0.48	11.7	5.7	1.43	3.0	1.18	0.48	185
bSOS_23.9_0.51	23.9	12.5	1.48	5.7	1.11	0.51	377
bSOS_23.2_0.52	23.2	12.4	1.48	5.4	1.13	0.52	366
bSOS_12.8_0.54	12.8	7.0	1.45	2.9	1.13	0.54	202
bSOS_12.2_0.56	12.2	7.0	1.45	2.6	1.14	0.56	192
bSOS_20.9_0.59	21.5	12.5	1.48	4.5	1.14	0.59	329
bSOS_24.8_0.59	24.8	14.8	1.45	5.0	1.15	0.59	390
bSOS_11.6_0.59	11.6	7.0	1.45	2.3	1.12	0.59	182
bSOS_19.6_0.62	19.6	12.4	1.48	3.6	1.13	0.62	308
bSOS_18.4_0.67	18.4	12.4	1.48	3.0	1.12	0.67	289
bSOS_21.2_0.69	21.2	14.8	1.45	3.2	1.15	0.69	332
nSOS_15.0_0.30	15.0	4.6	1.02	5.2	1.13	0.30	239
nSOS_12.8_0.35	12.8	4.6	1.02	4.1	1.11	0.35	203
nSOS_11.8_0.38	11.8	4.6	1.02	3.6	1.12	0.38	187
nSOS_11.2_0.40	11.2	4.6	1.02	3.3	1.13	0.40	177
nSOS_23.2_0.42	23.2	10.0	1.03	6.6	1.12	0.42	367
nSOS_45.2_0.43	45.2	20.0	1.01	12.6	1.14	0.43	715
nSOS_22.0_0.44	22.0	10.0	1.03	6.0	1.11	0.44	348
nSOS_7.1_0.46	7.1	3.3	1.03	1.9	1.11	0.46	112
nSOS_42.6_0.46	42.6	20.0	1.01	11.3	1.12	0.46	673
nSOS_20.0_0.49	20.0	10.0	1.03	5.0	1.12	0.49	316
nSOS_19.0_0.52	19.0	10.0	1.03	4.5	1.12	0.52	300
nSOS_8.4_0.54	8.4	4.6	1.02	1.9	1.16	0.54	132
nSOS_7.8_0.58	7.8	4.6	1.02	1.6	1.14	0.58	122

[a] Determined by quantitative end group analysis by ^{1}H NMR spectroscopy. [b] SEC in 0.05 M LiBr in DMF at 50 °C using dn/dc = 0.043 mL/g for **bPEOC-Br$_2$** and dn/dc = 0.042 mL/g for **nPEO-Br$_2$**. [c] Determined by quantitative ^{1}H NMR spectroscopy based on $M_{n,O}$. [d] Obtained by SEC in THF at 40 ºC versus narrow dispersity S homopolymer standards. [e] Calculated from neat polymer segment densities at 90 ºC using the reference volume V_{ref} = 0.1 nm^3.

2.4.2. Morphologies of Neat bSOS Triblocks

We first characterized the neat bSOS sample morphologies by SAXS between T = 22–150 °C. Salt-free bSOS samples with M_n < 25 kg/mol do not melt microphase separate, as only correlation-hole SAXS peaks were observed (Figure 2.2a).[173] When M_n > 30 kg/mol in the range f_O = 0.33–0.38, bSOS samples exhibit poorly ordered, microphase separated morphologies exemplified by the 1D-SAXS intensity profile for bSOS_38.0_0.38 at 22 °C (Figure 2.2a). This last sample appears to be microphase separated when T < 120 °C, since heating it to 120 °C leads to the disappearance of the broad, higher order reflections in a manner consistent with an order-disorder transition (see Appendix Figure A1.1). The broad, higher order peaks observed in these samples are located at (q/q^*) = √1, √3, √4, √7, and √9 (q^* = 0.020 Å^{-1}), consistent with poorly ordered, hexagonally-packed O cylinders in an S matrix (CYL_O). The observed peak breadths suggest poor translational order, analogous to that exhibited by broad dispersity block polymers with high M_n values.[31, 34, 174] The phase behaviors of the salt-free bSOS samples are compiled in the N versus f_O morphology diagram presented in Figure 2.2b.

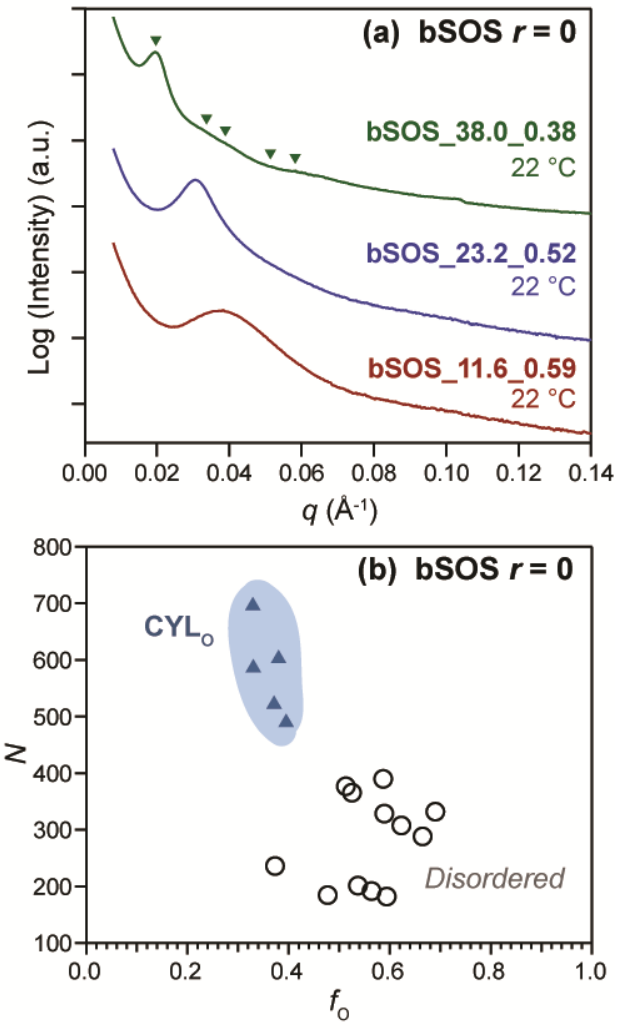

Figure 2. 2. (a) 1D-SAXS profiles for neat bSOS triblock polymers, and (b) a bSOS morphology map for samples listed in Table 2.1 at $T = 90$ °C, where open circles (⚬) denote samples that are melt-disordered, solid triangles (▲) indicate ordered CYL_O samples.

2.4.3. Morphologies of LiTFSI-doped bSOS

The morphologies of bSOS triblocks doped with varying amounts of LiTFSI were also characterized by temperature–dependent synchrotron SAXS. Per the report of Teran and Balsara,[96] the volume fraction of the O/LiTFSI microphase was calculated as:

$$f_{\mathrm{O/salt}} = \frac{\frac{M_{\mathrm{n,\,PEO}}}{\rho_{\mathrm{PEO}}} + r\frac{M_{\mathrm{n,\,PEO}}}{M_{\mathrm{EO}}}\frac{M_{\mathrm{LiTFSI}}}{\rho_{\mathrm{LiTFSI}}}}{\frac{M_{\mathrm{n,\,PEO}}}{\rho_{\mathrm{PEO}}} + r\frac{M_{\mathrm{n,\,PEO}}}{M_{\mathrm{EO}}}\frac{M_{\mathrm{LiTFSI}}}{\rho_{\mathrm{LiTFSI}}} + 2\frac{M_{\mathrm{n,\,PS}}}{\rho_{\mathrm{PS}}}}$$

where $r = [Li^+]/[EO]$, M_{EO} and M_{LiTFSI} are the respective molar masses of ethylene oxide (44.05 g/mol) and LiTFSI (287.09 g/mol), and $\rho_{LiTFSI} = 2.023$ g/cm^3 is the effective LiTFSI density. This expression assumes complete segregation of LiTFSI into the O domains, as a consequence of polyether ligation to Li^+ and preferential anion solvation therein.[92, 94]

Minimal LiTFSI-doping at $r = 0.01$ significantly alters the melt self-assembly behavior of bSOS. In the range $f_{O/salt} = 0.33$–0.41 with $M_n \gtrsim 30$ kg/mol, SAXS analyses of the salt-doped bSOS (Figure 2.3a) reveal broad peaks possibly consistent with a hexagonally-packed cylinders (CYL) morphology. Increasing the volume fraction to $f_{O/salt} = 0.53$ yields a SAXS signature consistent with a double gyroid (GYR) morphology with peaks corresponding to the (211), (220), (321), (400), (420), (332), and (422) reflections with a lattice parameter $a = 53$ nm ($q_{(211)} = 0.029$ Å^{-1}). This observation constitutes the first report of a GYR morphology in any broad dispersity triblock polymer.[31, 32, 34] When $f_{O/salt} = 0.55$–0.70, high molar mass bSOS samples exhibit sharp primary SAXS peaks (q^*) with a higher order reflection at $2q^*$ (Figure 2.3a), which we identify as lamellae (LAM). Only the two samples with $M_n = 19.6$ and 21.2 kg/mol ($N = 308$ and 332) in this composition range at $r = 0.01$ exhibit accessible order-disorder transition temperatures $T_{ODT} = 139$ °C and 111 °C,

respectively. Samples with M_n < 19 kg/mol (N < 300) display only the broad correlation-hole scattering of a disordered morphology. The phase sequence CYL ➞□GYR ➞□LAM suggests that the GYR phase comprises LiTFSI-doped O cables in a S matrix (GYR_O), in spite of its occurrence at the majority salt volume fraction $f_{O/salt}$ = 0.53. These morphology data are summarized in Figure 2.3b.

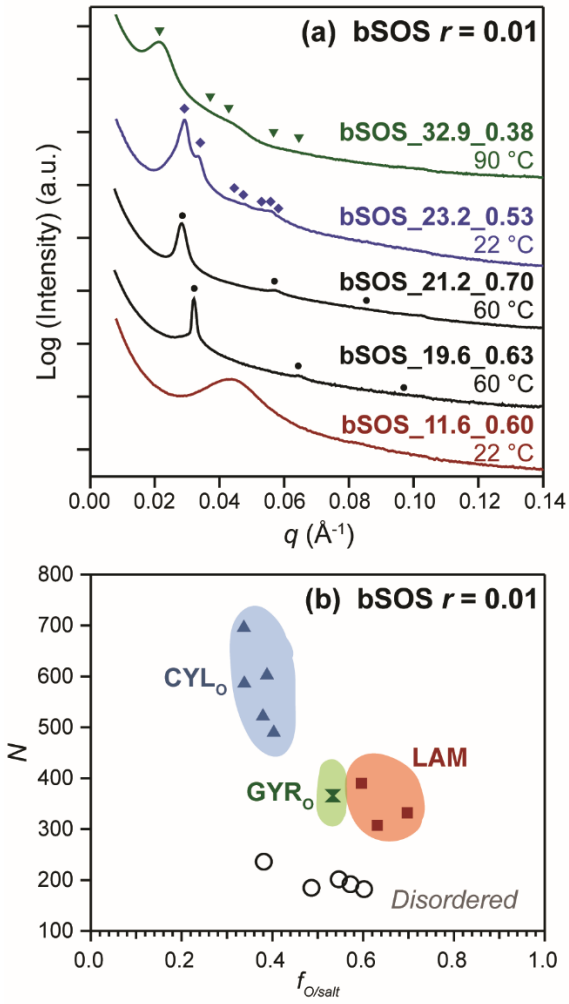

Figure 2. 3. (a) Synchrotron SAXS intensity profiles for representative LiTFSI-doped bSOS triblock polymers with r = 0.01, in which symbols demarcate the calculated peak positions for CYL_O (*triangles*), GYR_O (*diamonds*), and LAM (*circles*). The peak at q = 0.104 $Å^{-1}$ is an artifact associated with the detector mask. (b) A morphology diagram summarizing the results of SAXS characterization of 14 salt-doped bSOS samples with r = 0.01 at T = 90 °C, where the colored regions are intended only to guide the eye and do not represent exact phase boundaries.

The somewhat surprising occurrence of GYR_O at $f_{O/salt}$ = 0.53 led us to investigate the phase behaviors of nSOS control samples with comparable molecular weights. We synthesized nSOS per Scheme 2.1b, and nSOS molecular characterization data are given in Figure 2.1b and Table 2.1. SAXS data for selected samples at r = 0.01 provided in Figure 2.4a show that the narrow dispersity nSOS samples with $f_{O/salt}$ = 0.43–0.45 and M_n = 20.0–23.2 kg/mol form GYR_O, while nSOS with a higher M_n = 45.2 kg/mol at $f_{O/salt}$ = 0.44 instead forms LAM. Finally, we observe a composition-dependent order-order transition from GYR_O ➞ LAM at $f_{O/salt} \approx 0.48$. Comparison of the N versus $f_{O/salt}$ morphology diagrams for bSOS (Figure 2.3b) and nSOS (Figure 2.4b) at r = 0.01 establishes that O segment dispersity in bSOS shifts the GYR and LAM phase windows by ~10 vol% toward higher $f_{O/salt}$. In other words, the salt-doped, broad dispersity O segment apparently occupies a smaller than expected volume.

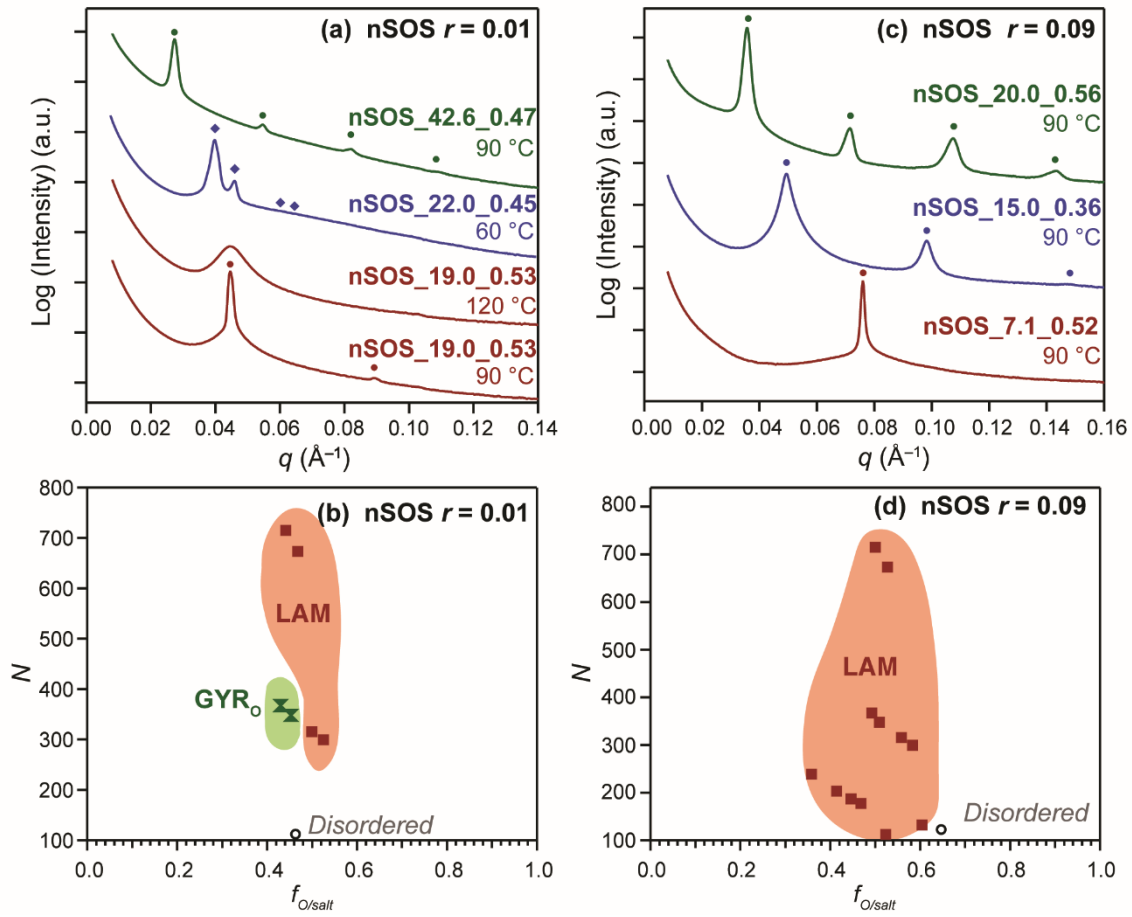

Figure 2. 4. Synchrotron SAXS profiles for representative nSOS triblock polymers at (*a*) $r = 0.01$ and at (*c*) $r = 0.09$, wherein markers indicate the expected peak positions for GYR_O (*diamonds*) and LAM (*circles*). N versus $f_{O/salt}$ morphology diagrams for nSOS triblock polymers at $T = 90$ ºC (b) with $r = 0.01$ and (d) with $r = 0.09$ demonstrate increased salt-loading leads to the stabilization of LAM phases in the studied composition window.

Upon increasing the LiTFSI-doping level to r = 0.05, bSOS triblocks microphase separate with varying degrees of long-range translational order. At $f_{O/salt}$ = 0.41, we observe SAXS maxima at q/q^* = 1, √3, 2 and √7 (q^* = 0.036 Å^{-1}, Figure 2.5a), consistent with CYL_O with modest long-range order. For samples with M_n > 30 kg/mol and $f_{O/salt}$ = 0.37–0.43 at r = 0.05, we observe poorly ordered yet segregated morphologies with broad SAXS peaks analogous to high M_n bSOS with r = 0.01 with similar $f_{O/salt}$ (Figure 2.3a). On that basis, we assign these samples as poorly ordered CYL_O. The sharper SAXS peaks observed in the low M_n CYL_O sample are consistent with greater chain mobility at low χN that enables structure refinement by thermal annealing. bSOS triblocks with asymmetric volume fractions $f_{O/salt}$ = 0.55–0.72 display SAXS intensity profiles with maxima at q/q^*= 1, 2, 3, and 4, corresponding to LAM. Note that the observed intensity and number of higher ordered SAXS peaks is greater for bSOS_19.6_0.66 with r = 0.05 (Figure 2.5a) than bSOS_19.6_0.63 with r = 0.01 (Figure 2.3a), even though both samples originate from the same parent bSOS polymer. Thus, increasing r drives bSOS self-assembly with better long-range order and sharper interfaces in a manner consistent with increased χN. bSOS_12.2_0.60 and bSOS_11.6_0.63, which are disordered at both r = 0 and 0.01, display accessible order-disorder transitions at T_{ODT} = 137 °C and 177 ºC, respectively. This observation is not unexpected as increasing r should increase melt segregation and thus T_{ODT}. Between the CYL_O and LAM phase windows at $f_{O/salt}$ = 0.52, we again observe a double gyroid morphology. bSOS_11.7_0.52 with r = 0.05 (Figure 2.5a) exhibits at least eight well-resolved peaks corresponding to GYR_O with a cubic unit cell parameter a = 39 nm (q^*√6 = 0.039 Å^{-1}). The occurrence of the (510) peak indicates significant long-range

order, which contrasts the less well-organized structure noted for the higher M_n bSOS_23.2_0.53 at r = 0.01 (Figure 2.3a). The above morphology assignments are summarized in Figure 2.5b.

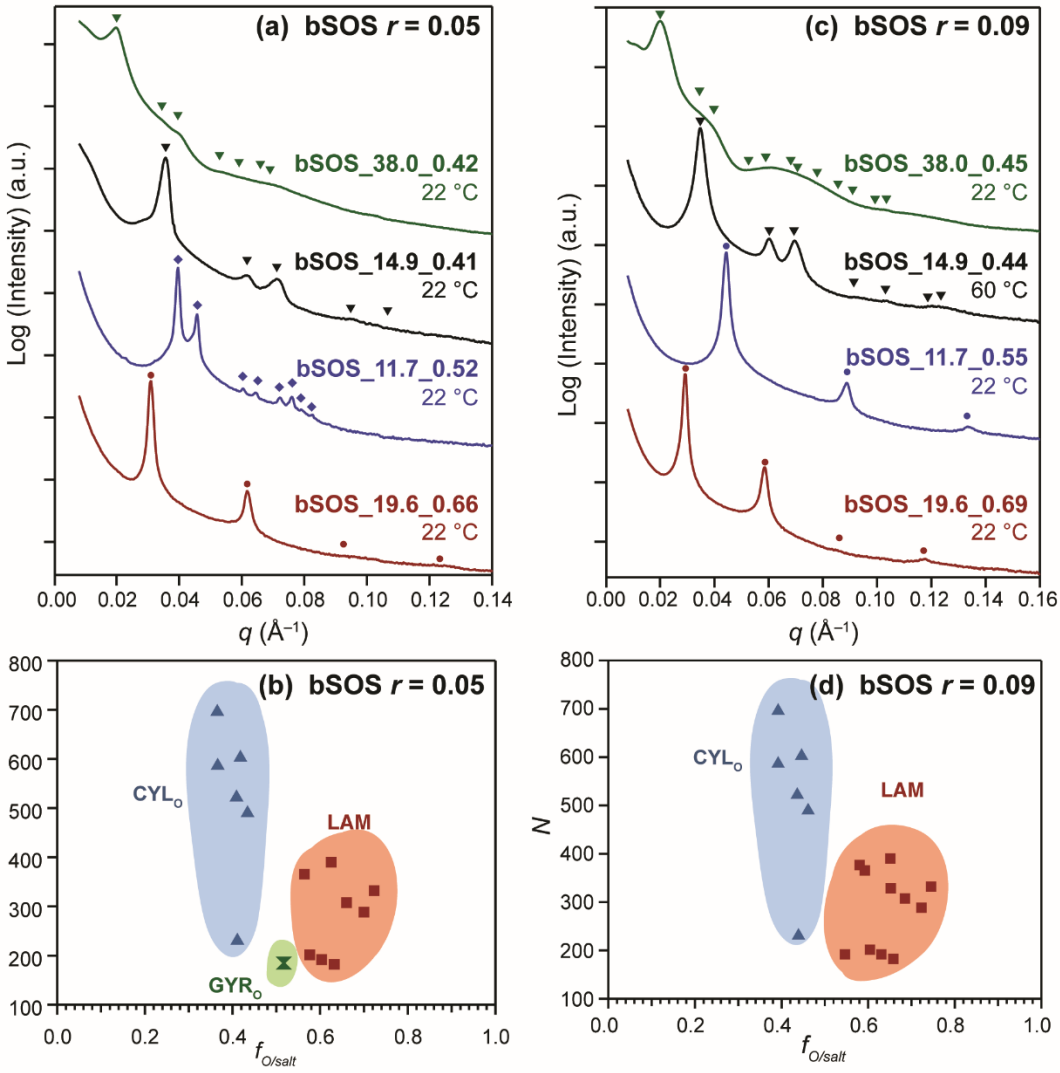

Figure 2. 5. Azimuthally–integrated synchrotron SAXS patterns of representative bSOS triblock polymers with (a) r = 0.05 and (c) with r = 0.09, indicating the expected peak positions for CYL_O (*triangles*), GYR_O (*diamonds*), and LAM (*circles*) phases. *N versus* $f_{O/salt}$ morphology diagrams for (b) r = 0.05 and (d) r = 0.09 at 90 ºC.

The observed composition-dependent microphase windows for bSOS do not markedly change on further increasing the LiTFSI-doping level to $r = 0.09$, except that the GYR_O phase becomes inaccessible. We observe LAM in the asymmetric composition range $f_{O/salt} = 0.55–0.75$ and CYL_O when $f_{O/salt} = 0.39–0.46$ by SAXS (Figure 2.5c), as summarized in the morphology diagram in Figure 2.5d. bSOS_14.9_0.44 ($r = 0.09$) exhibits defined SAXS peaks at $(q/q^*)^2 = 1, 3, 4, 7,$ and 9 corresponding to CYL_O, whereas the higher M_n bSOS_38.0_0.45 exhibits only the broad scattering of poorly-ordered CYL_O (Figure 2.5c) consistent with the above observations. At higher $f_{O/salt}$, bSOS_11.7_0.52 exhibits at least three Bragg peaks corresponding to LAM. While we cannot conclusively rule out the ability of bSOS to form GYR_O at $r = 0.09$, the GYR_O phase window width apparently narrows.

For control nSOS samples at $r = 0.09$, the data provided in Figures 4c and 4d establish that LAM form across the range $f_{O/salt} = 0.36–0.60$. Again, increasing $r = 0.01 \rightarrow 0.09$ also apparently extinguishes the GYR_O phase in these salt-doped polymers (*c.f.*, Figure 2.4b). Note that the GYR phase was previously observed to be unstable for $\chi N > 12$ in LiTFSI-doped narrow dispersity SO diblock polymers.[96] Thus, it appears that salt addition to S/O block polymers may generally restrict access to GYR phases regardless of center O segment dispersity.

2.4.4. Lamellar Domain Sizes in LiTFSI–Doped bSOS

Given that broad dispersity block polymers exhibit variable amounts of LAM domain dilation,[27, 31, 33, 37] we sought to quantitatively assess the extent of domain dilation in the salt-doped bSOS. Plots of lamellar *d*-spacings as a function of *N* at 90 °C for both nSOS

and bSOS samples are given in Figure 2.6(a–c); see Appendix Tables S1–S3 for numerical values. From these plots, one readily observes that the extent of LAM domain dilation in bSOS for $r = 0.01$ is larger than that for $r = 0.05$ or 0.09. While the bSOS d-spacings are ~40% larger than those of corresponding nSOS samples with comparable $f_{O/salt}$ and N (within 10%) at $r = 0.01$, we find a smaller extent of domain dilation of ~15–25% at the higher salt doping $r = 0.05$ and 0.09. Generally, the d-spacings of the nSOS triblocks monotonically increase with r, however the d increases with r in salt-doped in bSOS polymers are weaker as seen in Figure 2.6d: the addition of more LiTFSI to bSOS polymers triggers only small changes in d. Figure A1.2 shows data for other bSOS and nSOS with M_n = 19.0–45.2 kg/mol that exhibit comparable behaviors. Thus, for bSOS and nSOS samples of similar M_n, the d-spacing differences are larger at low salt concentrations and tend to decrease as r increases.

For each bSOS sample series at fixed r, we fit the LAM d-spacing data to the form $d \sim N^{\beta}$ to determine the scaling exponent β (fit shown in Figure 2.6). For $r = 0.05$, the scaling exponents for bSOS and nSOS are the same with $\beta_{b\mathrm{SOS}} = 0.64 \pm 0.08$ and $\beta_{n\mathrm{SOS}} = 0.64 \pm 0.04$, respectively. Increasing the salt-doping level to $r = 0.09$ results in a modest increase in the scaling exponent to $\beta_{b\mathrm{SOS}} = 0.69 \pm 0.07$ and $\beta_{n\mathrm{SOS}} = 0.73 \pm 0.02$. Since the last data positively deviate from $\beta = 2/3$ anticipated by strong segregation theory,[175, 176] we collected and analyzed literature data for the d-spacings of narrow dispersity SO diblock polymers at $r = 0.085$[82, 91] and found that $\beta_{n\mathrm{SO}} = 0.71 \pm 0.03$ (see Figure A1.3). These results collectively imply that block architecture and dispersity differences do not appreciably affect β for $r \geq 0.05$.

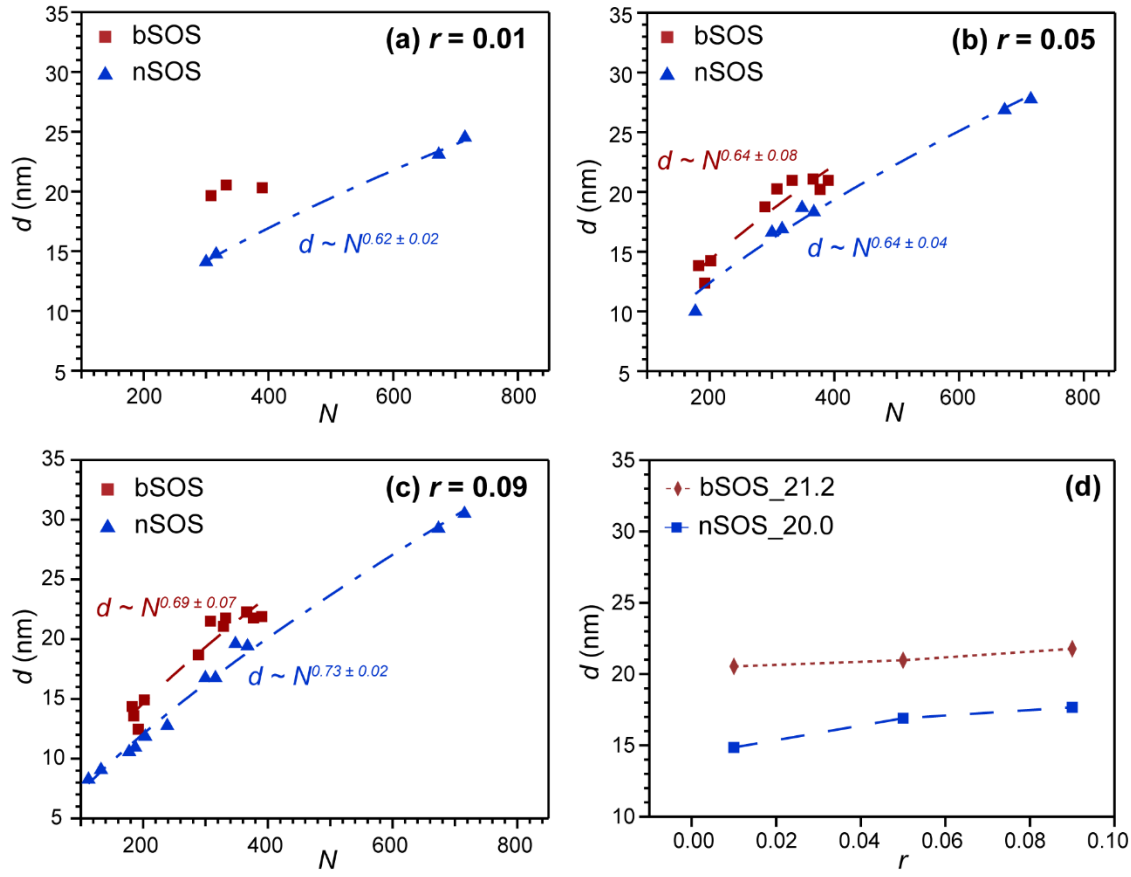

Figure 2. 6. Lamellar *d*-spacing comparison for bSOS (*squares*), nSOS (*triangles*) at r = [LiTFSI]/[EO] = (a) 0.01, (b) 0.05, and (c) 0.09, for which the dashed line represents the power law fit used to obtain β, and (d) *d*-spacings for representative bSOS (*red*) and nSOS (*blue*) triblock polymers with increasing r.

2.4.5. Salt-Doping Dependence of Order and Disorder

SAXS offers a convenient means for determining the ODT temperature (T_{ODT}), at which the Bragg scattering associated with the ordered block polymer morphology evolves into correlation-hole scattering of a disordered melt. The ODT for bSOS_19.6_0.63 at r = 0.01 is relatively broad, as the principal reflection (q^*) gradually diminishes in intensity over a

range of temperatures (Figure 2.7). We assign T_{ODT} as the temperature at which the sharp q^* peak completely vanishes. The transition breadth is not wholly unexpected, as Gibbs' Phase Rule anticipates a window of two-phase coexistence between the ordered and disordered states (assuming a pseudo-two component mixture of bSOS and LiTFSI). Similarly, broad ODT's have been previously observed and rationalized by mean-field theories for salt-doped systems.[177-179] Table 2.2 lists bSOS and nSOS samples that exhibited accessible T_{ODT}'s at different r-values. While the bSOS_19.6_0.63 exhibits T_{ODT} = 139 °C, bSOS_21.2_0.70 with r = 0.01 exhibits a lower T_{ODT} = 111 °C suggesting its closer proximity to the microphase separation transition. At the higher salt concentration r = 0.05, samples with accessible T_{ODT}'s exhibit much lower M_n's than those with r = 0.01. bSOS_11.6_0.63 exhibits T_{ODT} = 177 °C, whereas T_{ODT} = 137 °C of bSOS_12.2_0.60 with the same salt loading r = 0.05. This last observation indicates a strong composition dependence of T_{ODT} in these broad dispersity triblocks, given that these two samples stem from the same *b*PEOC midblock.

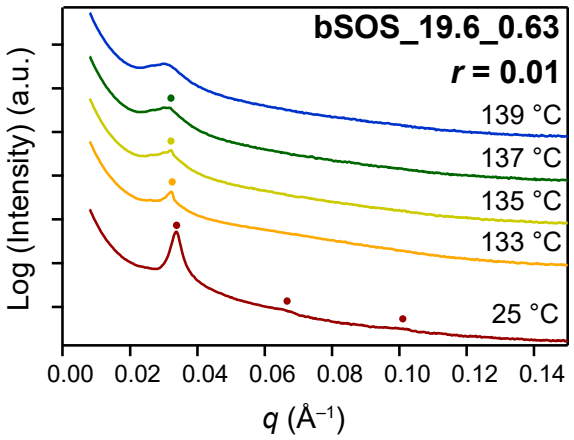

Figure 2. 7. Temperature-dependent synchrotron SAXS profile for bSOS_19.6_0.63 showing the formation of LAM at 25 °C, with T_{ODT} = 139 °C at which the sharp principal (q^*) peak is absent, and only the broad correlation-hole scattering of the disorder state is observed.

Table 2. 2. T_{ODT} and calculated $(\chi N)_{ODT}$ for bSOS and nSOS triblocks at r = 0.01 and 0.05.

r	0.01		0.05	
Sample	bSOS_19.6_0.63	bSOS_21.2_0.70	bSOS_12.2_0.60	bSOS_11.6_0.63
T_{ODT} (°C)	139	111	137	177
$(\chi_{eff}N_{di})_{ODT}$	10.3	10.8	11.1	10.8
Sample	nSOS_19.0_0.53	nSOS_20.0_0.50	nSOS_11.2_0.44	
T_{ODT} (°C)	141	148	189	
$(\chi_{eff}N_{di})_{ODT}$	10.2	10.2	10.7	

We used the f_O-independent effective segmental interaction parameter $\chi_{eff}(T)$ developed by Teran *et al.* for LiTFSI-doped SO diblocks at a given *r*-value

$$\chi_{eff}(T)=\frac{10.2}{T}+\frac{1.85\times10^{3}}{T\cdot N_{di}}+\frac{1.01\times10^{-2}\cdot T}{N_{di}}\left[1\text{-}\exp\left(\frac{-22.4\cdot Tr}{N_{di}}\right)\right]$$

to calculate the segregation strengths $\chi_{eff}N_{di} = \chi_{eff}N/2$ □associated each sample described here, in order to recast the phase information determined for bSOS and nSOS with $r = 0.01$ and 0.05 (Figures 3b, 4b, and 5b) into $\chi_{eff}N_{di}$ *versus* $f_{O,salt}$ morphology diagrams. This complex χ_{eff} expression was derived by fitting the absolute disordered state SAXS intensity from LiTFSI-doped SO diblock polymers to the random phase approximation,[96] wherein N_{di} is the segment density-normalized degree of polymerization of the neat diblock with respect to the reference volume $V_{ref} = 0.1$ nm^3. In spite of disagreements in the literature regarding the best *r*-dependent functional form that describes $\chi_{eff}(T)$ for LiTFSI-doped S/O block polymers, use of this expression for salt-doped SO diblock polymers with reported T_{ODT} values gives $(\chi_{eff}N)_{ODT} = 9.7–10.8$ for $0 \leq r \leq 0.10$, consistent with the mean-field theory prediction $(\chi_{eff}N)_{ODT} = 10.495$. Additionally, this formalism may help to guide the synthesis of bSOS samples with specific attributes for future studies.

Morphology diagrams for bSOS and nSOS constructed using this formalism for $r = 0.01$ and 0.05 are presented in Figure 2.8, and the $(\chi_{eff}N_{di})_{ODT}$ values for samples showing accessible order-disorder transitions are given in Table 2.2. From nSOS_20.0_0.50 with $r = 0.01$, we calculate a critical $(\chi_{eff}N_{di})_{ODT} = 10.2$ for microphase separation. Although mean-field theory for ABA-triblock polymers anticipates that $(\chi N_{di})_{ODT} \geq 8.95$ for microphase separation,[57] the $\chi_{eff}(T)$ of Teran *et al.*[96] likely does not account for segment

connectivity (architecture) effects nor the impact of monomer concentration fluctuations.[11] We observe a similar deviation from the expected mean-field result for nSOS_11.2_0.44 with $r = 0.05$, for which $(\chi_{eff}N_{di})_{ODT} = 10.7$. Inspection of the morphology maps for bSOS in Figure 2.8 (and Table 2.2) shows that for the bSOS triblocks, $(\chi_{eff}N_{di})_{ODT} \geq 10.3$ for $r = 0.01$ and $(\chi_{eff}N_{di})_{ODT} \geq 10.8$ for $r = 0.05$. Thus, increased salt-doping of the bSOS samples only slightly increases $(\chi N)_{ODT}$ for microphase separation over that for the control nSOS samples.

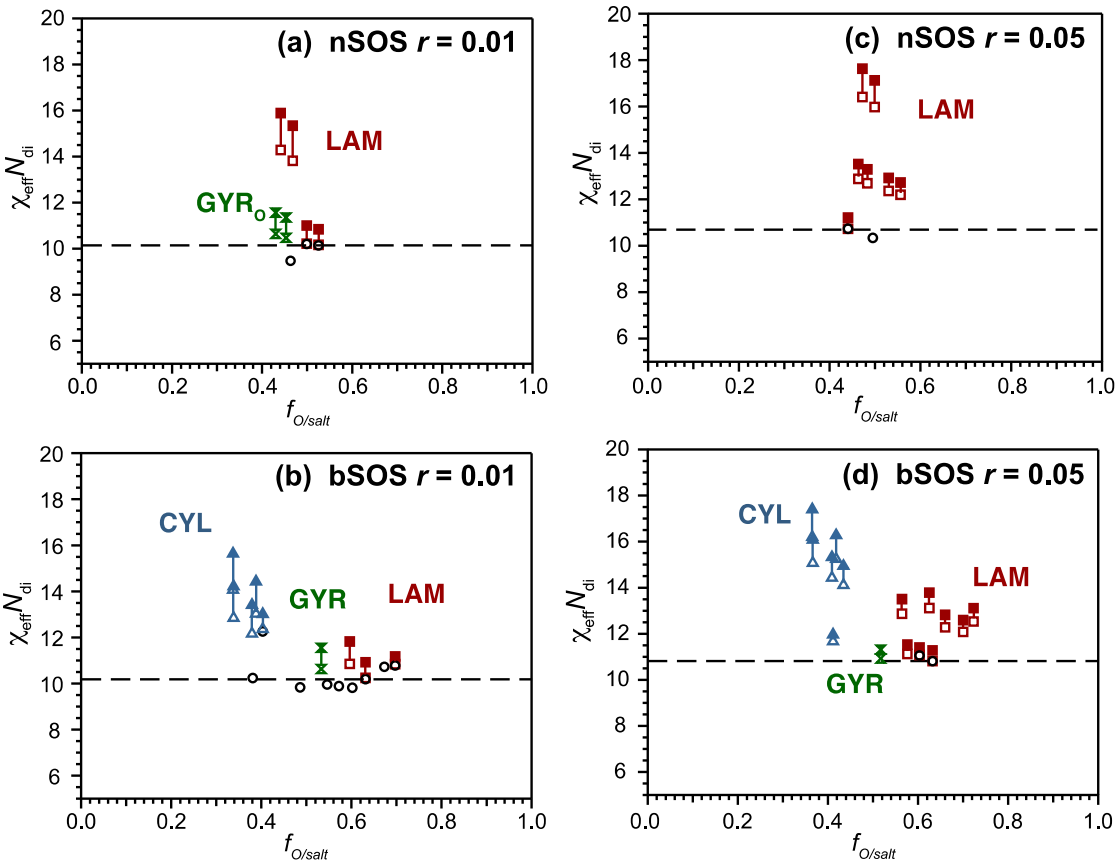

Figure 2. 8. ($\chi_{eff}N$) versus $f_{EO/salt}$ morphology diagrams at r = 0.01 for (a) nSOS and (b) bSOS, and at r = 0.05 for (c) nSOS and (d) bSOS at a reference temperature T_{ref} = 90 °C. The vertical lines indicate the range of temperatures over which the morphologies were determined by SAXS, and those lines capped with black open circles indicate samples that disordered on heating. The dashed line is drawn to indicate the minimum observed $(\chi_{eff}N_{di})_{ODT}$ at a given salt-doping level r.

2.5. Discussion

A few reports have documented segmental dispersity-induced dilation of the lamellar *d*-spacings of ABA triblocks with broad dispersity B midblocks, which stems from the broad chain length distribution and is likely sensitive to its exact width and shape.[40, 47] Generally, *d*-spacing dilation has been ascribed to two synergistic effects: (1) the presence of much longer than average B segments that fill space, and (2) interfacial desorption of ABA chains with short B segments that effectively act as "A–A homopolymers" that swell the A domains.[31] Lynd *et al*. described a method for calculating the critical B segment M_n below which chain desorption occurs, by equating the enthalpy cost for dissolving a short B segment in the A domain and the entropy gain from releasing the stretched chains from the domain interfaces.[47] They showed that the critical desorption chain length scales as $(\chi N)^{-2/3}$, thus predicting reduced *d*-spacing dilation in strongly segregated polymers due to suppressed chain pull out.

By virtue of the ability to tune χ_{eff} at constant N in a given bSOS by varying the salt-doping level r, our data provide an opportunity to analyze how *d*-spacing dilation changes with melt segregation strength. The data shown in Figure 2.6 indicate that the extent of domain dilation is greatest at $r = 0.01$ and that less domain dilation occurs when $r = 0.05$ and 0.09. These results may be rationalized by first considering how lamellar *d*-spacing depends on r for nSOS. In salt-doped nSOS, d increases with r since the O domain volume is augmented by the preferential solvation of LiTFSI and the concomitant increase in χ between the S and LiTFSI-doped O-domains leads to chain stretching. While these physical principles apply to bSOS and should drive *d*-spacing increases, the overall increase in χN

raises the enthalpic penalty for interfacial chain desorption and decreases the extent of "A-A homopolymer" swelling (*vide supra*). Apparently, these two effects cancel and result in the observed weak dependence of d on the doping level, r.

The LAM window shift to asymmetric volume fractions $f_{O/salt} \approx 0.55–0.75$ irrespective of bSOS salt doping level (r) is nearly identical to the dispersity-induced lamellar composition shifts previously reported in SBS[33] and LBL triblocks[38] with broad dispersity B segments. Given the low degree of "S–S homopolymer" swelling in the strongly segregated LiTFSI-doped bSOS, this LAM morphology window shift must arise from synergistic chain packings in the disperse O/salt microdomain that foster buckling towards it in a manner similar to that noted in LBL triblocks.[38] The details of this co-surfactant-like chain packing that fosters curvature toward the disperse domain have been explained elsewhere[33,65] and are not reiterated here.

In contrast to previous studies that found either large increases or decreases in the critical $(\chi_{eff}N_{di})_{ODT}$ for microphase separation of ABA-type triblocks with broad dispersity B segments,[31, 34] the critical $(\chi_{eff}N_{di})_{ODT}$ for salt-doped bSOS only marginally increases from the expected value of $(\chi_{eff}N_{di})_{ODT} = 8.95$ for narrow dispersity materials. In the case of SBS triblocks with broad dispersity B segments, the segregated melt is stabilized by synergistic interfacial chain packings of the medium and long chains in the distribution that decrease center segment chain stretching. This result concurs with self-consistent mean-field theory (SCFT) calculations by Matsen for such systems.[44] However, center B segment dispersity in high χ/low N LBL triblocks amplifies monomer concentration fluctuations that destabilize the ordered morphologies. The magnitude of this destabilization apparently

overwhelms the synergistic chain packing stabilization, leading to a net increase in the critical $(\chi N)_{ODT}$.[34] Modified SCFT calculations by Pandav and Ganesan[59] and Monte Carlo simulations by Beardsley and Matsen[51] indicate that dispersity enhances fluctuation effects, as experimentally demonstrated for nearly monodisperse diblock oligomers by Oschmann and co-workers.[56]

The modest changes in $(\chi N)_{ODT}$ for salt-doped bSOS likely arise from a combination of two opposing factors depicted in Figure 2.9. While O segment dispersity is expected to enhance monomer concentration fluctuations and drive up $(\chi N)_{ODT}$, preferential solvation of LiTFSI in the O domains increases segment incompatibility and drives microphase separation in a manner that counters the enhanced concentration fluctuations.[92, 93, 180]Additionally, ithium ions in the salt-doped O domains are coordinated by 2–7 O monomer units from one or several polymer chains, which dynamically crosslink these domains.[73, 181, 182] Ren *et al.*[183] have proposed a model in which they predict that preferential anion solvation and dynamic lithium salt crosslinks synergistically enhance microphase separation, and recent experiments by Xie and Lodge[184] suggest that similar effects drive blend phase separation in salty poly(ethylene-*alt*-propylene)/PEO. Consequently, the effect of salt solvation in the O domain dominates, leaving only small changes in the critical $(\chi_{eff}N_{di})_{ODT}$ upon LiTFSI salt doping of bSOS.

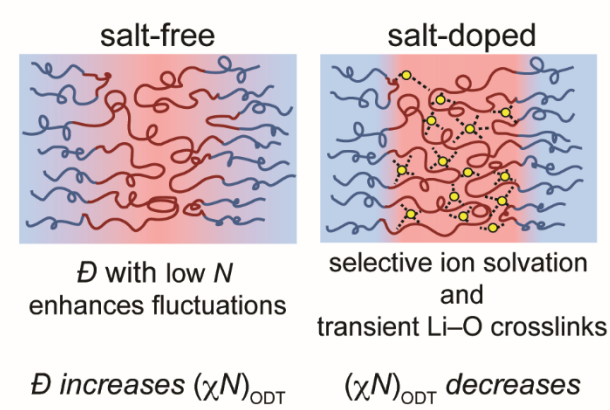

Figure 2. 9. For high χ/low N salt-doped bSOS, (a) broad dispersity low N polymer chains enhance fluctuation effects thereby disfavoring microphase separation, while (b) solvation of LiTFSI in the O domain leads to increased segment incompatibility and dynamic cross-linking of the O segments, both of which stabilize the ordered morphology.

This notion is further supported by a detailed comparison of the phase behaviors of bSOS doped with LiTFSI at r = 0.01 and 0.05. From the data presented in Table 2.2, one finds that the $(\chi_{eff}N_{di})_{ODT} \sim 10.2$ at r = 0.01 with overall M_n = 19.6–21.2 kg/mol. On the other hand, $(\chi_{eff}N_{di})_{ODT} \sim 11$ for samples with r = 0.05 and M_n = 11.6–12.2 kg/mol. This modest difference in the critical segregation strength for microphase separation follows the expected trend that the fluctuation corrections for lower molecular weight systems are stronger and lead to greater destabilization of the microphase separated morphology.

2.6. Conclusion

In this work, we described the synthesis and characterization of seventeen unimodal yet continuously disperse bSOS polymers by a sequential condensation polymerization and

ATRP, to furnish broad dispersity O midblocks flanked by narrow dispersity S end blocks with $0.33 \leq f_O \leq 0.69$ and $11.7 \leq M_n \leq 43.8$ kg/mol. Temperature-dependent SAXS analyses were used to construct morphology maps of bSOS samples doped with varying amounts of LiTFSI at salt loading levels $r = 0$–0.09. Generally, the bSOS lamellar phase window shifts by ~10 vol% to higher $f_{O/salt}$ based on direct comparisons with 13 narrow dispersity nSOS analogs that were characterized at the same LiTFSI loadings. Additionally, midblock dispersity dilates the lamellar microdomain *d*-spacing, although the extent of domain dilation depends on the specific *r*-value. The critical segregation strength for microphase separation is found to be $(\chi N/2)_{ODT} \geq 10.3$ for $r = 0.01$, whereas $(\chi N/2)_{ODT} \geq 10.8$ for $r = 0.05$. Thus, segmental dispersity in salt-doped polymers only incrementally increases the critical segregation strength from the mean-field theory prediction $(\chi N/2)_{ODT} = 8.95$. This last result contrasts previous work on ABA-type triblock polymers in which mid-segment dispersity results in larger changes in the location of the microphase separation transition. We attribute the present findings in the salty bSOS to a competition between dispersity-enhanced fluctuations in these high χ/low N materials near the ODT and and preferential lithium salt solvation in the O domains that stabilizes the ordered melts.

Chapter 3. Ionic Conductivities of Broad Dispersity Lithium Salt-Doped Poly(styrene)/Poly(ethylene oxide) Triblock Polymers

3.1. Synopsis

We describe the impact of center poly(ether) segment dispersity ($Đ = M_w/M_n \sim 1.45$) on the Li-ion conductivities of salt-doped poly(styrene-*block*-oligo(ethylene oxide) carbonate-*block*-styrene) (bSOS) electrolytes with narrow dispersity end blocks. Three representative bSOS samples with $M_{n,total}$ = 11.7–23.9 kg/mol were doped with lithium bis(trifluoromethanesulfonyl)imide (LiTFSI) with $r = [Li^+]:[O] = 0.09$. Small-angle X-ray scattering (SAXS) analyses reveal that these samples with $0.55 \leq f_{O/salt} \leq 0.60$ self-assemble into lamellar morphologies, with ionic conductivities as high as $\sigma = 0.19$ mS/cm at 90 °C from electrochemical impedance spectroscopy (EIS). The ionic conductivities of LiTFSI-doped bSOS are comparable to those of salt-doped, narrow dispersity nSOS triblocks with $M_n \gtrsim 20$ kg/mol, and are 2-3 times greater than those of the narrow dispersity nSO diblock control samples. These findings are rationalized in terms of segment dispersity-induced decreases in the lamellar grain size, which enhance intergrain connectivity and transport.

3.2. Introduction

Development of next-generation, lithium-ion batteries that exhibit enhanced safety, rechargeability, energy density is essential to broaden the spectrum of their utility, especially, in various transportation applications.[61] An attractive approach to maximizing the energy densities of Li-ion batteries relies on the use of lithium metal anodes.[63] However, the commercialization of rechargeable Li metal batteries with conventional liquid

electrolytes is impeded by the propensity for lithium dendrite growth during charging, which leads to cell failure by short circuiting.[62, 64, 65] The use of conventional liquid electrolytes in such systems, which comprise a lithium salt dissolved in an organic solvent, further exacerbates these utility and safety concerns due to their volatile and flammable characteristics. Consequently, numerous groups have pursued the development of alternative, non-flammable, solvent-free polymer electrolytes that enable safe operation of Li metal batteries. Ideal polymer electrolytes in these cells contain no volatile or flammable solvents, and they exhibit large elastic moduli in order to mechanically suppress lithium dendrite growth (some reports suggest that the moduli should exceed 1 GPa,[66, 67] although this value is the subject of current debate)[70, 71]. In this context, lithium salt-doped poly(ethylene oxide) (PEO) has long been studied as a candidate dry polymer electrolyte.[60, 72] However, PEO-based electrolytes that exhibit useful Li-ion conductivities do not typically exhibit the mechanical strength required for optimal cell performance and longevity mandated by applications.[77-79]

By virtue of their hybrid properties that originate in the physical attributes of their constituent segments, block polymers offer exciting opportunities for molecular design of new battery electrolytes that address the vexing trade-off between high ionic conductivity and good mechanical strength.[75, 77-79, 185] Narrow dispersity poly(styrene-*block*-ethylene oxide) (nSO) diblock polymers doped with lithium bis(trifluoromethylsulfonyl)imide (LiTFSI) are such archetypal polymer electrolytes, in which the glassy poly(styrene) domains impart the requisite stiffness to prevent dendrite growth and the liquid-like, LiTFSI-doped PEO domains furnish high ionic conductivities. The widespread use of

LiTFSI largely stems from the fact that the PEO segments of these salt-doped polymers exhibit glass transition temperatures $T_g \sim -44$ °C even at salt loadings as high as $r = [Li^+]/[\text{EO monomers}] = 0.09$, with suppressed propensity for crystallization.[72, 76, 84] Various studies have established that materials with nearly symmetric volume fractions ($f_S = f_O = 0.5$) with $r_{LiTFSI} = 0.09$ exhibit a useful balance of these orthogonal mechanical and conductivity characteristics.[69, 81]

Numerous experimental reports have consequently investigated the self-assembly thermodynamics and ion conductivities of lithium salt-doped nSO diblocks.[81-84, 91, 102, 186] Balsara and co-workers demonstrated that the ionic conductivities of lamellar, salty nSO diblock polymers increase with increasing M_n, such that optimal conductivities are achieved when the total $M_n \gtrsim 200$ kg/mol.[81, 82] Given that such high molecular weight materials are difficult to synthesize and process, various groups have alternatively investigated the properties of different block polymer architectures and compositions including triblock,[112, 187, 188] star,[107] brush,[189, 190] and hyperbranched block polymers.[191] More recently, Morris et al.[192] and Xie et al.[106] have investigated microphase separated bock polymer/homopolymer blends as means of further improving the conductivities of these "dry" electrolytes. All of these studies collectively establish that chain architecture, the presence of PEO homopolymer, and the chemical identities of the polymer end group functionalities influence the observed conductivities.[110, 111] However, these model studies have thus far not explicitly addressed the effects of increased segment dispersity on the conductivities of these electrolytes.

Advances in macromolecular synthesis over the last 30 years afford scalable access to myriad block polymer materials, with variable degrees of molar mass dispersity control in each segment. Experimental and theoretical studies of the self-assembly thermodynamics of disperse A/B block polymers have established their ability to microphase separate into lamellae (LAM), hexagonally-packed cylinders (HEX), and spheres (SPH) phases with variable long-range translational order, even when the constituent segment dispersities approach $Đ = M_w/M_n \approx 2.0$.[12, 26, 31, 34, 35, 37, 40, 41] Detailed studies indicate that the periodic domain spacings (d) of their segregated morphologies are typically dilated relative to those of narrow dispersity analogues with the same M_n. Additionally, the order-disorder transition temperatures (T_{ODT}'s) for these melts also change with segmental dispersity.[27-29, 31, 33, 34, 39] Contrary to the expectation that molecular precision is a pre-requisite for periodic mesoscale self-assembly, these studies demonstrate that segmental dispersity is another tool for manipulating block polymer phase behavior. Consequently, newer synthetic approaches have been specifically developed to reproducibly access block polymers with tailored dispersities.[19, 20, 22, 25]

In this connection, we recently sought to understand how segment dispersity in LiTFSI-doped poly(styrene)/poly(ethylene oxide) block polymers alters their microphase separation thermodynamics and morphologies. Toward this end, we developed a tandem synthesis of well-defined poly(styrene-*block*-oligo(ethylene oxide) carbonate-*block*-styrene) (bSOS) triblock polymers, in which broad dispersity O segments with $Đ_O \approx 1.45$ are flanked by narrow dispersity S end blocks with $Đ_S \lesssim 1.18$.[49] Phase mapping studies employing 17 bSOS polymers variably salt-doped with LiTFSI at loadings $0 \leq r \leq 0.09$

revealed that O segment dispersity asymmetrically shifts the LAM morphology window to $f_{O/salt} \approx 0.55–0.75$ with low degrees of *d*-spacing dilation, as compared to comparably salt-doped narrow dispersity nSOS triblock polymers. Temperature-dependent small-angle X-ray scattering (SAXS) studies revealed that the T_{ODT} values for the salty bSOS samples were similar to those of comparably salt-loaded nSOS. While this study suggests that the LAM phases of LiTFSI-doped bSOS could exhibit higher conductivities than nSOS/LiTFSI due to their occurrence at higher $f_{O/salt}$ values, the conductivity behaviors of these materials have not yet been reported. Furthermore, it is unclear whether dispersity confers any additional benefits on electrolyte performance.

Herein, we describe detailed studies of morphology-dependent conductivity behaviors LAM-forming LiTFSI-doped bSOS samples with $r = 0.09$ with near symmetric volume fractions $f_{O/Salt} = 0.55\text{-}0.60$. We specifically compare the conductivities of salt-doped bSOS measured by temperature-dependent electrochemical impedance spectroscopy, along with those of narrow dispersity nSOS triblock and nSO diblock control samples with comparable M_n values and $f_{O/Salt}$ values. We show that the volume fraction-normalized conductivities of the bSOS polymers are comparable to or slightly higher than those of nSOS, suggesting that dispersity does not appreciably alter electrolyte performance. Surprisingly, we find that salty nSOS and bSOS with $M_n \gtrsim$ 20 kg/mol exhibit 2-3 times higher conductivities than nSO diblocks with similar *d*-spacings. By correlating these results with SAXS analyses of these samples, we uncover an architecture- and a dispersity-independent relationship between lamellar grain size and the observed conductivity. Thus,

we demonstrate that grain size manipulation by segmental dispersity in bSOS results in higher conductivity electrolytes.

3.3. Experimental Methods

Materials. All reagents were purchased from Sigma-Aldrich Chemical Co. (Milwaukee, WI) and were used as received unless otherwise noted. A commercial PEO homopolymer with M_n = 30.8 kg/mol and $Đ$ = 1.02 was azeotropically freeze-dried in C_6H_6 and stored in a glove box under an Ar(*g*) atmosphere.

^{1}H Nuclear Magnetic Resonance (NMR) Spectroscopy. A Bruker Advance III HD 400 MHz spectrometer was used to acquire all ^{1}H NMR spectra. Spectra were referenced to the residual protiated solvent resonance of $CDCl_3$ (δ 7.26 ppm). A pulse repetition delay of 10-15 s was applied to ensure quantitative peak integration accuracy for polymer composition analyses.

Size-Exclusion Chromatography (SEC). SEC analyses on S/O block polymers were conducted on an Agilent 1200 Series GPC equipped with two Viscotek I-series columns (MBMMW-3078), a Wyatt Optilab T-rEX differential refractometer, and a Wyatt DAWN HELEOS II multi-angle laser light scattering detector running in 0.05 M LiBr in *N,N*-dimethylformamide (DMF) with a flow rate of 1.0 mL/min at 50 °C. The refractive index increment (*dn/dc*) for each sample was calculated by assuming 100% mass recovery on sample elution. SEC data for polystyrene homopolymers were obtained on a Viscotek GPCMax System equipped with two Polymer Labs Resipore columns (250 mm x 4.6 mm) and a differential refractometer, operating at 40 °C in THF with a flow rate of 0.8 mL/min. Molecular weight determination relied on a polystyrene calibration curve, which was

constructed using 10 narrow dispersity standards with M_n = 580-377,400 g/mol (Polymer Laboratories, Amherst, MA).

Differential Scanning Calorimetry (DSC). Glass transition temperatures (T_g) of the salt-doped polymers were measured using a TA Q1000 DSC instrument with sample enclosed in hermetically sealed aluminum DSC pans. The samples were first heated to 110 ºC, annealed for 5 min, cooled to -100 ºC and then heated to 110 ºC at 10 ºC/min. The glass transition temperatures are determined from the second heating ramp. Thermograms showing the melting endotherm of crystalline LiTFSI-doped bPEOC and PEO polymers were recorded by heating the samples to 80 ºC, annealed for 5 min, cooled to -20 ºC, isotherm for 5 min and then heated to 80 ºC at 10 ºC/min.

Synthesis α,ω-di(methyl)-poly(oligo(ethylene oxide) carbonate) (bPEOC). An azeotropically freeze-dried α,ω-di(hydroxy)-poly(ethyene oxide) (15.00 g, M_n = 1.4 kg/mol and $Đ$ = 1.12, 10.7 mmol), NaH (60 *wt*% dispersion in mineral oil, 0.0436 g, 10.9 mmol) and dimethyl carbonate (4.5 mL, 53.4 mmol) were combined in a 100 mL Schlenk tube under inert atmosphere. Under a flush of $N_2(g)$ on a high vacuum Schlenk line, a water-cooled distillation head was attached to the reaction tube. The reaction flask then heated at 120 ºC for 2 h under ambient pressure, after which the temperature was increased to 180 ºC and the pressure was slowly reduced to 0.10 Torr. The condensation polymerization reaction was continued under this last condition for 1 h, while the volatile CH_3OH reaction byproduct and unreacted dimethyl carbonate distilled into a receiving flask chilled with dry ice/2-propanol. Upon cooling the reaction back to 22 °C, the resulting polymer was dissolved in CH_2Cl_2 (50 mL), twice precipitated into Et_2O (2 × 500 mL), and

azeotropically freeze-dried from C_6H_6 under vacuum. M_n = 45.5 kg/mol, $Đ$ = 2.31 by SEC in 0.05 M LiBr in DMF.

Syntheses of Poly(styrene)/Poly(ethylene oxide) Block Polymers. The bSOS and nSOS block polymers were synthesized and characterized as previously described.[49] nSOS samples were prepared by hydroxyl end-functionalization of the commercially available, narrow dispersity PEO with bromoisobutryl esters and subsequent Cu-catalyzed ATRP of styrene by analogy to the bSOS syntheses. The nSO diblock polymer was prepared via sequential anionic polymerization of styrene and ethylene oxide as described in Irwin et al.[193]

Polymer Sample preparation. In an argon-filled glovebox, freeze-dried S/O block polymers were dissolved in a LiTFSI solution in THF/C_6H_6 (10/90 *v/v*) of known concentration to achieve the desired [Li^+]/[O] composition. These mixtures wer homogenized by sonication for 5 min, and directly freeze-dried under dynamic vacuum for 2 d to effect solvent removal. The resulting salt-doped block polymers formed either fluffy powders or solid foams, which were stored in the moisture free environment of an argon-filled glove box ([H_2O] < 4 ppm).

Salt-doped PEO and bPEOC homopolymers were prepared by first co-dissolving the homopolymer and LiTFSI salt in a small volume of THF in a 25 mL Schlenk tube with stirring until a homogeneous solution formed. The THF solvent then was removed under vacuum on a Schlenk line, followed by the addition of anhydrous CH_2Cl_2 in order to co-evaporate the residual THF in the sample. Finally, these samples were heated under high vacuum in an oil bath thermostatted at 45 °C for 2 d in order to effect complete solvent

removal. The resulting viscous, hygyoscopic solids were stored under inert atmosphere to prevent water uptake.

For each of the salt-doped polymer samples, the complete solvent removal was confirmed by ^{1}H NMR spectroscopy.

Electrochemical Impedance Spectroscopy (EIS). In a glove box under Ar(*g*), salt-doped polymer samples were loaded into Teflon O-rings (thickness $T = 1.04 \pm 0.04$ mm, and inner diameter $D = 5.35 \pm 0.12$ mm as measured by a digital micrometer) situated between two, flat stainless steel blocking electrodes under inert atmosphere in a glovebox. The stainless steel electrode surfaces were hand-polished with Buehler Micropolish (Union Carbide, 1 μm α-Al_2O_3) in Type I ultra–pure water (> 18 MΩ•cm), and cleaned in a PCE-44-LD UV-Ozone cleaner equipped with a double wave mercury UV lamp (254 nm and 184 nm) with peak intensity 4.6 mW/cm^2 for 20 min prior to transfer to the glovebox. This assembly was heated to 50 °C to entirely fill the sample gap and to ensure conformal polymer contact with the electrodes. The resulting electrode sandwiches were placed into a home-made, precision-milled reusable coin cell compression holder that was hermetically sealed with Kalrez O-rings held in place with six screws. Sealed sample cells were removed from the glovebox for subsequent analyses. The top and bottom electrodes were connected to a Metrohm Autolab PGSTAT302N electrochemical impedance analyzer equipped with FRA32M modules by temperature shielded copper wires. EIS measurements were controlled by the Metrohm Nova 2.0 software over the frequency range $\omega = 1–10^5$ Hz with an applied AC amplitude of 50 mV. For temperature-dependent measurements between $T = 40–100$ °C, coin cells were placed in a Lindburg Blue M

vacuum oven (Thermo Scientific, Waltham, MA) equipped with a CN7800 OMEGA temperature controller (±0.2 °C accuracy). During each EIS measurement, the temperature of the coin cell was recorded by an Omega OM-EL-USB-1-LCD temperature logger with a surface thermocouple directly attached to the coin cell. After thermally annealing the coin cell at 110 ºC for 2 h, conductivity measurements were performed on cooling from 100 to 40 °C in 5 °C decrements, with a 1 h pre-measurement equilibration time at each temperature. Conductivities measured on heating from 40 to 100 °C were also recorded and agree with the cooling ramp data within 5%. All reported data derive from the initial cooling ramp. The resistance (R) at each temperature for each sample was obtained from the high frequency, horizontal (real-axis) intercept of the resulting Nyquist plots. The ionic conductivity was then calculated as $\sigma = T/(A \cdot R)$, where the electrolyte thickness (T) and cross-sectional area (A) were specified by the Teflon O-ring spacer. Three parallel conductivity measurements on individually prepared samples were performed for each homopolymer and block polymer. Reported values reflect the average and standard deviation in these trials.

Small Angle X-Ray Scattering (SAXS). Samples for synchrotron SAXS analyses were prepared by loading Teflon O-ring spacers (thickness $T = 0.73 \pm 0.02$ mm, inner diameter $D = 3.65 \pm 0.08$ mm) with salt-doped polymer samples at 50 °C in an argon glovebox. These samples were loaded into the home-made reusable coin cells and annealed at 120 °C for 2 h, as with the conductivity samples. These thermally cycled samples were then taken back into the glovebox and snugly fit into hermetically sealed DSC pans (TA Instruments, New Castle, DE) for temperature-dependent scattering measurements. Note that this

strategy ensures a uniform sample thickness across all samples. Synchrotron SAXS measurements were made at the 12-ID-B beamline of the Advanced Photon Source (Argonne, IL). Using an incident beam wavelength of $\lambda = 0.886$ Å and a 3.605 m sample-to-detector distance, 2D-SAXS patterns were recorded on a Pilatus 2M CCD rectangular area detector (25.4 cm × 28.9 cm with 1475 × 1679 pixel resolution) using a 1 s sample exposure time. The DSC pans containing the block polymer samples were thermally equilibrated at each desired temperature in a multi-array sample stage for at least 10 min prior to X-ray exposure. The scattering wavevector *(q)* scale was calibrated using a silver behenate standard ($d = 58.38$ Å), and reduced one-dimensional intensity Log[$I(q)$] versus scattering wavevector q profiles were generated using a data reduction tool available at the beamline. The full-width at half-maximum (FWHM) for each of the primary scattering peaks (q^*) were resolved from the linear intensity profiles using the multi-peak fitting package for Igor Pro (Wavemetrics, Inc.) by fitting a Voigt distribution for the primary SAXS peak, after a log(intensity) background correction using a 5th order q-dependent polynomial.

3.4. Results & Analysis

We synthesized three bSOS samples (Figure 3.1) using the multi-step, tandem polymerization strategy detailed in our earlier publication.[49] Briefly, condensation polymerization of α,ω-di(hydroxy)-oligo(ethylene oxide) ($M_n = 1.4$ kg/mol and $Đ = 1.12$) with excess diallylcarbonate in the presence of NaH followed by treatment of the isolated polymer with HCOOH and catalytic $(Ph_3P)_4Pd$ yielded α,ω-dihydroxy-bPEOC with $Đ \approx 1.45$. Hydroxyl end-functionalization the telechelic bPEOC with bromoisobutryl bromide

yielded a difunctional macroinitiator, from which bidirectional Cu-catalyzed atom transfer radical polymerization (ATRP) of the styrene furnished the desired bSOS. Integration of the thermodynamically-controlled step-growth polymerization with a kinetically-controlled chain growth polymerization provides scalable access to bSOS triblocks in which narrow dispersity S end segments flank a broad dispersity center O block. As experimental controls for our morphology and conductivity studies of LiTFSI-doped bSOS, we also synthesized nSOS triblocks (Figure 3.1) by bidirectional Cu-catalyzed ATRP of styrene from an α,ω-bis(bromoisobutyryl)-poly(ethylene oxide). Finally, nSO diblock control samples were produced by sequential living anionic polymerizations of styrene and ethylene oxide per a prior report by Irwin et al.[193] The molecular characteristics of the polymers used in this study are listed in Table 3.1.

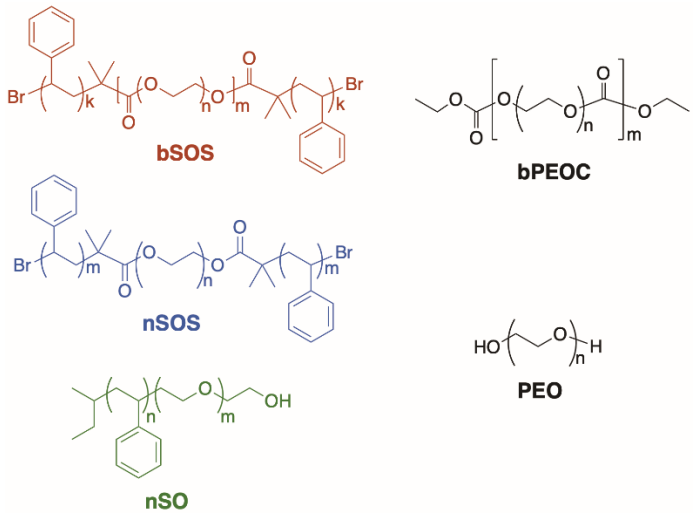

Figure 3. 1. Molecular structures of the poly(styrene)/poly(ethylene oxide) materials used in this study.

Table 3. 1 Molecular Characteristics of bSOS, nSOS, and nSO Polymers.

Sample	$M_{n,O}$[a]	$Đ_O$[b]	$M_{n,S}$[c]	$Đ_S$[d]	$M_{n,SOS}$	$f_{O/Salt}$[f]
bSOS_11.7_0.55	5.7	1.43	3.0	1.18	11.7	0.55
bSOS_12.8_0.60	7.0	1.45	2.9	1.13	12.8	0.60
bSOS_23.9_0.58	12.5	1.48	5.7	1.11	23.9	0.58
nSOS_45.2_0.50	20.0	1.01	12.6	1.14	45.2	0.50
nSOS_20.0_0.56	10.0	1.03	5.0	1.12	20.0	0.56
nSOS_11.2_0.47	4.6	1.02	3.3	1.13	11.2	0.47
nSO_4.6_0.45	1.8	1.05	2.8	*n.d.*[e]	4.6	0.45
nSO_14.4_0.48	6.1	1.03	8.3	*n.d.*[e]	14.4	0.48
bPEOC	45.5	2.31	-	-	-	1.0
PEO	35.0	1.05	-	-	-	1.0

[a] Determined by quantitative ^{1}H NMR spectroscopy end group analyses. [b] Obtained by SEC in 0.05 M LiBr/DMF at 50 ºC, using *dn/dc* = 0.043 mL/g for bPEOC segments and *dn/dc* = 0.042 mL/g for O in nSOS. [c] Calculated based on $M_{n,O}$ from quantitative ^{1}H NMR spectroscopy. [d] Measured by THF SEC at 40 ºC versus narrow dispersity S homopolymer standards after polymer degradation per the method in Ref. [49]. [e] *n.d.* = not determined. [f] Calculated with r = [Li]/[EO units] = 0.09 (see text for details).

Ion containing block polymer electrolytes based on bSOS, nSOS, and nSO block polymers were then produced by preparing each of these polymers with LiTFSI at a fixed loading r = 0.09. The selection of this loading level throughout this study derives from the fact that PEO exhibits the highest conductivities at this r-value.[72, 194] For these LiTFSI-doped polymer samples, the volume fraction of the O/salt microphase is calculated according to the expression of Teran and Balsara:[96]

$$f_{\mathrm{O/salt}} = \frac{\frac{M_{\mathrm{n,\,PEO}}}{\rho_{\mathrm{PEO}}} + r\frac{M_{\mathrm{n,\,PEO}}}{M_{\mathrm{EO}}}\frac{M_{\mathrm{LiTFSI}}}{\rho_{\mathrm{LiTFSI}}}}{\frac{M_{\mathrm{n,\,PEO}}}{\rho_{\mathrm{PEO}}} + r\frac{M_{\mathrm{n,\,PEO}}}{M_{\mathrm{EO}}}\frac{M_{\mathrm{LiTFSI}}}{\rho_{\mathrm{LiTFSI}}} + 2\frac{M_{\mathrm{n,\,PS}}}{\rho_{\mathrm{PS}}}}$$

where $M_{\mathrm{n,PEO}}$ and $M_{\mathrm{n,PS}}$ are the respective molar masses of the O and S segments, M_{EO} and M_{LiTFSI} are the corresponding molar masses of ethylene oxide (44.05 g/mol) and LiTFSI (287.09 g/mol), ρ_{PS} = 1.032 g/cm^3 and ρ_{PEO} = 1.073 g/cm^3 are the homopolymer melt densities at 90 ºC, and ρ_{LiTFSI} = 2.023 g/cm^3 is the effective LiTFSI density. Use of this expression assumes selective LiTFSI solvation in the polyether O domains. The compositions of the bSOS and nSOS materials were specifically designed to form microphase separated LAM morphologies with comparable $f_{\mathrm{O/salt}}$ values (within 12%) on LiTFSI doping at comparable total M_{n} values. Note that perfect matching of the $f_{\mathrm{O/salt}}$ and $M_{\mathrm{n,total}}$ at r = 0.09 for bSOS and nSOS is not possible, since O segment dispersity asymmetrically shifts the LAM phase composition window and narrows the common composition range over which the nSOS and bSOS adopt the same morphologies.

The morphologies of the LiTFSI-containing block polymers were characterized by synchrotron SAXS between 25–110 °C, to match temperature range over which we subsequently measured their ion conductivities (*vide infra*). Conductivity measurements are limited to the stated range to avoid thermal degradation during EIS characterization, evidenced by substantial differences in the conductivities measured on heating and cooling; within the range 40–100°C, measured conductivities in heating and cooling ramps are within 5% of one another. 1D-SAXS intensity profiles for the three LiTFSI-doped bSOS samples with M_{n} = 11.7–23.9 kg/mol and $f_{\mathrm{O/salt}}$ = 0.55–0.60 (Table 3.1) exhibit three or

more strong scattering maxima at (q/q^*) = 1, 2, 3,… (Figure 3.2a) at 90 °C, corresponding to LAM phases. This observation concurs with an earlier phase mapping study, which established the LAM phase window for salt-doped bSOS at r = 0.09 spans $f_{O/salt} \approx 0.55–0.75$.[49] SAXS analyses of control LiTFSI-loaded nSOS samples with M_n = 11.2–45.2 kg/mol with $f_{O/salt}$ = 0.47–0.56 (Table 3.1) also reveal the formation of LAM phases (Figure 3.2b), consistent with the formation of lamellae in nSOS at r = 0.09 when $f_{O/salt}$ = 0.42–0.59. In the case of nSOS_45.2_0.50, we note that the even order diffraction peaks (q/q^* = 2, 4, …) are extinct as expected for a sample of symmetric volume composition. This result corroborates the use of the above expression to calculate $f_{O/salt}$ and the assumed selective LiTFSI solvation in the O domains. In the final set of control samples, LiTFSI-doped nSO diblocks with M_n = 4.6 and 14.4 kg/mol and $f_{O/Salt}$ = 0.45–0.48 self-assemble into LAM (Figure 3.2c) in a manner consistent with earlier reports by Balsara and co-workers on related materials with M_n = 2.7–123 kg/mol.[82, 91] The order-to-disorder transition temperatures of all of these samples are far above 110 °C, as evidenced by the temperature-dependent SAXS profiles of representative bSOS, nSOS, and nSO with the lowest M_n values given in Figure A2.1.

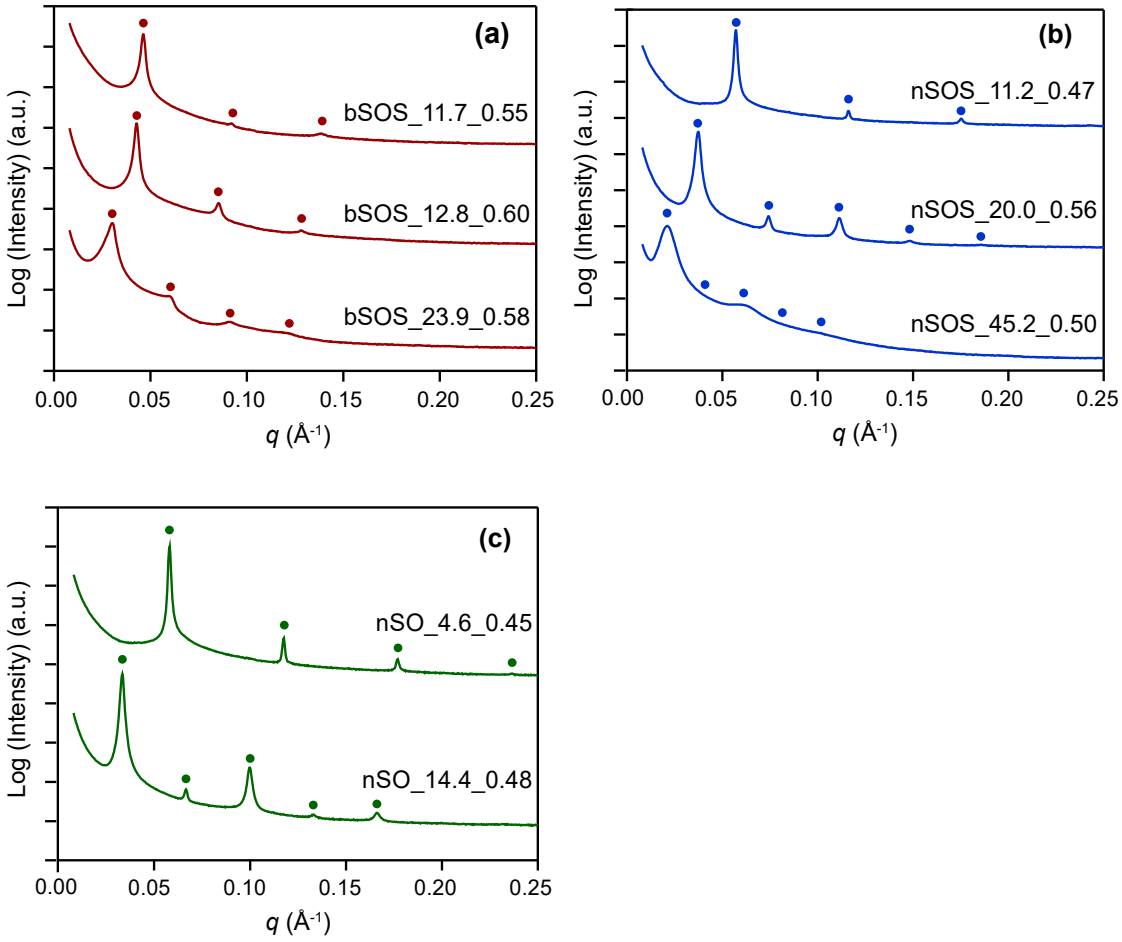

Figure 3. 2. Synchrotron SAXS profiles of (a) bSOS (b) nSOS and (c) nSO block polymers with r = 0.09 at 90 ºC. The circles denote the expected peak positions of lamellar morphology that occur at q/q^* = 1, 2, 3, 4...

Quantitative analyses of the SAXS data in Figure 3.2 reveal that the LAM *d*-spacings of this suite of samples are d_{LAM} = 10–21 nm at 90 °C, with the exception of the highest molecular weight sample nSOS_45.2_0.50 (Table 3.2). In each set of samples, the *d*-spacing increases with M_n as anticipated. Pairwise comparisons of bSOS_11.7_0.55 with nSOS_11.2_0.47 and bSOS_23.9_0.58 with nSOS_20.0_0.56 demonstrate that segment dispersity induces modest *d*-spacing dilation in samples of comparable M_n's or $f_{O,salt}$. While quantitative comparisons of these values are not possible due to somewhat imperfect matching of the samples, increased O segment dispersity qualitatively dilates d_{LAM} by < 30%. Given that a nSOS triblock may be conceptualized as a dimer of two nSO diblocks, one also expects a nSO diblock with $M_{n,nSO}$ to display d_{LAM} value to that of a nSOS triblock with molar mass $2M_{n,nSO}$.[57, 159] This correlation is borne out in that nSOS_11.2_0.47 and nSO_4.6_0.45 exhibit similar d-spacings of ~10.5 nm. Finally, we note that the qualitative breadths of the primary SAXS peaks in this sample set increase in the order nSO < nSOS < bSOS. Since the 2D-SAXS patterns for all samples are isotropic rings, the absence of any orientational order suggests that the peak broadening stems from differences in the microphase separated grain sizes. We return to the issue below.

Table 3. 2. Morphological and Conductivity Data for LiTFSI-doped bSOS, nSOS, and nSO block polymers with r = 0.09 at 90 ºC.

Sample	d_{LAM} (nm) [a]	F (10^{-3} Å^{-1}) [b]	L_r [c]	$T_{g,O/Salt}$ [d]	$T_{g,S}$ [d]	σ(90 °C) (10^{-5} S/cm) [e]	σ_n(90 °C) [f]
bSOS_11.7_0.55	13.6	1.65	26.1	-36	70	9.35±1.26	0.099±0.013
bSOS_12.8_0.60	14.7	1.68	23.7	-38	68	6.39±0.71	0.062±0.007
bSOS_23.9_0.58	20.7	2.96	9.54	-39	83	19.2±0.8	0.19±0.01
nSOS_11.2_0.47	10.6	1.14	48.6	-37	66	7.59±0.55	0.072±0.005
nSOS_20.0_0.56	16.8	1.78	19.6	-41	81	13.2±1.7	0.11±0.01
nSOS_45.2_0.50	30.5	6.02	3.18	-43	96	38.3±0.5	0.34±0.004
nSO_4.6_0.45	10.5	0.935	59.5	-37	63	4.51	0.045
nSO_14.4_0.48	18.6	1.53	20.5	-39	86	7.54	0.070
bPEOC	-	-	-	-42	-	172±0.3	-
PEO	-	-	-	-44	-	223±1	-

[a] Calculated from the primary scattering peak (q^*) where $d_{LAM} = 2\pi/q^*$ at 90 °C. [b] Calculated by fitting the primary scattering peak to a Voigt distribution after 5th order polynomial background correction of the 1D-SAXS linear Intensity versus q profiles. [c] reduced grain size $L_r = L/d_{LAM}$. = $2\pi K(Fd_{LAM})^{-1}$, where F (Å^{-1}) is the SAXS peak width, and the shape factor K = 0.93. [d] Determined by DSC. [d] Determined by DSC. [e] Average of triplicate samples. [f] Volume-fraction normalized conductivity σ_n(90 °C) = σ(90 °C)/[$f_{O/salt}$•σ_O(90 °C)].

Due to differences in the chemical compositions of the O segments in the bSOS and nSOS, namely the presence of ≤ 5.5 wt% carbonate functional groups, we first measured the ionic conductivities of LiTFSI-doped, high molecular weight bPEOC (M_n = 45.5 kg/mol) and O homopolymer (M_n = 35.0 kg/mol) at r = 0.09 in the range T = 40–100 ºC. Ion conductivity in these salt-doped high M_n polymers, which are expected to be partially entangled, is largely governed by local polymer segmental dynamics with negligible

contributions stemming from polymer chain diffusion ("vehicular diffusion").[75, 195] Thus, the bulk conductivities of these salty homopolymers represent baseline values against which the ion conduction dynamics of the relatively immobile O chains in microphase separated LAM-forming S/O block polymers may be compared.[91] The ion conductivity (σ) of the salty bPEOC measured by EIS are ~25% lower than those of the salty PEO over the entire temperature range as seen in Figure 3.3a and 3.3b, in spite of their very similar glass transition temperatures ($T_{g,bPEOC}$ = -42 °C and $T_{g,PEO}$ = -44 °C). Thus, we surmise that this difference in ionic conductivity stems from perturbations in the local segmental dynamics that arise from increased bPEOC chain rigidity imposed by the carbonate functionalities. Similar effects have been previously documented in salt-doped carbonate-containing polymer electrolytes.[196, 197]

Since temperature-dependent ion conductivities of the salty bPEOC and PEO are slave to the polymer segmental dynamics, we fit these $\sigma(T)$ data to according to the Vogel-Fulcher-Tammann–Hesse (VFTH) relationship:[98, 106, 192]

$$\sigma(T) = \sigma_0 exp\left[\frac{B}{R(T - T_0)}\right]$$

where σ_0 is the infinite temperature conductivity, B is a pseudo-activation energy for ion motion, and T_0 is the Vogel temperature that is $T_0 = T_g - 50$ K, where T_g is the glass transition temperature of the conductive phase. We note that the conductivity of these homopolymer samples do exhibit sample history-dependence below 50 ºC, due to low degrees of crystallinity with broad melting temperatures centered near $T_m \approx 28$ ºC and 47 °C measured by DSC of salt-doped bPEOC and PEO respectively (see Appendix Figure

A2.2). Consequently, we fit the conductivity data using the VFTH equation to obtain σ_0 and B between 55–100 °C (see Figure A2.3 for representative data fits). The distribution of B = 8.69–9.20 J/mol (see Table A2.1) across the salty PEO and bPEOC suggests that the local segmental dynamics are comparable and that the origins of the observed conductivity difference are quite subtle.

The temperature-dependent ionic conductivities of S/O block polymers salt-doped at r = 0.09 were subsequently measured in triplicates by EIS in the range T = 40–100 ºC. For comparison purposes, the values of σ(90 °C) for each sample are given in Table 3.2. Even though the conductivity of LiTFSI-doped bPEOC is lower than that of PEO, the measured conductivities of the bSOS samples are comparable or greater than those of the nSOS samples with comparable M_n and $f_{O/salt}$ values. VFTH fits of $\sigma(T)$ data again were conducted in the range 55–100 °C, in order to avoid issues related to low levels of O/salt domain crystallinity. In each of the bSOS, nSOS, and nSO series, the conductivities of the salt-doped block polymers generally increased with increased molar mass (Figure 3.3 a–c). While this trend coincides with a small decrease in T_g for the samples increasing M_n (Table 3.2), the documented ≤ 3% variation in O/salt domain T_g is likely not a major contributor to the observed M_n-dependent conductivity trend. Furthermore, inspection of the pseudo-activation energy barriers (B) for ion motion in these samples (Table A2.1) reveals no systematic trends. This last observation suggests that ion transport dynamics are not appreciably altered by chain connectivity effects (diblock *versus* triblock) or triblock O center segment dispersity.

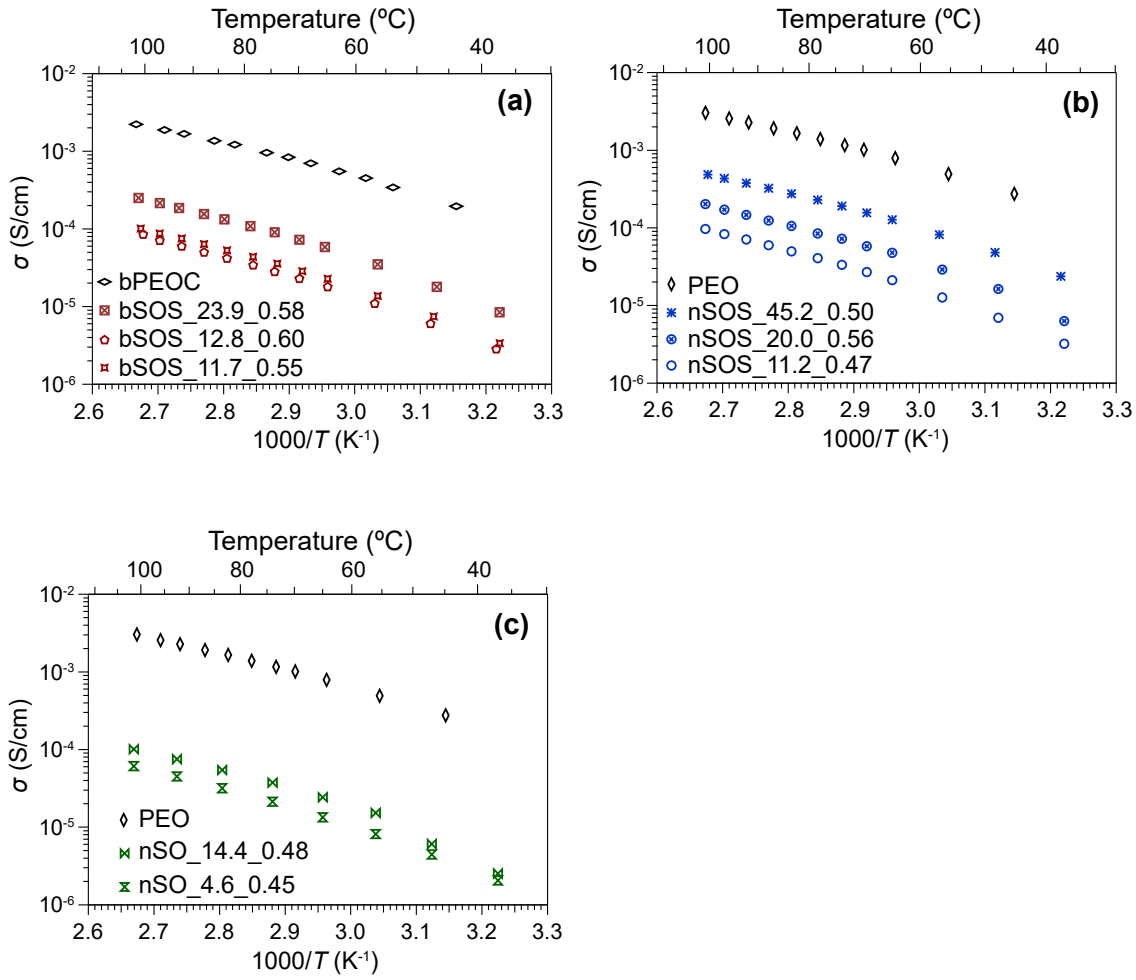

Figure 3. 3. Temperature dependent ionic conductivity at $r = 0.09$ of salt-doped (a) bSOS (b) nSOS and (c) nSO block polymers with the black diamonds represents the conductivity of the corresponding homopolymers.

To facilitate more quantitative comparisons of the conductivities of these various salty nSO, sSOS, and bSOS samples, we calculated the volume-fraction normalized conductivity $\sigma_n(T)$ (sometimes also called a "morphology factor") as

$$\sigma_n(T) = \frac{\sigma(T)}{\sigma_O(T) \cdot f_{O/Salt}}.$$

The denominator in this expression represents the maximum conductivity that could be expected from the salt-doped block polymer, and thus $\sigma_n(T)$ indicates the deviation from the ideal conductivity. This $\sigma_n(T)$ further takes into account differences in the salt-doped homopolymer conductivities, which allows more detailed comparisons of the bSOS and nSOS conductivity data. For randomly-orientated lamellar grains with minimal interfacial width between the conducting and insulating domains, the "effective medium theory" of Sax and Ottino suggests that one should expect $\sigma_n(T) = 2/3$ as a consequence of the two-dimensional conducting microdomains of a LAM morphology.[103] However, the calculated $\sigma_n(90\ °C) = 0.045–0.34$ for the samples listed in Table 3.2 are much lower than the ideal value. Numerous recent studies have ascribed such deviations due to the tortuosity of the conductivity pathways,[138-141, 147] grain boundaries in the self-assembled morphology,[76, 83, 117, 149] and interfacial mixing,[81, 109, 192, 198] amongst other effects. A plot of the $\sigma_n(90\ °C)$ versus total block polymer M_n is given in Figure 3.4, including selected conductivity data for nSO polymers reported by Panday et al.[82] and Yuan et al.[91] The M_n values of the diblocks were doubled in the plot in Figure 3.4 to enable comparison of the nSO diblock data with that of the triblocks, since the *d*-spacing and melt segregation strength of a nSO diblock with $M_{n,nSO}$ is comparable to that of a nSOS triblock with $M_{n,nSOS} \approx 2M_{n,nSO}$. We

find that the σ_n(90 °C) values determined for the two nSO samples in this work agree with well with previous literature reports.[82, 91] Figure 3.4 clearly indicates two regimes of conductivity behavior: (1) architecture- and dispersity-independent low conductivities of σ_n(90 °C) ≈ 0.10 when $M_n \leq 15$ kg/mol, and (2) 2-3 fold higher σ_n(90 °C) values for triblocks when $M_n \geq 20$ kg/mol with a modestly higher value for bSOS at a similar M_n.

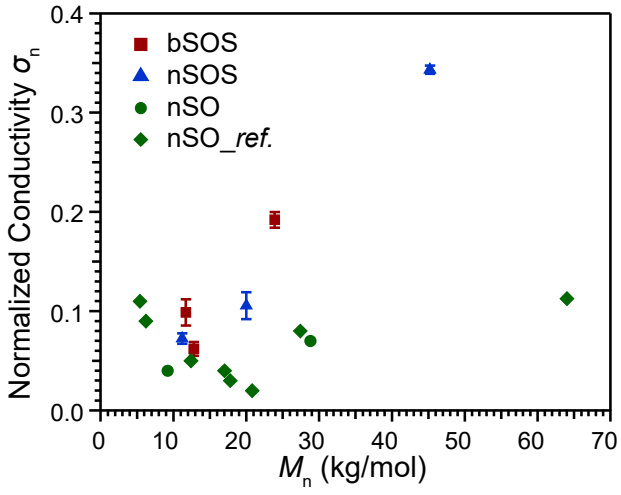

Figure 3. 4. Normalized conductivity σ_n(90 ± 2 °C) for LiTFSI-doped S/O block polymers plotted as function M_n. Error bars for the bSOS (*squares*) and nSOS (*triangles*) data represent the standard deviation from triplicate conductivity measurements. Normalized conductivity of nSO combines measurements in this study (*circles*) and results recalculated from Panday et. al.[82] and Yuan et. al.[91] (*diamonds*), where M_n values for the nSO polymers are doubled to facilitate comparisons with the triblock polymers.

3.5. Discussion

The observation of two M_n-dependent conductivity regimes in Figure 3.4 for the S/O diblock polymers, coupled with the much higher σ_n(90 °C) values for bSOS and nSOS, as compared to nSO is not readily accounted for by explanation provided thus far in the literature. Enhanced ion conductivity with increased total block polymer M_n was previously reported in narrow dispersity diblock polymers (nSO), however, substantial increases in the measured conductivity are not observed up to a threshold $M_{n,\,nSO} \approx 60$ kg/mol.[82, 91] This effect has been rationalized in terms of M_n-dependent changes in lithium salt solvation,[199-201] ion distribution within the O microdomains,[94, 202, 203] polymer segmental dynamics[113-116] due to the microphase separation with non-conductive segments. Undoubtedly, the influence from the glassy S domain dynamics and possible segregation strength-dependent interfacial mixing is most prominent at low molecular weights, as reflect by the decreasing O/salt domain T_g with increased $M_{n,total}$ (Table 3.2). However, these rationalizations do not fully account for the conductivity differences between SO diblocks and their equivalent SOS triblocks. We note that increased O segment dispersity in bSOS only minimally augments the ionic conductivity of the salt-doped nSOS control samples, even though one might have anticipated that the dispersity-driven differences in molecular packings[31, 33] in the morphologies of bSOS[49] might lead to differences in lithium salt solvation and O segmental dynamics.

Chintapalli et al. first pointed out the importance of grain structure in the ionic conductivities of nSO diblock polymers, whereby increased conductivities were documented in LAM samples that exhibit poor long-range translational order derived from rapid thermal quench processing[117] or increased lithium salt loadings.[76] In order to understand the former observations, they estimated the microphase separated grain sizes (L) in their nSO samples by a Scherrer analysis of the associated SAXS data. According to this analysis, L is inversely proportional to the full-width at half-maximum for the primary SAXS peak. In order to facilitate comparisons between polymers with different d-spacings, they calculated the average number of periodic repeating motifs per grain as a reduced grain size (L_r) as $L_r = L/d_{LAM}$. In two nSO samples with varying r-values, they determined that the $\sigma_n(90\ °C) \sim \exp(-L_r)$ varied with salt loading. More recent work by Chakraborty *et al*. has affirmed similar effects in related poly(polyhedral oligomeric silsesquioxane acrylate)/PEO triblock polymers with temperature-dependent changes in grain size.[204]

In view of our observation that the principal SAXS peak breadth apparently increases in the order nSO < nSOS < bSOS, which is coincident with the observed trend in $\sigma_n(90\ °C)$, we applied the corrected quantitative analysis of Chakraborty et al. to the present sample set.[204] More specifically, we fit the q^* peaks in the SAXS data in Figure 3.2 with a Voigt distribution and a q-dependent 5th order polynomial background to quantify the peak full-width half-maximum (F) in Å^{-1}. The LAM grain size may then be estimated as $L = 2\pi K/F$ where $K = 0.93$ is the shape factor for the lamellar grains,[205] since SAXS peak broadening due to the X-ray wavelength uncertainty in these data obtained using a monochromatic synchrotron X-ray source is minimal.[76, 206] We note that our analysis crucially relies on 2D-

SAXS data comprising isotropic ring patterns, indicative of a lack of preferential orientation of the domains that may spuriously lead to peak broadening. In other words, the sample is assumed to contain randomly oriented lamellar grains as the estimated grain sizes ($\lesssim$ 100 nm) are orders of magnitude smaller than the block polymer SAXS sample thickness (~1 mm).[207, 208] From the plot in Figure 3.5a, we see that the reduced grain size L_r rapidly decreases with increasing M_n and that the steepness of this drop off depends on chain connectivity, and to a lesser extent dispersity. That is to say, bSOS samples exhibit smaller reduced grain sizes than nSOS and nSO.

On plotting the σ_n(90 °C) versus L_r as in Figure 3.5b, we observe that all of the grain size-dependent conductivity data apparently collapse onto a single curve that shows that the conductivity substantially increases when $L_r \lesssim 10$. The observed dependence σ_n(90 °C) ~ exp(–L_r) is qualitatively similar to that reported earlier by Chintapalli et al. for two low-M_n nSO diblock samples.[76]

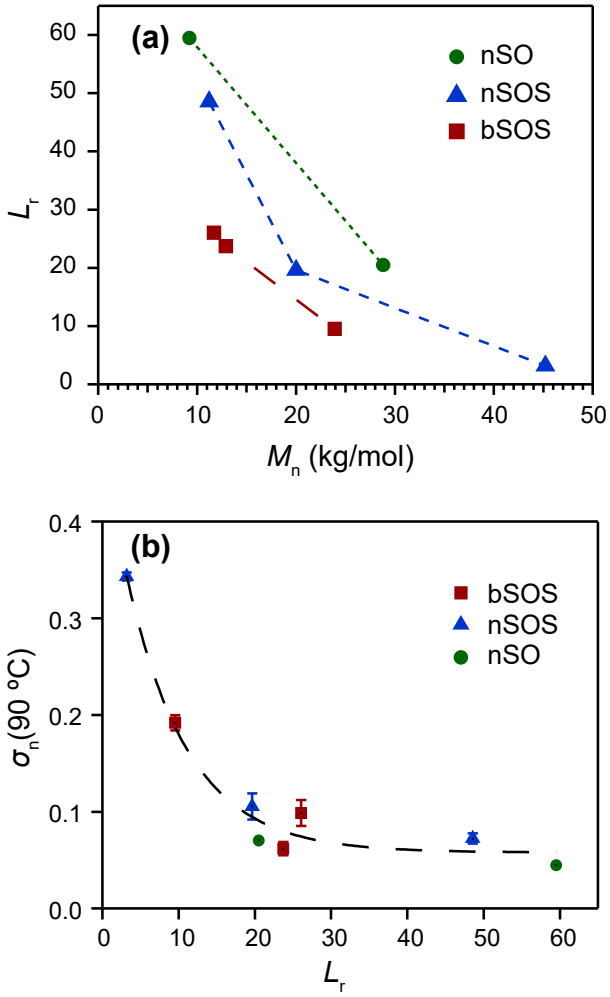

Figure 3. 5. (a) Reduced grain size (L_r) of salt-doped nSO, nSOS and bSOS versus total block polymer M_n. M_n of nSO polymers are doubled so as to allow for a more careful comparison to the triblock samples. (b) σ_n(90 °C) for bSOS, nSOS, and nSO with $r = 0.09$ as a function of the normalized grain size, L_r. The dashed line is an exponential fit intended to serve as a guide to the eye.

The data presented in Figure 3.5b suggest that poor long-range translational order in self-assembled block polymer assembly result in increased ionic conductivities. This result is somewhat counterintuitive given earlier work on block polymer electrolytes that suggests that the presence of numerous grain boundaries impedes ion motion in the conductive microdomains.[138, 140, 141, 147] As compared to a monodomain LAM sample, the presence of grain boundaries does increase tortuosity and decrease the conductivity in two-dimensional conductive layers.[138, 141, 145] However, the ionic conductivities reported herein were obtained from macroscopic block polymers samples with dimensions that are much larger than their constituent, randomly-oriented LAM grains. Consequently, our measured conductivities must depend on inter-grain transport and the structure of the grain boundaries in these lamellae-forming samples.[146, 149, 209] In LAM block polymers, the most commonly observed grain boundaries are twist boundaries and tilt boundaries. Twist boundaries are co-continuous structures that locally adopt a Scherk hyperbolic minimal surface structure which has been identified in TEM studies of block polymer samples[118, 120] and recently fabricated using directly self-assembly of block polymer thin films.[121] Tilt boundaries also preserve the connectivity of the LAM grains, albeit with a change in the orientation of the lamellar normal vector, as long as the angle between the lamellar normal is not 90°. Thus, only the perfect T-junctions (tilt boundaries with a 90° angle between lamellar normals) entirely disrupts grain connectivity and potential intergrain transport.[119, 210] Therefore, a majority of the grain boundaries in the two-dimensional LAM morphology[146, 148, 149] are conductive such that reducing grain size effective produces a disorganized bicontinuous morphology[77, 185, 198] that exhibits less tortuous ion conducting

pathways as depicted in Figure 3.6a. The findings present here suggest two previously unrecognized means of decreasing the grain sizes of ion conducting materials: (1) embedding the conductivity domain in the center of an ABA-type triblock, and (2) incorporation of a disperse center segment.

The question naturally arises as to why the triblock architecture results in a more defective LAM morphology with better transport characteristics. Below the order-to-disorder transition temperature of a microphase separated block polymer, grain boundaries in the morphology are kinetically trapped defects that arise from sample history-dependent grain nucleation and growth. The generally slow kinetics of defect removal in S/O block polymers by high temperature annealing depends sensitively on chain diffusivity within the segregated melt both parallel and normal to the LAM phase interfaces.[211-213] Since chain diffusion normal to the interface incurs a substantial energy penalty associated with unfavorable segment mixing, predominantly in-plane chain diffusion occurs. Furthermore, the SOS triblock chain diffusivity is substantially more restricted as compared to that of SO diblocks for two distinct reasons (Figure 3.6b). First, SOS triblock chain diffusion requires cooperative motion of the two S end segments,[214] which may not be situated in the same microdomain (i.e., a "bridging" conformation). Furthermore, the O mid-segments may form interfacially trapped entanglements ("knotted loops"),[215, 216] for which chain escape requires S end segment pull out in the segregated morphology that is energetically costly due to unfavorable segment mixing. For these reasons, we speculate that the thermal annealing step conducted prior to our conductivity measurements fosters greater

elimination of the grain boundaries in the nSO samples as compared to the nSOS and bSOS. Thus, the grain sizes in the triblock samples are smaller and their conductivities are higher.

Triblock segment dispersity apparently further stabilizes grain boundaries, as the continuous O segment dispersity in bSOS results in both chain length and composition heterogeneities in the samples.[31, 33] In order words, bSOS samples comprise chains that exhibit a broad distribution of preferred interfacial curvatures. Consequently, these chains can synergistically pack into arrangements that stabilize grain boundaries with reduced packing frustration[119, 210] in a manner not possible for nSOS (Figure 3.6c). Recent self-consistent mean-field theory calculations support this view, in that segment dispersity more readily allows the formation of structures akin to tilt boundaries.[217] Thus, bSOS polymers exhibit the smallest grain sizes due to the combination of the triblock architecture and O block dispersity as compared to its narrow dispersity analogs. These effects manifest in the conductivity data plotted in Figure 3.4, especially, the conductivity increase onset at lower total M_n for the triblocks.

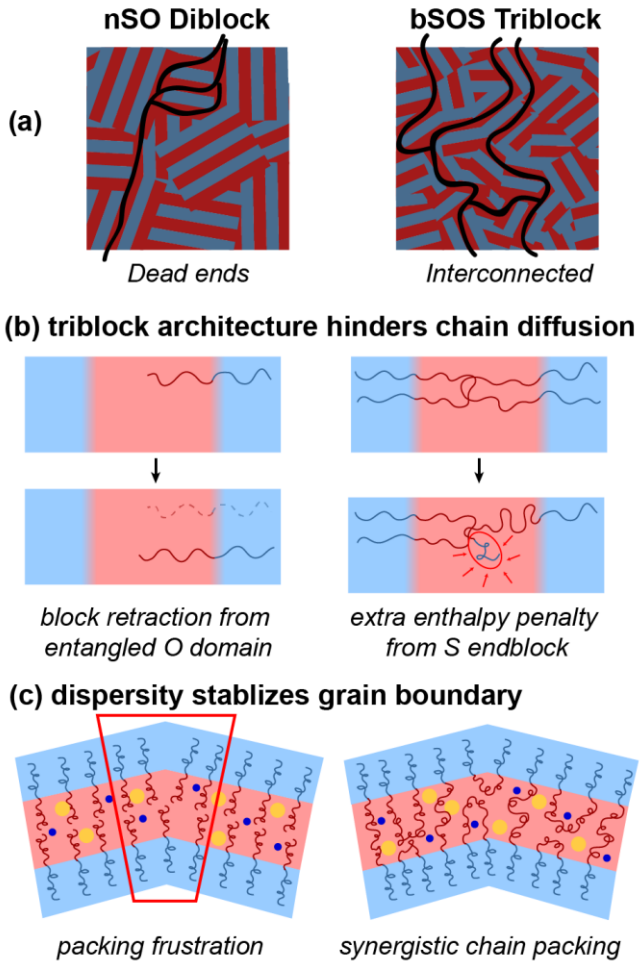

Figure 3. 6. (a) Decreased grain size in bSOS polymers leads to more interconnected channels for lithium ion transport, as compared to nSO diblocks. This observation likely stems from: (b) hindered diffusion due to cooperative S chain motion and the presence of knotted loops in the O domain associated with the triblock architecture, and (c) grain boundary structure stabilization by synergistic packing of broad dispersity O segments that relieves packing frustration.

3.6. Conclusion

We investigated the ionic conductivities of salt-doped SOS triblock polymers comprising LiTFSI-doped broad dispersity O blocks with $Đ_O \sim 1.45$ and $r = 0.09$ and narrow dispersity insulating S blocks with $Đ_S < 1.18$. Comparative structure-conductivity relationships were developed between three lamellae-forming, salty bSOS polymers with near symmetric volume fractions ($f_{O/Salt} = 0.55 – 0.60$) and $M_n = 11.7–23.9$ kg/mol and narrow dispersity nSO diblock and nSOS triblock polymer analogues with similar $f_{O/salt}$. EIS studies demonstrated that the ionic conductivities in each of these electrolytes series increase with increasing $M_{n,total}$. The broad dispersity bSOS_23.9_0.58 displays a conductivity at 90 ºC of 0.19 mS/cm ($\sigma_n = 0.2$), which is two-fold higher than that of a nSOS sample of comparable M_n and salt-loading. For samples having similar M_n's, the volume-fraction normalized conductivities σ_n(90 °C) across these electrolyte series increase in the order bSOS > nSOS > nSO with substantial increases in conductivity when $M_n \gtrsim 20$ kg/mol. We rationalize these findings in the context of architecture- and dispersity-induced changes in the lamellar grain sizes in these materials, which are quantified using a Scherrer analysis of synchrotron SAXS data for the salt-doped samples, whereby smaller grain sizes lead to higher ionic conductivities. These studies highlight the importance of grain size engineering in optimization of the ionic conductivities of block polymer-based electrolytes energy applications.

Chapter 4. Flexible Nanoporous Materials from Matrix Domain Etching of Block Polymers*

** This work was done in collaboration with Han Xiao and Christopher J. Ellison.*

4.1. Motivation

The development of scalable and robust methods for fabricating nanoporous polymeric materials impacts their applications in microelectronic device manufacture,[157, 218-221] as size-selective separations and ultrafiltration membranes,[143, 144, 222] solid catalysts,[223-226] templates for porous inorganic materials,[227-230] and drug delivery vehicles.[231] While the fabrication of an isoporous polymer structure is crucial to many of these applications, periodic long-range translational order in the pore structure is often not an absolute requirement. The required materials attribute in many applications is that the pores are continuous and macroscopically percolate through the structure. As compared to porous ceramic and metallic materials, the pore sizes, pore wall functionalities, [232, 233] interfacial wettability[234] and overall mechanical properties of nanoporous polymers may be readily tailored by judicious selection of their constituent monomers, their overall volume fractions and their processing protocols.[235] The ready melt and solution processabilities of monomeric or polymeric precursors to these porous media further extend the utility of the resulting materials, by allowing their fabrication in formats ranging from monoliths to nanometer-thick coatings.

An enticing design strategy for producing tailored nanoporous materials with controlled pore dimensions, pore functionalities, and tunable properties relies on block polymer self-assembly.[125, 232] Block polymers, which derive from covalently tethering two or more chemically dissimilar polymer segments, thermodynamically microphase separate into spherical (S), hexagonally-packed cylinder (HEX), gyroid (G), and lamellar (LAM) nanostructures with tunable domain dimensions dependent on overall polymer molecular weight.[3, 5] Incorporating mechanically robust (e.g., high T_g or crosslinkable) segments with degradable segments into these nanostructured polymers allows development of porosity by selective chemical etching of the degradable nanodomains.[122-124] Register and co-workers first demonstrated the formation of polymer-based nanolithography templates based on ozonolysis of the PB domains of a self-assembled poly(styrene-*block*-butadiene) (PS-*b*-PB) thin film.[218] By a conceptually-related strategy, Hillmyer and co-workers produced isoporous PS monoliths with 15 nm diameter cylindrical pores, by flow aligning a HEX-forming poly(styrene-*block*-lactide) (PS-*b*-PLA) and degradation of the minority phase PLA cylinders by saponification. This approach has further been extended using degradable poly(ether)[236] and poly(siloxane)[127, 237] segments. These methods produce materials with ordered nanopore arrays, with the expense of non-trivial processing steps to produce aligned morphologies.[125, 219]

Selective chemical etching of bicontinuous block polymer morphologies enables access to useful high surface area nanoporous materials, while avoiding arduous processing steps. Both ordered and disordered bicontinuous nanoporous polymers may be derived from microphase separated double gyroid morphologies[126-128] and bicontinouous

microemulsions,[129] respectively. However, these privileged phases only form over narrow composition and molecular weight ranges that limit synthetic access and ultimate porosity.[128] More robust access to polymers with percolating, disorganized pores has been recently reported by polymerization-induced microphase separation (PIMS),[130, 131, 238, 239] crosslinking disordered states of diblocks above their order-to-disorder transition temperatures,[132, 240, 241] and through the formation of randomly end-linked networks (RECNs).[133]

A further limitation of many of the above routes to nanoporous polymers is that the observed porosity is typically 50% or less, as consequence of the block polymer composition presumed to furnish sufficient mechanical integrity. Even though HEX morphologies of block polymers comprising structurally robust cylinders in a degradable matrix would permit access to higher porosity nanostructures, conventional wisdom suggests that matrix etching in such phases will lead to materials that fall apart. Indeed, such studies have been reported as a means of producing narrow dispersity nanotubes[134, 135] and polymer nanofibrils.[136, 137] Contrary to this conventional wisdom, we herein demonstrate selective domain etching of unaligned HEX morphologies of block polymers with a degradable matrix phase yields mechanically robust, high porosity polymers with defined pore sizes.

4.2. Observations & Analysis

By a previously reported sequential anionic polymerization and tin-catalyzed ring-opening transesterification polymerization (ROTEP) sequence, we synthesized a PS-*b*-PLA diblock (Figure 4.1a) with total molecular weight M_n = 41.1 kg/mol ($Đ = M_w/M_n$ =

1.24) and a minority PS volume fraction f_{PS} = 0.21 (see Appendix Figure A3.1 (a) and Fiugre A3.2 (a-b) for synthesis and characterization details). Synchrotron SAXS analysis of a 0.7 mm-thick sample compression-molded at 120 °C exhibits a poorly ordered HEX-morphology (Figure 4.1b), likely due to the strongly segregated nature of this high molar mass polymer. Immersion of this material into 2.5 M NaOH in MeOH/H_2O (20:80 *v/v*) at 45 °C for 12 h completely degrades the PLA therein, evidenced by the disappearance of PLA proton resonance at δ = 5.1–5.3 ppm in Figure A3.2 (c) of a vacuum-dried sample after etching and the exact mass loss from the vacuum-dried PS monolith of 80.9 wt% as compared to the 81.3 wt% expected theoretically. Surprisingly, the resulting water-filled PS monolith retains its original shape with a clear, slightly bluish appearance (Figure 4.1c) and can be readily handled. This water-imbibed monolith was cryofractured in $N_2(l)$, vacuum dried, coated with a 2 nm thick Ir layer, and imaged by SEM to reveal a porous network of discrete fibrils in Figure 4.1d. While the vitreous nature of the PS domains preserves the porous nanostructure after PLA removal, the low molecular weight of the PS segment (M_n = 7.5 kg/mol) confers little mechanical strength to the material for practical applications. Nonetheless, this finding clearly establishes that the cylinders in this polydomain HEX morphology are sufficiently interconnected in the unaligned melt morphology to yield a nanoporous polymer by matrix domain etching.

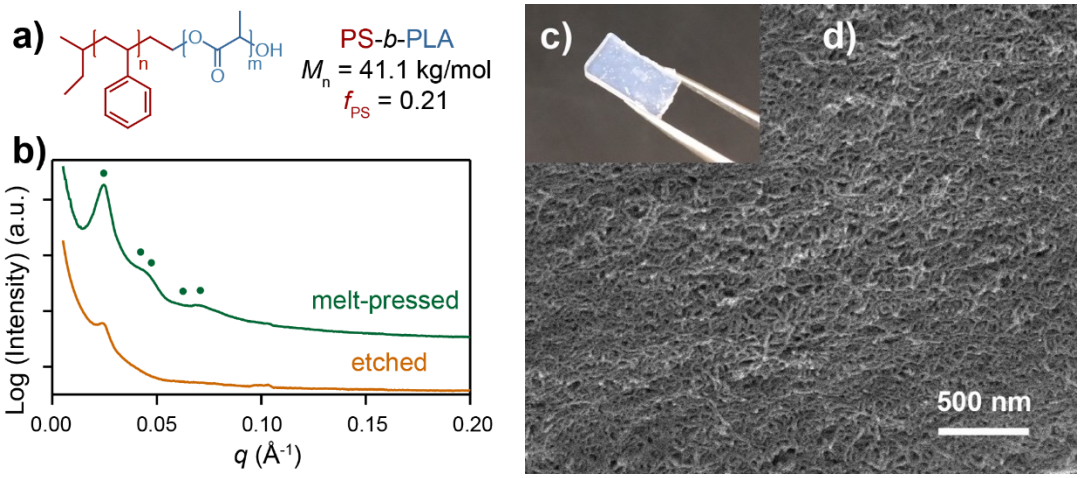

Figure 4. 1. (a) Molecular structure of PS-*b*-PLA block polymer synthesized via tandem anionic and ring-opening transesterification polymerization. (b) SAXS patterns of a compression-molded PS-*b*-PLA sample before (*green*) and after (*orange*) PLA etching. Markers indicate the positions the expected peaks hexagonally-packed cylinders with q^*, $\sqrt{3}\ q^*$, $\sqrt{4}q^*$, $\sqrt{7}q^*$, $\sqrt{9}q^*$…at $q^* = 0.0244$ Å^{-1}. The etched PS-*b*-PLA sample (*orange*) exhibits only a single, broad correlation peak at the same q^* position before etching with weak scattering signals. (c) Picture of the water-filled porous PS sample after etching and (d) SEM images of the cyrofractured sample showing interconnected PS cylinders.

Encouraged by this unexpected initial finding, we sought to develop a melt-processable HEX-forming block polymer that would lead to a tougher material upon matrix domain etching. Consequently, we opted to investigate the fabrication of nanoporous polymers derived from poly(isoprene-*block*-lactide) (PI-*b*-PLA) in which the PI cylinders are thermally crosslinked during melt processing by dicumyl peroxide (DCP) to enhance their rigidity (Figure 4.2a). By a literature procedure,[242] we synthesized a PI-*b*-PLA diblock with

M_n = 32.0 kg/mol (($Đ = M_w/M_n$ = 1.17) and PI volume fraction f_{PI} = 0.22 (see Figure A3.1 (b) and Figure A3.3 for detailed synthesis and characterization). This polymer was blended with DCP by co-dissolution in C_6H_6, followed by freeze-drying the frozen mixture under vacuum, yielding the DCP content of 15.7 wt% determined via ^{1}H NMR. The resulting mixture was initially compression-molded at 60 °C to agglomerate the polymer into a 0.7 mm thick film above the glass transition temperature of the PLA domain ($T_{g,PLA}$ = 42 °C, decreased from 58 ºC by DCP blending) without activating the crosslinker, followed by PI-domain crosslinking under hydraulic compression (40 psi) at 155 °C for 1 h. SAXS analyses presented in Figure 4.2b demonstrate the formation of a HEX morphology by this PI-*b*-PLA/DCP blend prior to crosslinking, evidenced by scattering maxima at $(q/q^*)^2$ = 1, 3, 7, 9, 12, 13, etc. with domain spacing d = 30.7 nm (q^* = 0.0204 Å^{-1}). Crosslinking induces a small decrease in the d-spacing to d = 29.3 nm with some loss of long-range order evidenced from smearing of the higher order SAXS peaks (Figure 4.2b), likely due to the expected volume contraction on conversion of van der Waals contacts to covalent bonds formed between the PI chains. Comparative SAXS analysis of the neat PI-*b*-PLA diblock (Figure A3.4) reveals that the incorporation of DCP prior to crosslinking drives 3% reduction in the observed HEX d-spacing, indicating that DCP compatibilizes the PI and PLA segments by non-selectively partitioning into both domains.[243]

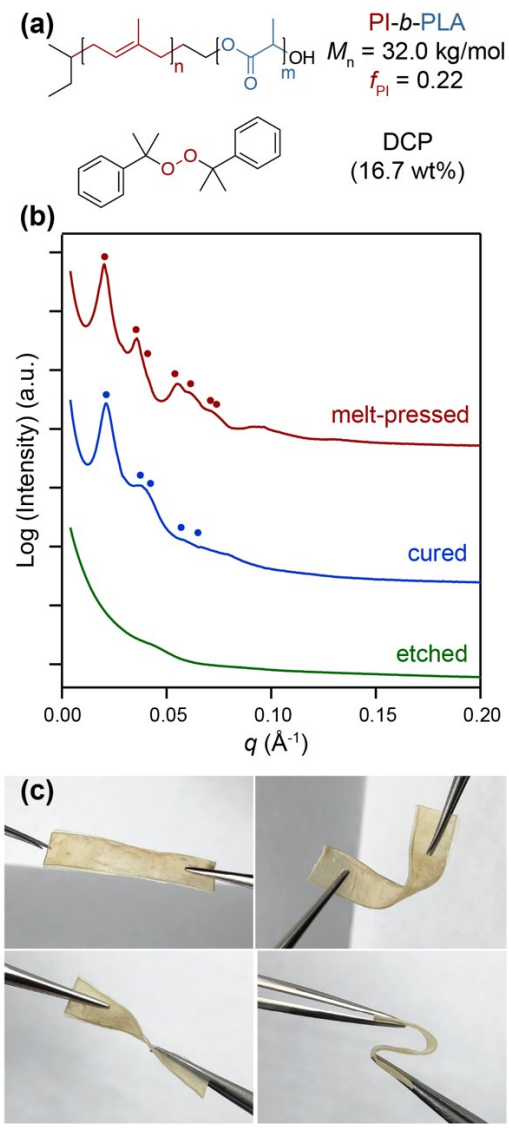

Figure 4. 2. (a) Chemical structure of PI-*b*-PLA and the thermal crosslinker DCP. (b) SAXS patterns of PI-*b*-PLA block polymer loaded with 15.7 wt% DCP before (*red*) and after (*blue*) thermally-activated crosslinking of the PI domains. Markers indicate positions of the expected peaks for hexagonally-packed cylinders with q^*, $\sqrt{3}\,q^*$, $\sqrt{4}q^*$, $\sqrt{7}q^*$, $\sqrt{9}q^*$… The wet PI-*b*-PLA sample (*green*) after etching exhibits only a single, broad correlation peak at $q^* = 0.0428$ Å^{-1} without strong scattering signals. (c) Photos of etched and water-imbibed flexible nanoporous PI that can be bent, folded and twisted.

Etching of the crosslinked PI-*b*-PLA film with 2.5 M NaOH in MeOH/H_2O (20:80 *v/v*) solution at 45 ºC for 12 h followed by immersion in DI water to remove the base yields a flexible, water-imbibed nanoporous PI (npPI) material that retains its original shape, which may be bent, twisted and folded as pictured in Figure 4.2c. Thus, this wet npPI monolith does not simply fall apart as anticipated by conventional wisdom, since the cylinders apparently remain interconnected. However, monoliths thus prepared become brittle on drying. Gravimetry reveals an average mass loss of 81.0±1.0 wt% over five replicates in the dried npPI relative to the original material. To better quantify the mass loss corresponding to etched PLA and minimize the effect of the large quantity of DCP in use, etching was performed separately on crosslinked PI-*b*-PLA samples first swelled in THF at 55 ºC to extract residual DCP and cross-linking byproducts (see Appendix 3 for details). After etching the extracted crosslinked PI-*b*-PLA under the same conditions as above, a mass loss of 80.3±0.2 wt% with respect to the extracted crosslinked diblock was derived via gravimetric measurements in triplicate, from which we deduce that there is 12.6±0.8 wt% residual PLA in the dry polymer monolith based on the PLA weight fraction of 82.8 wt% in the diblock precursor. Thermogravimetric analysis (TGA) corroborates the presence of ~12 wt% PLA in the dried npPI materals that etched from the extracted polymer sample (Figure A3.5). Increasing the chemical etching time to 2-3 d did not further reduce the PLA content. We surmise that some of the DCP initiator crosslinks the PLA chains by H-atom abstraction and generation of α-enolic radicals,[244, 245] which may lead to its covalent incorporation at the surface of the crosslinked PI cylinders as suggested from the FTIR spectra (Figure A3.6) of the etched monolith.

The crosslinked npPI monoliths imbibed with water were cryofractured and cross-sectionally imaged by SEM (Figure 4.3a and 4.3b) to reveal a porous structure with interconnected polymer fibrils, which is akin to that previously reported in nanoporous PI derived from a crosslinked and etched bicontinuous microemulsion.[129] Quantitative image analyses via ImageJ on Figure 4.3b indicate the presence of discrete fibers with an average diameter of 16 ± 2 nm from 40 measurements of manually selected isolated fibrils to avoid merged cylinder bundles. This fibril diameter is in agreement with the expected diameter of the PI cylinders of 17.4 nm estimated from the SAXS-derived d = 29.3 nm of the crosslinked PI-*b*-PLA and the total volume occupied by the crosslinked PI and residual PLA in the monolith (see Figure A3.7 for calculation details). In spite of their origin in an ordered block polymer morphology, these fibrils are randomly oriented with scant signs of hexatic ordering and some degree of fiber agglomeration and collapse. The last finding is consistent with the SAXS pattern for the etched, water-filled polymer network (Figure 4.2b), which shows only a broad correlation peak with no signs of Bragg scattering. Quantitation of the mass loss on water removal by drying the porous fibrillar network leads us to estimate the void fraction therein to be 55 ± 4 %. This porosity estimate is lower than the f_{PLA} = 0.78, which further suggests that the partial collapse of the cylinders on PLA etching and water removal. We note that this porosity is comparable to reported by Vidil *et al*. from etching melt-disordered block polymers.[132]

The compressive mechanical properties of the wet npPI samples were characterized by 10 consecutive compression-release cycles with a maximum 20% applied strain at a strain rate 0.02 s^{-1} (Figure 4.3c). We observe notable hysteresis after the first compression cycle,

which likely arises from irreversible plastic deformation and possible collapse of the structure. From the slope of the linear regime of the 2nd compression stress-strain curve, we calculate that the compressive modulus of the etched polymer is 95.5 ± 23.9 kPa. The compression profiles obtained in cycles 2-10 exhibit a sharp upturn between 15-20 % strain, which coincide with what observed in fibrillar network mechanics documented in soft fatty tissue.[246] The fibrillar npPI network mechanics continue to evolve in subsequent cycles such that the peak normal stress decreases by 26 ± 9% after 10 cycles likely comes from some network rupture and possible water loss.

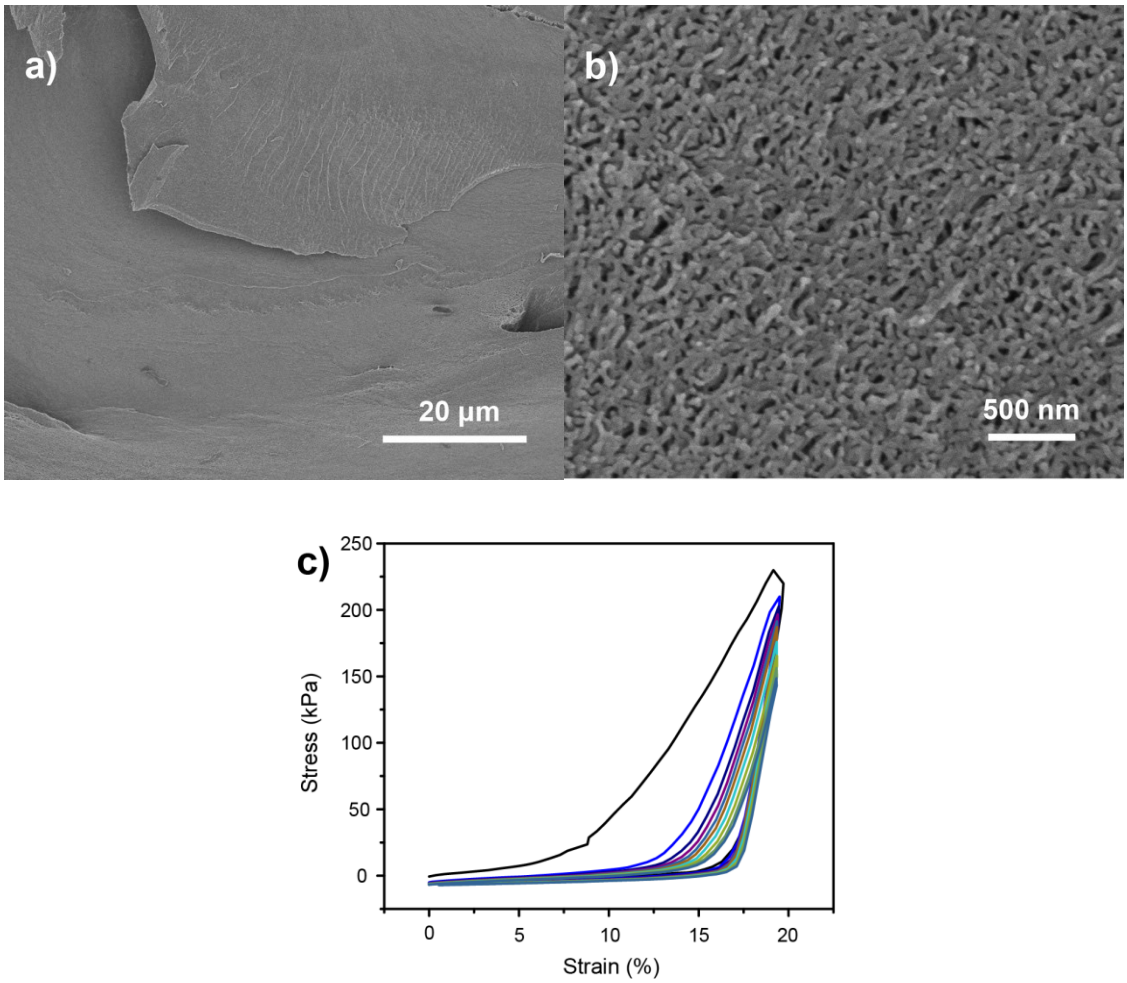

Figure 4. 3. SEM images of the cross-section of cryofractured sample under (a) low magnification and (b) high magnification showing the interconnected cylinder fibrils and the porous structure. (c) Cyclic compression of the etched IL polymer. Compression modulus was calculated from the two linear regimes of the 2nd compression curve being 95.5 ± 23.9 kPa and 3.58 ± 0.31 MPa respectively. The maximum normal stress decreases by 26 ± 9 % after 10 compression cycles at a 20% maximum strain. Data and the corresponding error are calculated from five parallel characterizations.

In order to quantify the effective pore size in the npPI and demonstrate their percolation through a macroscopic sample, we examined its performance as a semi-permeable membrane for the separation of a mixture of five narrow dispersity poly(ethylene oxide) (PEO) standards having M_n = 0.4–35 kg/mol. We set up a U-tube diffusion cell (see Appendix A3 for details) at 22 °C, wherein the 0.35 mm thick npPI membrane was situated between a reservoir containing pure de-ionized water and one containing a mixture of PEO standards (the right and left arms of the U-tube, respectively, in Figure A3.8). The initial experiment in pure DI water revealed continuous osmotically-driven water transport evident from increased water level difference. However, penetration of the PEO molecules of all molar masses are low (< 5 wt%) and do not evolve significantly over time. Given the presence of residual PLA in the npPI sample which could hydrolyze to yield carboxylic acids lining the fibrillar network surface that bind PEO,[247] we speculated that the impeded PEO penetration stems from PEO adsorption within the material that clogs the membrane. Consequently, we conducted the same U-tube diffusion experiment replacing the de-ionized water with 1.0 M KOH(*aq*) (pH 14) to promote deprotonation of any acidic functionalities. This condition could additionally promote electrostatic repulsions between the cylindrical fibrils that lead to enhanced porosity.

Figure 4.4a depicts the time-dependent PEO concentration profiles determined by quantitative SEC analyses of aliquots taken from both arms of the U-tube (see Appendix A3 for details), from which we deduce percentage of PEO molecules rejected by the npPI membrane as shown in Figure 4.4b. While solvated PEO chains with $M_n \leq 1.5$ kg/mol diffused through the npPI by day 3 of the experiment, ~98% of the 35 kg/mol PEO nm was

rejected even after 70 days. Thus, the critical pore diameter in the npPI is estimated to be 5.7 nm, which is the calculated hydrodynamic radius of the 35 kg/mol PEO.[248] This value matches reasonably well with the estimated critical pore size of 4.2 nm estimated from the cylinder diameter including the putative PLA shell, the 55% porosity determined by gravimetry above, and a local hexatic packing of the fibrils (see Figure A3.9 for the geometric calculation). The fact that the PEO chains diffuse through a macroscopic npPI sample confirms its percolating porous structure, which also suggests potential ultrafiltration applications for these materials.

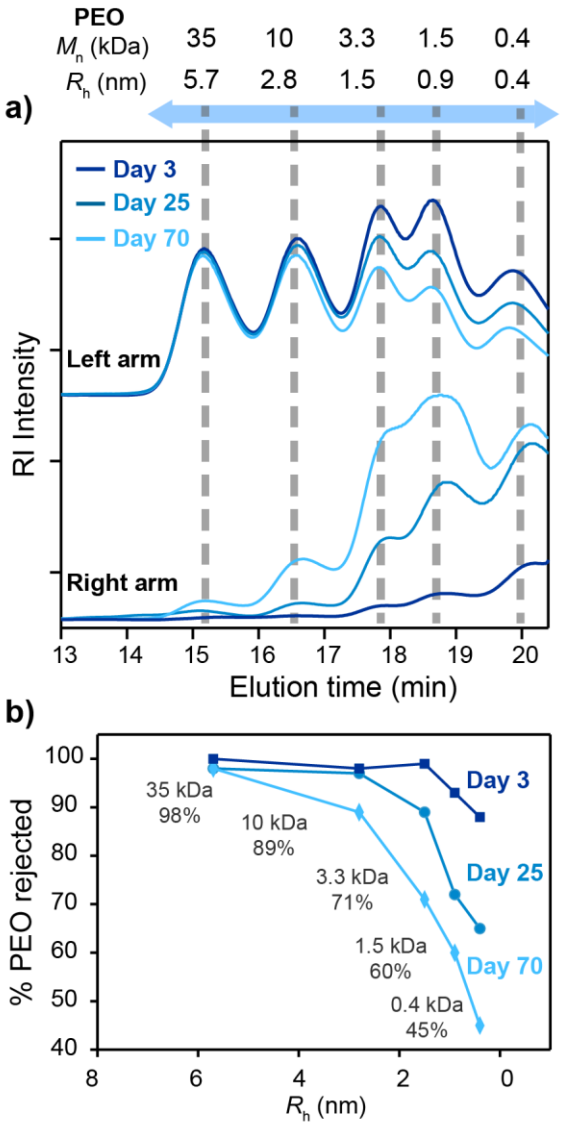

Figure 4. 4. (a) SEC traces showing change of PEO composition over time, from the concentrated PEO stock solution side (left arm, *top*) and the blank solution side (right arm, *bottom*) at pH = 14 separated by the semi-permeable porous IL membrane in a U-tube setup. The vertical dashed line marked the SEC peaks corresponds to each PEO molar mass and its hydrodynamic radius. (b) Percentage of rejected PEO that did not pass through the etched IL separator plotted against the PEO hydrodynamic radius (R_h) after 3, 25 and 70 days of the experiment.

As a step to better understand the limits within which the mechanical properties of these porous fibrillar networks could be tuned, we attempted to fabricate npPI samples from basic etching of PI-*b*-PLA crosslinked by the same thermal annealing protocol with 8.6 wt%, 5.9 wt% and 3.5 wt% DCP. Samples comprising [DCP] ≤ 5.9 wt% were resistant to etching even after 2 d, evidenced by only a 2 wt% mass loss on drying samples exposed to caustic methanol. SEM analyses of such samples (Figure 4.5a) revealed the formation of rough and apparently non-porous structure, which may stem from insufficient crosslinking of the PI to form high modulus fibrils and is in contrast to the porous structure of the etched IL Samples with [DCP] = 8.6 wt% (Figure 4.5b). This line of reasoning is consistent with the notion that preventing porous polymer nanostructure collapse requires the polymer modulus to be sufficient high to counteract the Laplace pressure in the pores.[237, 249] The cross-linked PLA layer coating the elastomeric PI cylinders in a putative core-shell structure might also enable preservation of the structural porosity and the mechanical stability.

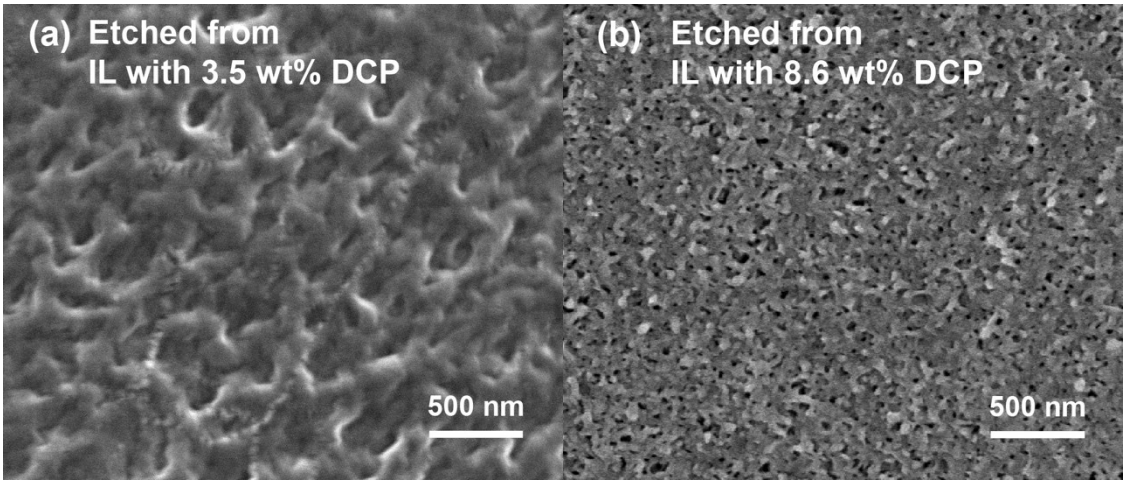

Figure 4. 5. SEM image of (a) IL sample cured with 3.5 wt% DCP, showing the surface after etching in the NaOH solution for 2 days; and (b) cyrofractured IL sample with 8.6 wt% DCP showing the porous cross-section.

While one does not intuitively expect etching the matrix domain from block polymer HEX morphology to produce a bicontinuous, nanoporous material, our findings demonstrate that the minority phase cylinders are indeed connected (Figure 4.6). The common expectation that matrix etching would yield only cylindrical fibrils that fall apart is predicated on a pseudo-single domain sample and neglects the existence of grain boundaries and their detailed structures. Transmission electron microtomography studies by Jinnai *et al.*[250] have documented connections between the cylinders in adjacent, misoriented grains of a HEX-forming poly(styrene-*block*-isoprene) diblock. Even pseudo-single domain samples with HEX morphologies produced by shear alignment often possess Y-junctions (branches) as common defects in imperfectly aligned specimens.[251] Thus, crosslinking the interconnected cylinders in randomly oriented HEX grains lead to a

percolating yet porous, fibrillar network that offers reasonable mechanical properties. This result conceptually resembles a recent report from Osuji and co-workers, where a mechanically stable porous ultrafiltration membrane is prepared through crosslinking shear-aligned, cylindrical surfactant micelles in a continuous aqueous matrix.[252] The mechanical stability of this micellar network stems from a water-soluble crosslinker that links the fibrils to resist structural change. Our findings regarding the intrinsic continuity through grain boundaries suggest new design principles for other mechanically stable porous materials derived from simple and scalable preparation processes.

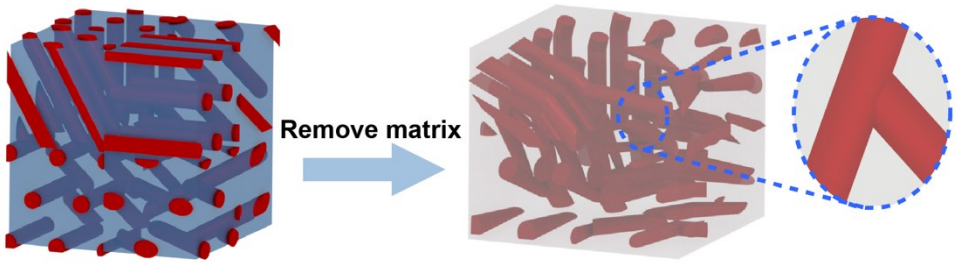

Figure 4. 6. Schematic illustration of the grain boundary connecting two cylinder microdomains after matrix removal.

4.3. Conclusion

In summary, we have demonstrated the preparation of a flexible, nanoporous material by crosslinking of the minority phase of a microphase separated HEX block polymer morphology followed by matrix domain etching. Contrary to the expectation that discontinuous cylindrical microdomains would fall apart upon chemical degradation of the matrix, we obtain a free-standing crosslinked polymer monolith that exhibits mechanical

properties consistent with its nanofibrillar network morphology observed by SEM. We demonstrated the percolating nanoporosity of the resulting materials by studies of the selective penetration of solvated PEO samples of varying molecular weight, which enabled deduction of a critical pore size that conforms to expectations based on the SAXS analyses of the block polymer starting materials. These findings highlight how finite-sized grains in the HEX morphology and the structures of their grain boundaries unexpectedly pave the way toward simple and scalable preparation of nanoporous polymers with potentially tunable surface activities, void sizes and mechanical properties.

Chapter 5. Conclusion

This thesis discussed the impact of segment dispersity and domain grain boundaries on block polymer structure-property relationships. These two factors may have been regarded as architecture and morphological "defects", while we found these polymer imperfections can play a positive and important role in block polymer applications.

The first study in chapter 2 is designated to understand how phase behaviors of poly(styrene-*block*-ethylene oxide-*block*-styrene) (SOS) are affected by a combination of increased dispersity and lithium salt doping in the poly(ethylene oxide) (PEO) domain. We report the synthesis of 17 SOS triblock polymers with broad O block dispersity (bSOS) with broad dispersity O midblocks flanked with narrow dispersity S endblocks. The bSOS triblock polymers are doped with lithium bis(trifluoromethanesulfonyl)imide (LiTFSI) at doping concentration $r = [Li^+]/[O] = 0.01$, 0.05 and 0.09 respectively. Using temperature dependent small angle X-ray scattering (SAXS), the morphology maps are constructed at each salt concentration and compared to narrow dispersity SOS triblock polymers (nSOS). We find that the increased dispersity in O blocks effectively shifts the lamellar morphology window to higher $f_{O/Salt}$ at all three salt concentrations. The shift of phase diagram is attributed to the synergistic chain packing that alters the interface curvature towards the domain with higher dispersity. Dilated lamellar domain spacings are observed with increased O block dispersity while the extent of dilation is higher at lower r, which reflects the depressed swelling effect with increased interaction strength at higher salt loading. While the changes in phase window and domain spacings are more dominant by increased

dispersity, the order-disorder transition of bSOS is mostly govern by salt concentration. The critical segregation strength of microphase separation of salt doped bSOS is found to be with $(\chi N/2)_{ODT}$ = 10.3–10.8 for r = 0.01–0.05, which is in direct contrast with a drastic change in $(\chi N)_{ODT}$ observed in previous studies on broad midblock dispersities. We attribute the result to the competition between enhanced composition fluctuation in these low N polymers that favors the disorder state and preferential solvation of lithium salt that stabilizes the ordered morphologies.

With respect to salt doped block polymers, many research emphasis has been directed to increase its ion conductivity. In Chapter 3, we aim to fundamentally elucidate the decisive factor in conductivity of S/O polymer model systems by comparing the ion conductivity of salt doped bSOS, nSOS and narrow dispersity diblock polymer nSO. Ion conductivities are measured by AC impedance spectroscopy and compared among the three polymer architectures with lamellae morphology. In general, we find that ion conductivity increases with increased block polymer molar mass until it reaches the theoretical limit of about 1/3 of the PEO homopolymer conductivity. While the bSOS and nSOS triblocks show more dramatic conductivity increase with M_n compared to the diblock polymers, thus at intermediate molar mass ($M_n \approx$ 20–50 kg/mol), triblock polymers appear much more conductive than the diblock counterparts. By calculating the lamellar microdomain size from the primary X-ray scattering peak width, we found that the ionic conductivities of block polymers are inversely related to lamellar grain size and the trend is common across the three different polymer architectures. Thus, we argue that a less tortuous conductive

pathway with decreased long-range ordering is an important factor to improve the conductivity in microstructured polymer electrolytes.

Apparently, increasing the density of morphological "defects" leads to increased domain interconnectivity in the lamellar phase, which makes it more desirable for ion transport. Inspired by this result, we infer that in a hexagonally packed cylinder phase, the minority cylinders may also be interconnected through the randomly oriented grain boundaries. In Chapter 4, we report the preparation of nanoporous materials by etching the matrix domain of a cylinder phase. The porous sample is prepared from a directly melt-pressed poly(isoprene-*block*-lactide) diblock polymer, with a cross-linked minority polyisoprene domain and an etched polylactide matrix. The nanoporous microstructure composed of interconnected nanocylinders is revealed from the cryofractured cross-section. The fibril network appears as a free-standing monolith that maintains ~74% of its peak stress after 10 compression-release cycles at 20% maximum strain. When applied as semi-permeable membrane, the etched material demonstrates size-selective penetration to PEO standards of different molar mass which corroborates to its continuous and porous microstructure.

These results indicate the feasibility of a matrix etching strategy to prepare useful nanoporous materials, by taking advantage of the interconnectivity between cylinders through domain boundaries. To take advantage of the wide morphological stability of cylinder phase and the facile matrix etching process, future work should seek for better mechanical properties on the minority cylinder domain, so as to provide mechanical strength for practical applications.

Bibliography

1. Lodge, T. P. Block Copolymers: Past Successes and Future Challenges. *Macromol. Chem. Phys.* **2003,** *204*, 265-273.

2. Leibler, L. Theory of Microphase Separation in Block Copolymers. *Macromolecules* **1980,** *13*, 1602-1617.

3. Bates, F. S.; Fredrickson, G. H. Block Copolymer Thermodynamics: Theory and Experiment. *Annu. Rev. Phys. Chem.* **1990,** *41*, 525-557.

4. Bates, F. S.; Fredrickson, G. H. Block Copolymers–Designer Soft Materials. *Phys. Today* **1999,** *52*, 32-36.

5. Abetz, V.; Simon, P. F. W. Phase Behaviour and Morphologies of Block Copolymers. *Adv. Polym. Sci.* **2005,** *189*, 125-212.

6. Khandpur, A. K.; Förster, S.; Bates, F. S.; Hamley, I. W.; Ryan, A. J.; Bras, W.; Almdal, K.; Mortensen, K. Polyisoprene-Polystyrene Diblock Copolymer Phase Diagram near the Order-Disorder Transition. *Macromolecules* **1995,** *28*, 8796-8806.

7. Matsen, M. W. Effect of Architecture on the Phase Behavior of AB-Type Block Copolymer Melts. *Macromolecules* **2012,** *45*, 2161-2165.

8. Bates, F. S.; Fredrickson, G. H. Conformational Asymmetry and Polymer-Polymer Thermodynamics. *Macromolecules* **1994,** *27*, 1065-1067.

9. Matsen, M. W.; Bates, F. S. Conformationally Asymmetric Block Copolymers. *J. Polym. Sci., Part B: Polym. Phys.* **1997,** *35*, 945-952.

10. Fredrickson, G. H.; Helfand, E. Fluctuation Effects in the Theory of Microphase Separation in Block Copolymers. *J. Chem. Phys.* **1987,** *87*, 697-705.

11. Medapuram, P.; Glaser, J.; Morse, D. C. Universal Phenomenology of Symmetric Diblock Copolymers near the Order–Disorder Transition. *Macromolecules* **2015,** *48*, 819-839.

12. Lynd, N. A.; Meuler, A. J.; Hillmyer, M. A. Polydispersity and Block Copolymer Self-Assembly. *Prog. Polym. Sci.* **2008,** *33*, 875-893.

13. Kim, I.; Li, S. Recent Progress on Polydispersity Effects on Block Copolymer Phase Behavior. *Polym. Rev.* **2019,** *59*, 561-587.

14. Whitfield, R.; Truong, N. P.; Messmer, D.; Parkatzidis, K.; Rolland, M.; Anastasaki, A. Tailoring Polymer Dispersity and Shape of Molecular Weight Distributions: Methods and Applications. *Chem. Sci.* **2019,** *10*, 8724-8734.

15. Matsen, M. W.; Bates, F. S. Origins of Complex Self-Assembly in Block Copolymers. *Macromolecules* **1996,** *29*, 7641-7644.

16. Meuler, A. J.; Hillmyer, M. A.; Bates, F. S. Ordered Network Mesostructures in Block Polymer Materials. *Macromolecules* **2009,** *42*, 7221-7250.

17. Bielawski, C. W.; Morita, T.; Grubbs, R. H. Synthesis of ABA Triblock Copolymers via a Tandem Ring-Opening Metathesis Polymerization: Atom Transfer Radical Polymerization Approach. *Macromolecules* **2000,** *33*, 678-680.

18. Monteiro, M. J. Design Strategies for Controlling the Molecular Weight and Rate Using Reversible Addition–Fragmentation Chain Transfer Mediated Living Radical Polymerization. *J. Polym. Sci., Part A: Polym. Chem.* **2005,** *43*, 3189-3204.

19. Whitfield, R.; Parkatzidis, K.; Rolland, M.; Truong, N. P.; Anastasaki, A. Tuning Dispersity by Photoinduced Atom Transfer Radical Polymerisation: Monomodal Distributions with ppm Copper Concentration. *Angew. Chem. Int. Ed.* **2019,** *58*, 13323-13328.

20. Whitfield, R.; Parkatzidis, K.; Truong, N. P.; Junkers, T.; Anastasaki, A. Tailoring Polymer Dispersity by Raft Polymerization: A Versatile Approach. *Chem* **2020,** *6*, 1340-1352.

21. Arriola, D. J.; Carnahan, E. M.; Hustad, P. D.; Kuhlman, R. L.; Wenzel, T. T. Catalytic Production of Olefin Block Copolymers via Chain Shuttling Polymerization. *Science* **2006,** *312*, 714-719.

22. Yadav, V.; Hashmi, N.; Ding, W.; Li, T. H.; Mahanthappa, M. K.; Conrad, J. C.; Robertson, M. L. Dispersity Control in Atom Transfer Radical Polymerizations through Addition of Phenylhydrazine. *Polym. Chem.* **2018,** *9*, 4332-4342.

23. Kottisch, V.; Gentekos, D. T.; Fors, B. P. "Shaping" the Future of Molecular Weight Distributions in Anionic Polymerization. *ACS Macro Lett.* **2016,** *5*, 796-800.

24. Morsbach, J.; Müller, A. H. E.; Berger-Nicoletti, E.; Frey, H. Living Polymer Chains with Predictable Molecular Weight and Dispersity via Carbanionic Polymerization in Continuous Flow: Mixing Rate as a Key Parameter. *Macromolecules* **2016,** *49*, 5043-5050.

25. Gentekos, D. T.; Dupuis, L. N.; Fors, B. P. Beyond Dispersity: Deterministic Control of Polymer Molecular Weight Distribution. *J. Am. Chem. Soc.* **2016,** *138*, 1848-1851.

26. Bendejacq, D.; Ponsinet, V.; Joanicot, M.; Loo, Y. L.; Register, R. A. Well-Ordered Microdomain Structures in Polydisperse Poly(styrene)−Poly(acrylic acid) Diblock Copolymers from Controlled Radical Polymerization. *Macromolecules* **2002,** *35*, 6645-6649.

27. Lynd, N. A.; Hillmyer, M. A. Influence of Polydispersity on the Self-Assembly of Diblock Copolymers. *Macromolecules* **2005,** *38*, 8803-8810.

28. Lynd, N. A.; Hamilton, B. D.; Hillmyer, M. A. The Role of Polydispersity in the Lamellar Mesophase of Model Diblock Copolymers. *J. Polym. Sci., Part B: Polym. Phys.* **2007,** *45*, 3386-3393.

29. Lynd, N. A.; Hillmyer, M. A. Effects of Polydispersity on the Order-Disorder Transition in Block Copolymer Melts. *Macromolecules* **2007,** *40*, 8050-8055.

30. Widin, J. M.; Schmitt, A. K.; Im, K.; Schmitt, A. L.; Mahanthappa, M. K. Polydispersity-Induced Stabilization of a Disordered Bicontinuous Morphology in ABA Triblock Copolymers. *Macromolecules* **2010,** *43*, 7913-7915.

31. Widin, J. M.; Schmitt, A. K.; Schmitt, A. L.; Im, K.; Mahanthappa, M. K. Unexpected Consequences of Block Polydispersity on the Self-Assembly of ABA Triblock Copolymers. *J. Am. Chem. Soc.* **2012,** *134*, 3834-3844.

32. Schmitt, A. L.; Mahanthappa, M. K. Polydispersity-Driven Shift in the Lamellar Mesophase Composition Window of PEO-PB-PEO Triblock Copolymers. *Soft Matter* **2012,** *8*, 2294-2303.

33. Schmitt, A. K.; Mahanthappa, M. K. Characteristics of Lamellar Mesophases in Strongly Segregated Broad Dispersity ABA Triblock Copolymers. *Macromolecules* **2014,** *47*, 4346-4356.

34. Schmitt, A. K.; Mahanthappa, M. K. Order and Disorder in High χ/Low N, Broad Dispersity ABA Triblock Polymers. *Macromolecules* **2017,** *50*, 6779-6787.

35. Ruzette, A. V.; Tencé-Girault, S.; Leibler, L.; Chauvin, F.; Bertin, D.; Guerret, O.; Gérard, P. Molecular Disorder and Mesoscopic Order in Polydisperse Acrylic Block Copolymers Prepared by Controlled Radical Polymerization. *Macromolecules* **2006,** *39*, 5804-5814.

36. Listak, J.; Jakubowski, W.; Mueller, L.; Plichta, A.; Matyjaszewski, K.; Bockstaller, M. R. Effect of Symmetry of Molecular Weight Distribution in Block Copolymers on Formation of "Metastable" Morphologies. *Macromolecules* **2008,** *41*, 5919-5927.

37. Li, S.; Register, R. A.; Weinhold, J. D.; Landes, B. G. Melt and Solid-State Structures of Polydisperse Polyolefin Multiblock Copolymers. *Macromolecules* **2012,** *45*, 5773-5781.

38. Wagner, N. L.; Timmers, F. J.; Arriola, D. J.; Jueptner, G.; Landes, B. G. Random Block Copolymers via Segment Interchange Olefin Metathesis. *Macromol. Rapid Commun.* **2008,** *29*, 1438-1443.

39. Gentekos, D. T.; Fors, B. P. Molecular Weight Distribution Shape as a Versatile Approach to Tailoring Block Copolymer Phase Behavior. *ACS Macro Lett.* **2018,** *7*, 677-682.

40. Gentekos, D. T.; Jia, J.; Tirado, E. S.; Barteau, K. P.; Smilgies, D. M.; Distasio, R. A.; Fors, B. P. Exploiting Molecular Weight Distribution Shape to Tune Domain Spacing in Block Copolymer Thin Films. *J. Am. Chem. Soc.* **2018,** *140*, 4639-4648.

41. Gentekos, D. T.; Sifri, R. J.; Fors, B. P. Controlling Polymer Properties through the Shape of the Molecular-Weight Distribution. *Nat. Rev. Mater.* **2019,** *4*, 761-774.

42. Sides, S. W.; Fredrickson, G. H. Continuous Polydispersity in a Self-Consistent Field Theory for Diblock Copolymers. *J. Chem. Phys.* **2004,** *121*, 4974-4986.

43. Matsen, M. W. Polydispersity-Induced Macrophase Separation in Diblock Copolymer Melts. *Phys. Rev. Lett.* **2007,** *99*, 148304 (1-4).

44. Matsen, M. W. Comparison of A-Block Polydispersity Effects on BAB Triblock and AB Diblock Copolymer Melts. *Eur. Phys. J. E* **2013,** *36*, 44 (1-7).

45. Cooke, D. M.; Shi, A. C. Effects of Polydispersity on Phase Behavior of Diblock Copolymers. *Macromolecules* **2006,** *39*, 6661-6671.

46. Matsen, M. W. Effect of Large Degrees of Polydispersity on Strongly Segregated Block Copolymers. *Eur. Phys. J. E* **2006,** *21*, 199-207.

47. Lynd, N. A.; Hillmyer, M. A.; Matsen, M. W. Theory of Polydisperse Block Copolymer Melts: Beyond the Schulz-Zimm Distribution. *Macromolecules* **2008,** *41*, 4531-4533.

48. Rosenbloom, S. I.; Gentekos, D. T.; Silberstein, M. N.; Fors, B. P. Tailor-Made Thermoplastic Elastomers: Customisable Materials: via Modulation of Molecular Weight Distributions. *Chem. Sci.* **2020,** *11*, 1361-1367.

49. Xu, H.; Greve, E. M.; Mahanthappa, M. K. Morphological Impact of Segment Dispersity in Lithium Salt-Doped Poly(styrene)/Poly(ethylene oxide) Triblock Polymers. *Macromolecules* **2019,** *52*, 5722-5734.

50. Li, Y.; Qian, H. J.; Lu, Z. Y. The Influence of One Block Polydispersity on Phase Separation of Diblock Copolymers: The Molecular Mechanism for Domain Spacing Expansion. *Polymer* **2013,** *54*, 3716-3722.

51. Beardsley, T. M.; Matsen, M. W. Monte Carlo Phase Diagram for a Polydisperse Diblock Copolymer Melt. *Macromolecules* **2011,** *44*, 6209-6219.

52. Court, F.; Hashimoto, T. Morphological Studies of Binary Mixtures of Block Copolymers. 1. Cosurfactant Effects and Composition Dependence of Morphology. *Macromolecules* **2001,** *34*, 2536-2545.

53. Pitet, L. M.; Hillmyer, M. A. Combining Ring-Opening Metathesis Polymerization and Cyclic Ester Ring-Opening Polymerization to Form ABA Triblock Copolymers from 1,5-Cyclooctadiene and D,L-Lactide. *Macromolecules* **2009,** *42*, 3674-3680.

54. Court, F.; Yamaguchi, D.; Hashimoto, T. Morphological Studies of Binary Mixtures of Block Copolymers: Temperature Dependence of Cosurfactant Effects. *Macromolecules* **2006,** *39*, 2596-2605.

55. Rosedale, J. H.; Bates, F. S.; Almdal, K.; Mortensen, K.; Wignall, G. D. Order and Disorder in Symmetric Diblock Copolymer Melts. *Macromolecules* **1995,** *28*, 1429-1443.

56. Oschmann, B.; Lawrence, J.; Schulze, M. W.; Ren, J. M.; Anastasaki, A.; Luo, Y.; Nothling, M. D.; Pester, C. W.; Delaney, K. T.; Connal, L. A.; McGrath, A. J.; Clark, P. G.; Bates, C. M.; Hawker, C. J. Effects of Tailored Dispersity on the Self-Assembly of

Dimethylsiloxane-Methyl Methacrylate Block Co-Oligomers. *ACS Macro Lett.* **2017,** *6*, 668-673.

57. Matsen, M. W.; Thompson, R. B. Equilibrium Behavior of Symmetric ABA Triblock Copolymer Melts. *J. Chem. Phys.* **1999,** *111*, 7139-7146.

58. Beardsley, T. M.; Matsen, M. W. Effects of Polydispersity on the Order-Disorder Transition of Diblock Copolymer Melts. *Eur. Phys. J. E* **2008,** *27*, 323-333.

59. Pandav, G.; Ganesan, V. Fluctuation Effects on the Order-Disorder Transition in Polydisperse Copolymer Melts. *J. Chem. Phys.* **2013,** *139*, 214905.

60. Fenton, D. E.; Parker, J. M.; Wright, P. V. Complexes of Alkali Metal Ions with Poly(ethylene oxide). *Polymer* **1973,** *14*, 589-589.

61. Tarascon, J. M.; Armand, M. Issues and Challenges Facing Rechargeable Lithium Batteries. *Nature* **2001,** *414*, 359-367.

62. Mauger, A.; Armand, M.; Julien, C. M.; Zaghib, K. Challenges and Issues Facing Lithium Metal for Solid-State Rechargeable Batteries. *J. Power Sources* **2017,** *353*, 333-342.

63. Lin, D.; Liu, Y.; Cui, Y. Reviving the Lithium Metal Anode for High-Energy Batteries. *Nat. Nanotechnol.* **2017,** *12*, 194-206.

64. Tu, Z.; Nath, P.; Lu, Y.; Tikekar, M. D.; Archer, L. A. Nanostructured Electrolytes for Stable Lithium Electrodeposition in Secondary Batteries. *Acc. Chem. Res.* **2015,** *48*, 2947-2956.

65. Tikekar, M. D.; Choudhury, S.; Tu, Z.; Archer, L. A. Design Principles for Electrolytes and Interfaces for Stable Lithium-Metal Batteries. *Nat. Energy* **2016,** *1*, 16114-16114.

66. Monroe, C.; Newman, J. The Impact of Elastic Deformationon Deposition Kinetics at Lithium/Polymer Interfaces. *J. Electrochem. Soc.* **2005,** *152*, A396-A404.

67. Barai, P.; Higa, K.; Srinivasan, V. Lithium Dendrite Growth Mechanisms in Polymer Electrolytes and Prevention Strategies. *Phys. Chem. Chem. Phys.* **2017,** *19*, 20493-20505.

68. Maslyn, J. A.; Loo, W. S.; McEntush, K. D.; Oh, H. J.; Harry, K. J.; Parkinson, D. Y.; Balsara, N. P. Growth of Lithium Dendrites and Globules through a Solid Block Copolymer Electrolyte as a Function of Current Density. *J. Phys. Chem. C* **2018,** *122*, 22-22.

69. Schauser, N. S.; Harry, K. J.; Parkinson, D. Y.; Watanabe, H.; Balsara, N. P. Lithium Dendrite Growth in Glassy and Rubbery Nanostructured Block Copolymer Electrolytes. *J. Electrochem. Soc.* **2015,** *162*, A398-A405.

70. Khurana, R.; Schaefer, J. L.; Archer, L. A.; Coates, G. W. Suppression of Lithium Dendrite Growth Using Cross-Linked Polyethylene/Poly(ethylene oxide) Electrolytes: A New Approach for Practical Lithium-Metal Polymer Batteries. *J. Am. Chem. Soc.* **2014,** *136*, 7395-7402.

71. Stalin, S.; Johnson, H. E. N.; Biswal, P.; Vu, D.; Zhao, Q.; Yin, J.; Abel, B. A.; Deng, Y.; Coates, G. W.; Archer, L. A. Achieving Uniform Lithium Electrodeposition in

Cross-Linked Poly(ethylene oxide) Networks: “Soft” Polymers Prevent Metal Dendrite Proliferation. *Macromolecules* **2020,** *53*, 5445-5454.

72. Lascaud, S.; Perrier, M.; Vallee, A.; Besner, S.; Prudhomme, J.; Armand, M. Phase Diagrams and Conductivity Behavior of Poly(ethylene oxide)-Molten Salt Rubbery Electrolytes. *Macromolecules* **1994,** *27*, 7469-7477.

73. Borodin, O.; Smith, G. D. Mechanism of Ion Transport in Amorphous Poly(ethylene oxide)/LiTFSI from Molecular Dynamics Simulations. *Macromolecules* **2006,** *39*, 1620-1629.

74. Duan, Y.; Halley, J. W.; Curtiss, L.; Redfern, P. Mechanisms of Lithium Transport in Amorphous Polyethylene Oxide. *J. Chem. Phys.* **2005,** *122*, 054702.

75. Hallinan, D. T.; Balsara, N. P. Polymer Electrolytes. *Annu. Rev. Mater. Res* **2013,** *43*, 503-525.

76. Chintapalli, M.; Le, T. N. P.; Venkatesan, N. R.; Mackay, N. G.; Rojas, A. A.; Thelen, J. L.; Chen, X. C.; Devaux, D.; Balsara, N. P. Structure and Ionic Conductivity of Polystyrene-*block*-Poly(ethylene oxide) Electrolytes in the High Salt Concentration Limit. *Macromolecules* **2016,** *49*, 1770-1780.

77. Schulze, M. W.; McIntosh, L. D.; Hillmyer, M. A.; Lodge, T. P. High-Modulus, High-Conductivity Nanostructured Polymer Electrolyte Membranes via Polymerization-Induced Phase Separation. *Nano Lett.* **2014,** *14*, 122-126.

78. Park, M. J. Confinement-Entitled Morphology and Ion Transport in Ion-Containing Polymers. *Mol. Syst. Des. Eng.* **2019,** *4*, 239-251.

79. Hallinan, D. T.; Villaluenga, I.; Balsara, N. P. Polymer and Composite Electrolytes. *MRS Bull.* **2018,** *43*, 775-781.

80. Morris, M. A.; An, H.; Lutkenhaus, J. L.; Epps, T. H. Harnessing the Power of Plastics: Nanostructured Polymer Systems in Lithium-Ion Batteries. *ACS Energy Lett.* **2017,** *2*, 1919-1936.

81. Singh, M.; Odusanya, O.; Wilmes, G. M.; Eitouni, H. B.; Gomez, E. D.; Patel, A. J.; Chen, V. L.; Park, M. J.; Fragouli, P.; Iatrou, H.; Hadjichristidis, N.; Cookson, D.; Balsara, N. P. Effect of Molecular Weight on the Mechanical and Electrical Properties of Block Copolymer Electrolytes. *Macromolecules* **2007,** *40*, 4578-4585.

82. Panday, A.; Mullin, S.; Gomez, E. D.; Wanakule, N.; Chen, V. L.; Hexemer, A.; Pople, J.; Balsara, N. P. Effect of Molecular Weight and Salt Concentration on Conductivity of Block Copolymer Electrolytes. *Macromolecules* **2009,** *42*, 4632-4637.

83. Zardalidis, G.; Gatsouli, K.; Pispas, S.; Mezger, M.; Floudas, G. Ionic Conductivity, Self-Assembly, and Viscoelasticity in Poly(styrene-*b*-ethylene oxide) Electrolytes Doped with LiTF. *Macromolecules* **2015,** *48*, 7164-7171.

84. Young, W. S.; Epps, T. H. Salt Doping in PEO-Containing Block Copolymers: Counterion and Concentration Effects. *Macromolecules* **2009,** *42*, 2672-2678.

85. Ye, Y. S.; Rick, J.; Hwang, B. J. Ionic Liquid Polymer Electrolytes. *J. Mater. Chem. A* **2013,** *1*, 2719-2743.

86. Cheng, X.; Pan, J.; Zhao, Y.; Liao, M.; Peng, H. Gel Polymer Electrolytes for Electrochemical Energy Storage. *Adv. Energy Mater* **2018,** *8*, 1702184.

87. Barteau, K. P.; Wolffs, M.; Lynd, N. A.; Fredrickson, G. H.; Kramer, E. J.; Hawker, C. J. Allyl Glycidyl Ether-Based Polymer Electrolytes for Room Temperature Lithium Batteries. *Macromolecules* **2013,** *46*, 8988-8994.

88. Shibuya, Y.; Tatara, R.; Jiang, Y.; Shao-Horn, Y.; Johnson, J. A. Brush-First Romp of Poly(ethylene oxide) Macromonomers of Varied Length: Impact of Polymer Architecture on Thermal Behavior and Li^+ Conductivity. *J. Polym. Sci., Part A: Polym. Chem.* **2019,** *57*, 448-455.

89. Porcarelli, L.; Gerbaldi, C.; Bella, F.; Nair, J. R. Super Soft All-Ethylene Oxide Polymer Electrolyte for Safe All-Solid Lithium Batteries. *Sci. Rep.* **2016,** *6*, 19892.

90. Chopade, S. A.; Au, J. G.; Li, Z.; Schmidt, P. W.; Hillmyer, M. A.; Lodge, T. P. Robust Polymer Electrolyte Membranes with High Ambient-Temperature Lithium-Ion Conductivity via Polymerization-Induced Microphase Separation. *ACS Appl. Mater. Interfaces* **2017,** *9*, 14561-14565.

91. Yuan, R.; Teran, A. A.; Gurevitch, I.; Mullin, S. A.; Wanakule, N. S.; Balsara, N. P. Ionic Conductivity of Low Molecular Weight Block Copolymer Electrolytes. *Macromolecules* **2013,** *46*, 914-921.

92. Nakamura, I.; Balsara, N. P.; Wang, Z. G. Thermodynamics of Ion-Containing Polymer Blends and Block Copolymers. *Phys. Rev. Lett.* **2011,** *107*, 1-5.

93. Nakamura, I.; Wang, Z. G. Salt-Doped Block Copolymers: Ion Distribution, Domain Spacing and Effective χ Parameter. *Soft Matter* **2012,** *8*, 9356-9367.

94. Gomez, E. D.; Panday, A.; Feng, E. H.; Chen, V.; Stone, G. M.; Minor, A. M.; Kisielowski, C.; Downing, K. H.; Borodin, O.; Smith, G. D.; Balsara, N. P. Effect of Ion

Distribution on Conductivity of Block Copolymer Electrolytes. *Nano Lett.* **2009,** *9*, 1212-1216.

95. Hou, K. J.; Loo, W. S.; Balsara, N. P.; Qin, J. Comparing Experimental Phase Behavior of Ion-Doped Block Copolymers with Theoretical Predictions Based on Selective Ion Solvation. *Macromolecules* **2020,** *53*, 3956-3966.

96. Teran, A. A.; Balsara, N. P. Thermodynamics of Block Copolymers with and without Salt. *J. Phys. Chem. B* **2014,** *118*, 4-17.

97. Loo, W. S.; Sethi, G. K.; Teran, A. A.; Galluzzo, M. D.; Maslyn, J. A.; Oh, H. J.; Mongcopa, K. I.; Balsara, N. P. Composition Dependence of the Flory-Huggins Interaction Parameters of Block Copolymer Electrolytes and the Isotaksis Point. *Macromolecules* **2019,** *52*, 5590-5601.

98. Hiemenz, P. C.; Lodge, T. P., *Polymer Chemistry*. 2nd ed.; CRC Press: Boca Raton, FL: 2007.

99. Maurer, W. W.; Bates, F. S.; Lodge, T. P.; Almdal, K.; Mortensen, K.; Fredrickson, G. H. Can a Single Function for χ Account for Block Copolymer and Homopolymer Blend Phase Behavior? *J. Chem. Phys.* **1998,** *108*, 2989-3000.

100. Lin, C. C.; Jonnalagadda, S. V.; Kesani, P. K.; Dai, H. J.; Balsara, N. P. Effect of Molecular Structure on Thermodynamics of Block Copolymer Melts. *Macromolecules* **1994,** *27*, 7769-7780.

101. Loo, W. S.; Mongcopa, K. I.; Gribble, D. A.; Faraone, A. A.; Balsara, N. P. Investigating the Effect of Added Salt on the Chain Dimensions of Poly(ethylene oxide) through Small-Angle Neutron Scattering. *Macromolecules* **2019,** *52*, 8724-8732.

102. Loo, W. S.; Balsara, N. P. Organizing Thermodynamic Data Obtained from Multicomponent Polymer Electrolytes: Salt-Containing Polymer Blends and Block Copolymers. *J. Polym. Sci., Part B: Polym. Phys.* **2019,** *57*, 1177-1187.

103. Sax, J.; Ottino, J. M. Modeling of Transport of Small Molecules in Polymer Blends: Application of Effective Medium Theory. *Polym. Eng. Sci.* **1983,** *23*, 165-176.

104. Shen, K. H.; Brown, J. R.; Hall, L. M. Diffusion in Lamellae, Cylinders, and Double Gyroid Block Copolymer Nanostructures. *ACS Macro Lett.* **2018,** *7*, 1092-1098.

105. Chen, L.; Phillip, W. A.; Cussler, E. L.; Hillmyer, M. A. Robust Nanoporous Membranes Templated by a Doubly Reactive Block Copolymer. *J. Am. Chem. Soc.* **2007,** *129*, 13786-13787.

106. Xie, S.; Meyer, D. J.; Wang, E.; Bates, F. S.; Lodge, T. P. Structure and Properties of Bicontinuous Microemulsions from Salt-Doped Ternary Polymer Blends. *Macromolecules* **2019,** *52*, 9693-9702.

107. Lee, D.; Jung, H. Y.; Park, M. J. Solid-State Polymer Electrolytes Based on AB_3-Type Miktoarm Star Copolymers. *ACS Macro Lett.* **2018,** *7*, 1046-1050.

108. Devaux, D.; Glé, D.; Phan, T. N. T.; Gigmes, D.; Giroud, E.; Deschamps, M.; Denoyel, R.; Bouchet, R. Optimization of Block Copolymer Electrolytes for Lithium Metal Batteries. *Chem. Mater.* **2015,** *27*, 4682-4692.

109. Kuan, W. F.; Remy, R.; Mackay, M. E.; Epps, T. H. Controlled Ionic Conductivity via Tapered Block Polymer Electrolytes. *RSC Adv.* **2015,** *5*, 12597-12604.

110. Jo, G.; Ahn, H.; Park, M. J. Simple Route for Tuning the Morphology and Conductivity of Polymer Electrolytes: One End Functional Group Is Enough. *ACS Macro Lett.* **2013,** *2*, 990-995.

111. Park, M. J.; Jo, G.; Kwak, K.; Jung, H. Y.; Kim, M.; Kim, O.; Mandal, P. Modulating Ion Transport and Self-Assembly of Polymer Electrolytes via End-Group Chemistry. *Macromolecules* **2017,** *50*, 3224-3233.

112. Bouchet, R.; Phan, T. N. T.; Beaudoin, E.; Devaux, D.; Davidson, P.; Bertin, D.; Denoyel, R. Charge Transport in Nanostructured PS−PEO−PS Triblock Copolymer Electrolytes. *Macromolecules* **2014,** *47*, 2659-2665.

113. Schneider, H.; Saalwächter, K.; Roos, M. Complex Morphology of the Intermediate Phase in Block Copolymers and Semicrystalline Polymers As Revealed by ^{1}H NMR Spin Diffusion Experiments. *Macromolecules* **2017,** *50*, 8598-8610.

114. Sethuraman, V.; Mogurampelly, S.; Ganesan, V. Ion Transport Mechanisms in Lamellar Phases of Salt-Doped PS–PEO Block Copolymer Electrolytes. *Soft Matter* **2017,** *13*, 7793-7803.

115. Mongcopa, K. I. S.; Tyagi, M.; Mailoa, J. P.; Samsonidze, G.; Kozinsky, B.; Mullin, S. A.; Gribble, D. A.; Watanabe, H.; Balsara, N. P. Relationship between Segmental Dynamics Measured by Quasi-Elastic Neutron Scattering and Conductivity in Polymer Electrolytes. *ACS Macro Lett.* **2018,** *7*, 504-508.

116. Wheatle, B. K.; Lynd, N. A.; Ganesan, V. Effect of Polymer Polarity on Ion Transport: A Competition between Ion Aggregation and Polymer Segmental Dynamics. *ACS Macro Lett.* **2018,** *7*, 1149-1154.

117. Chintapalli, M.; Chen, X. C.; Thelen, J. L.; Teran, A. A.; Wang, X.; Garetz, B. A.; Balsara, N. P. Effect of Grain Size on the Ionic Conductivity of a Block Copolymer Electrolyte. *Macromolecules* **2014,** *47*, 5424-5431.

118. Gido, S. P.; Gunther, J.; Thomas, E. L.; Hoffman, D. Lamellar Diblock Copolymer Grain Boundary Morphology. 1. Twist Boundary Characterization. *Macromolecules* **1993,** *26*, 4506-4520.

119. Gido, S. P.; Thomas, E. L. Lamellar Diblock Copolymer Grain Boundary Morphology. 4. Tilt Boundaries. *Macromolecules* **1994,** *27*, 6137-6144.

120. Nishikawa, Y.; Kawada, H.; Hasegawa, H.; Hashimoto, T. Grain Boundary Morphology of Lamellar Microdomains. *Acta Polym.* **1993,** *44*, 247-255.

121. Liu, G.; Ramírez-Hernández, A.; Yoshida, H.; Nygård, K.; Satapathy, D. K.; Bunk, O.; de Pablo, J. J.; Nealey, P. F. Morphology of Lamellae-Forming Block Copolymer Films between Two Orthogonal Chemically Nanopatterned Striped Surfaces. *Phys. Rev. Lett.* **2012,** *108*, 065502.

122. Olson, D. A.; Chen, L.; Hillmyer, M. A. Templating Nanoporous Polymers with Ordered Block Copolymers. *Chem. Mater.* **2008,** *20*, 869-890.

123. Jackson, E. A.; Hillmyer, M. A. Nanoporous Membranes Derived from Block Copolymers: From Drug Delivery to Water Filtration. *ACS Nano* **2010,** *4*, 3548-3553.

124. Lee, J. S.; Hirao, A.; Nakahama, S. Polymerization of Monomers Containing Functional Silyl Groups. 5. Synthesis of New Porous Membranes with Functional Groups. *Macromolecules* **1988,** *21*, 274-276.

125. Hillmyer, M. A., Nanoporous Materials from Block Copolymer Precursors in *Block Copolymers II*, Springer-Verlag: Berlin, 2005; pp 137-181.

126. Hashimoto, T.; Tsutsumi, K.; Funaki, Y. Nanoprocessing Based on Bicontinuous Microdomains of Block Copolymers: Nanochannels Coated with Metals. *Langmuir* **1997,** *13*, 6869-6872.

127. Ndoni, S.; Vigild, M. E.; Berg, R. H. Nanoporous Materials with Spherical and Gyroid Cavities Created by Quantitative Etching of Polydimethylsiloxane in Polystyrene-Polydimethylsiloxane Block Copolymers. *J. Am. Chem. Soc.* **2003,** *125*, 13366-13367.

128. Mao, H.; Hillmyer, M. A. Macroscopic Samples of Polystyrene with Ordered Three-Dimensional Nanochannels. *Soft Matter* **2006,** *2*, 57-59.

129. Zhou, N.; Bates, F. S.; Lodge, T. P. Mesoporous Membrane Templated by a Polymeric Bicontinuous Microemulsion. *Nano Lett.* **2006,** *6*, 2354-2357.

130. Seo, M.; Hillmyer, M. A. Reticulated Nanoporous Polymers by Controlled Polymerization-Induced Microphase Separation. *Science* **2012,** *336*, 1422-1425.

131. Kanamori, K.; Nakanishi, K.; Hanada, T. Rigid Macroporous Poly(divinylbenzene) Monoliths with a Well-Defined Bicontinuous Morphology Prepared by Living Radical Polymerization. *Adv. Mater.* **2006,** *18*, 2407-2411.

132. Vidil, T.; Hampu, N.; Hillmyer, M. A. Nanoporous Thermosets with Percolating Pores from Block Polymers Chemically Fixed above the Order-Disorder Transition. *ACS Cent. Sci.* **2017,** *3*, 1114-1120.

133. Zeng, D.; Ribbe, A.; Hayward, R. C. Anisotropic and Interconnected Nanoporous Materials from Randomly End-Linked Copolymer Networks. *Macromolecules* **2017,** *50*, 4668-4676.

134. Yan, X.; Liu, G.; Liu, F.; Tang, B. Z.; Peng, H.; Pakhomov, A. B.; Wong, C. Y. Superparamagnetic Triblock Copolymer/Fe_2O_3 Hybrid Nanofibers. *Angew. Chem. Int. Ed.* **2001,** *40*, 3593-3596.

135. Liu, G.; Yan, X.; Duncan, S. Polystyrene-Block-Polyisoprene Nanofiber Fractions. 1. Preparation and Static Light-Scattering Study. *Macromolecules* **2002,** *35*, 9788-9793.

136. Won, Y. Y.; Ted Davis, H.; Bates, F. S. Giant Wormlike Rubber Micelles. *Science* **1999,** *283*, 960-963.

137. Liu, G., Block Copolymer Nanotubes Derived from Self-Assembly in *Self-Assembled Nanomaterials II*, Springer: Berlin Heidelberg, 2008; pp 29-64.

138. Majewski, P. W.; Gopinadhan, M.; Jang, W. S.; Lutkenhaus, J. L.; Osuji, C. O. Anisotropic Ionic Conductivity in Block Copolymer Membranes by Magnetic Field Alignment. *J. Am. Chem. Soc.* **2010,** *132*, 17516-17522.

139. Majewski, P. W.; Gopinadhan, M.; Osuji, C. O. The Effects of Magnetic Field Alignment on Lithium Ion Transport in a Polymer Electrolyte Membrane with Lamellar Morphology. *Polymers* **2019,** *11*, 887-887.

140. Majewski, P. W.; Gopinadhan, M.; Osuji, C. O. Understanding Anisotropic Transport in Self-Assembled Membranes and Maximizing Ionic Conductivity by Microstructure Alignment. *Soft Matter* **2013,** *9*, 7106-7116.

141. Park, M. J.; Balsara, N. P. Anisotropie Proton Conduction in Aligned Block Copolymer Electrolyte Membranes at Equilibrium with Humid Air. *Macromolecules* **2010,** *43*, 292-298.

142. Querelle, S. E.; Jackson, E. A.; Cussler, E. L.; Hillmyer, M. A. Ultrafiltration Membranes with a Thin Poly(styrene)-*b*-Poly(isoprene) Selective Layer. *ACS Appl. Mater. Interfaces* **2013,** *5*, 5044-5050.

143. Yang, S. Y.; Ryu, I.; Kim, H. Y.; Kim, J. K.; Jang, S. K.; Russell, T. P. Nanoporous Membranes with Ultrahigh Selectivity and Flux for the Filtration of Viruses. *Adv. Mater.* **2006,** *18*, 709-712.

144. Phillip, W. A.; O'neill, B.; Rodwogin, M.; Hillmyer, M. A.; Cussler, E. L. Self-Assembled Block Copolymer Thin Films as Water Filtration Membranes. *ACS Appl. Mater. Interfaces* **2010,** *2*, 847-853.

145. Kambe, Y.; Arges, C. G.; Czaplewski, D. A.; Dolejsi, M.; Krishnan, S.; Stoykovich, M. P.; de Pablo, J. J.; Nealey, P. F. Role of Defects in Ion Transport in Block Copolymer Electrolytes. *Nano Lett.* **2019,** *19*, 4684–4691.

146. Arges, C. G.; Kambe, Y.; Dolejsi, M.; Wu, G. P.; Segal-Pertz, T.; Ren, J.; Cao, C.; Craig, G. S. W.; Nealey, P. F. Interconnected Ionic Domains Enhance Conductivity in Microphase Separated Block Copolymer Electrolytes. *J. Mater. Chem. A* **2017,** *5*, 5619-5629.

147. Weber, R. L.; Ye, Y.; Schmitt, A. L.; Banik, S. M.; Elabd, Y. A.; Mahanthappa, M. K. Effect of Nanoscale Morphology on the Conductivity of Polymerized Ionic Liquid Block Copolymers. *Macromolecules* **2011,** *44*, 5727-5735.

148. Diederichsen, K. M.; Brow, R. R.; Stoykovich, M. P. Percolating Transport and the Conductive Scaling Relationship in Lamellar Block Copolymers under Confinement. *ACS Nano* **2015,** *9*, 2465-2476.

149. Chintapalli, M.; Higa, K.; Chen, X. C.; Srinivasan, V.; Balsara, N. P. Simulation of Local Ion Transport in Lamellar Block Copolymer Electrolytes Based on Electron Micrographs. *J. Polym. Sci., Part B: Polym. Phys.* **2017,** *55*, 266-274.

150. Werber, J. R.; Osuji, C. O.; Elimelech, M. Materials for Next-Generation Desalination and Water Purification Membranes. *Nat. Rev. Mater.* **2016,** *1*, 16018.

151. Abetz, V. Isoporous Block Copolymer Membranes. *Macromol. Rapid Commun.* **2015,** *36*, 10-22.

152. Crossland, E. J. W.; Kamperman, M.; Nedelcu, M.; Ducati, C.; Wiesner, U.; Smilgies, D. M.; Toombes, G. E. S.; Hillmyer, M. A.; Ludwigs, S.; Steiner, U.; Snaith, H. J. A Bicontinuous Double Gyroid Hybrid Solar Cell. *Nano Lett.* **2009,** *9*, 2807-2812.

153. Orilall, M. C.; Wiesner, U. Block Copolymer Based Composition and Morphology Control in Nanostructured Hybrid Materials for Energy Conversion and Storage: Solar Cells, Batteries, and Fuel Cells. *Chem. Soc. Rev.* **2011,** *40*, 520-535.

154. Yoo, H. G.; Byun, M.; Jeong, C. K.; Lee, K. J. Performance Enhancement of Electronic and Energy Devices via Block Copolymer Self-Assembly. *Adv. Mater.* **2015,** *27*, 3982-3998.

155. Cheng, J. Y.; Ross, C. A.; Smith, H. I.; Thomas, E. L. Templated Self-Assembly of Block Copolymers: Top-Down Helps Bottom-Up. *Adv. Mater.* **2006,** *18*, 2505-2521.

156. Bang, J.; Jeong, U.; Ryu, D. Y.; Russell, T. P.; Hawker, C. J. Block Copolymer Nanolithography: Translation of Molecular Level Control to Nanoscale Patterns. *Adv. Mater.* **2009,** *21*, 4769-4792.

157. Bates, C. M.; Maher, M. J.; Janes, D. W.; Ellison, C. J.; Willson, C. G. Block Copolymer Lithography. *Macromolecules* **2014,** *47*, 2-12.

158. Bates, F. S.; Hillmyer, M. A.; Lodge, T. P.; Bates, C. M.; Delaney, K. T.; Fredrickson, G. H. Multiblock Polymers: Panacea or Pandora's Box? *Science* **2012,** *336*, 434-440.

159. Mai, S. M.; Mingvanish, W.; Turner, S. C.; Chaibundit, C.; Fairclough, J. P. A.; Heatley, F.; Matsen, M. W.; Ryan, A. J.; Booth, C. Microphase-Separation Behavior of Triblock Copolymer Melts. Comparison with Diblock Copolymer Melts. *Macromolecules* **2000,** *33*, 5124-5130.

160. Cochran, E. W.; Garcia-Cervera, C. J.; Fredrickson, G. H. Stability of the Gyroid Phase in Diblock Copolymers at Strong Segregation. *Macromolecules* **2006,** *39*, 2449-2451.

161. Arora, A.; Qin, J.; Morse, D. C.; Delaney, K. T.; Fredrickson, G. H.; Bates, F. S.; Dorfman, K. D. Broadly Accessible Self-Consistent Field Theory for Block Polymer Materials Discovery. *Macromolecules* **2016,** *49*, 4675-4690.

162. Plichta, A.; Zhong, M.; Li, W.; Elsen, A. M.; Matyjaszewski, K. Tuning Dispersity in Diblock Copolymers Using ARGET ATRP. *Macromol. Chem. Phys.* **2012,** *213*, 2659-2668.

163. Ouchi, M.; Terashima, T.; Sawamoto, M. Transition Metal-Catalyzed Living Radical Polymerization: Toward Perfection in Catalysis and Precision Polymer Synthesis. *Chem. Rev.* **2009,** *109*, 4963-5050.

164. Register, R. A. Continuity through Dispersity. *Nature* **2012,** *483*, 167-168.

165. Bates, C. M.; Bates, F. S. 50th Anniversary Perspective: Block Polymers-Pure Potential. *Macromolecules* **2017,** *50*, 3-22.

166. Hillmyer, M. A. Polydisperse Block Copolymers: Don't Throw Them Away. *J. Polym. Sci., Part B: Polym. Phys.* **2007,** *45*, 3249-3251.

167. Loo, W. S.; Galluzzo, M. D.; Li, X.; Maslyn, J. A.; Oh, H. J.; Mongcopa, K. I.; Zhu, C.; Wang, A. A.; Wang, X.; Garetz, B. A.; Balsara, N. P. Phase Behavior of Mixtures of Block Copolymers and a Lithium Salt. *J. Phys. Chem. B* **2018,** *122*, 8065-8074.

168. Armarego, W. L. F.; Chai, C. L. L., *Purification of Laboratory Chemicals*. Butterworth-Heinemann: Waltham, MA, 2009.

169. Hayakawa, Y.; Kato, H.; Uchiyama, M.; Kajino, H.; Noyori, R. Allyloxycarbonyl Group: A Versatile Blocking Group for Nucleotide Synthesis. *J. Org. Chem.* **1985,** *51*, 2400-2402.

170. Lipscomb, C. E.; Mahanthappa, M. K. Microphase Separation Mode-Dependent Mechanical Response in Poly(vinyl ester)/PEO Triblock Copolymers. *Macromolecules* **2011,** *44*, 4401-4409.

171. Park, J. H.; Jeon, J. Y.; Lee, J. J.; Jang, Y.; Varghese, J. K.; Lee, B. Y. Preparation of High-Molecular-Weight Aliphatic Polycarbonates by Condensation Polymerization of Diols and Dimethyl Carbonate. *Macromolecules* **2013,** *46*, 3301-3308.

172. Mark, J. E., Physical Properties of Polymers Handbook. in 2 nd ed.; Mark, J. E., Ed. Springer: Philadelphia, PA, 2007.

173. Bates, F. S. Measurement of the Correlation Hole in Homogeneous Block Copolymer Melts. *Macromolecules* **1985,** *18*, 525-528.

174. Lee, I.; Panthani, T. R.; Bates, F. S. Sustainable Poly(lactide-*b*-butadiene) Multiblock Copolymers with Enhanced Mechanical Properties. *Macromolecules* **2013,** *46*, 7387-7398.

175. Likhtman, A. E.; Semenov, A. N. An Advance in the Theory of Strongly Segregated Polymers. *Europhys. Lett.* **2000,** *51*, 307-313.

176. Matsen, M. W.; Bates, F. S. Block Copolymer Microstructures in the Intermediate-Segregation Regime. *J. Chem. Phys.* **1997,** *106*, 2436-2448.

177. Thelen, J. L.; Teran, A. A.; Wang, X.; Garetz, B. A.; Nakamura, I.; Wang, Z. G.; Balsara, N. P. Phase Behavior of a Block Copolymer/Salt Mixture through the Order-to-Disorder Transition. *Macromolecules* **2014,** *47*, 2666-2673.

178. Nakamura, I.; Balsara, N. P.; Wang, Z. G. First-Order Disordered-to-Lamellar Phase Transition in Lithium Salt-Doped Block Copolymers. *ACS Macro Lett.* **2013,** *2*, 478-481.

179. Teran, A. A.; Mullin, S. A.; Hallinan, D. T.; Balsara, N. P. Discontinuous Changes in Ionic Conductivity of a Block Copolymer Electrolyte through an Order-Disorder Transition. *ACS Macro Lett.* **2012,** *1*, 305-309.

180. Wang, Z. G. Effects of Ion Solvation on the Miscibility of Binary Polymer Blends. *J. Phys. Chem. B* **2008,** *112*, 16205-16213.

181. Mao, G.; Saboungi, M. L.; Price, D. L.; Armand, M. B.; Howells, W. S. Structure of Liquid PEP-LiTFSI Electrolyte. *Phys. Rev. Lett.* **2000,** *84*, 5536-5539.

182. Borodin, O.; Smith, G. D. Molecular Dynamics Simulations of Poly(ethylene oxide)/LiI Melts. 1. Structural and Conformational Properties. *Macromolecules* **1998,** *31*, 8396-8406.

183. Ren, C. L.; Nakamura, I.; Wang, Z. G. Effects of Ion-Induced Cross-Linking on the Phase Behavior in Salt-Doped Polymer Blends. *Macromolecules* **2016,** *49*, 425-431.

184. Xie, S.; Lodge, T. P. Phase Behavior of Binary Polymer Blends Doped with Salt. *Macromolecules* **2018,** *51*, 266-274.

185. Young, W. S.; Kuan, W. F.; Epps, T. H. Block Copolymer Electrolytes for Rechargeable Lithium Batteries. *J. Polym. Sci., Part B: Polym. Phys.* **2014,** *52*, 1-16.

186. Young, W. S.; Epps, T. H. Ionic Conductivities of Block Copolymer Electrolytes with Various Conducting Pathways: Sample Preparation and Processing Considerations. *Macromolecules* **2012,** *45*, 4689-4697.

187. Hirahara, K.; Takano, A.; Yamamoto, M.; Kazama, T.; Isono, Y.; Fujimoto, T.; Watanabe, O. Fabrication of Solid Polymer Electrolyte Based on Block-Graft Copolymer. 1. Precision Synthesis and Characterization of Polystyrene-*block*-[Poly(p-hydroxystyrene)-*graft*-Poly(ethylene oxide)]-*block*-Polystyrene. *React. Funct. Polym.* **1998,** *37*, 169-182

188. Zhang, B.; Zhang, Y.; Zhang, N.; Liu, J.; Cong, L.; Liu, J.; Sun, L.; Mauger, A.; Julien, C. M.; Xie, H.; Pan, X. Synthesis and Interface Stability of Polystyrene-

Poly(ethylene glycol)-Polystyrene Triblock Copolymer as Solid-State Electrolyte for Lithium-Metal Batteries. *J. Power Sources* **2019,** *428*, 93-104.

189. Bates, C. M.; Chang, A. B.; Momčilović, N.; Jones, S. C.; Grubbs, R. H. ABA Triblock Brush Polymers: Synthesis, Self-Assembly, Conductivity, and Rheological Properties. *Macromolecules* **2015,** *48*, 4967-4973.

190. Zardalidis, G.; Pipertzis, A.; Mountrichas, G.; Pispas, S.; Mezger, M.; Floudas, G. Effect of Polymer Architecture on the Ionic Conductivity. Densely Grafted Poly(ethylene oxide) Brushes Doped with LiTF. *Macromolecules* **2016,** *49*, 2679-2687.

191. Chen, Y.; Shi, Y.; Liang, Y.; Dong, H.; Hao, F.; Wang, A.; Zhu, Y.; Cui, X.; Yao, Y. Hyperbranched PEO-Based Hyperstar Solid Polymer Electrolytes with Simultaneous Improvement of Ion Transport and Mechanical Strength. *ACS Appl. Energy Mater.* **2019,** *2*, 1608-1615.

192. Morris, M. A.; Sung, S. H.; Ketkar, P. M.; Dura, J. A.; Nieuwendaal, R. C.; Epps, T. H. Enhanced Conductivity via Homopolymer-Rich Pathways in Block Polymer-Blended Electrolytes. *Macromolecules* **2019**.

193. Irwin, M. T.; Hickey, R. J.; Xie, S.; Bates, F. S.; Lodge, T. P. Lithium Salt-Induced Microstructure and Ordering in Diblock Copolymer/Homopolymer Blends. *Macromolecules* **2016,** *49*, 4839-4849.

194. Vallée, A.; Besner, S.; Prud'Homme, J. Comparative Study of Poly(ethylene oxide) Electrolytes Made with $Li_n(CF_3SO_2)_2$, $LiCF_3SO_3$ and $LiClO_4$: Thermal Properties and Conductivity Behaviour. *Electrochim. Acta* **1992,** *37*, 1579-1583.

195. Teran, A. A.; Tang, M. H.; Mullin, S. A.; Balsara, N. P. Effect of Molecular Weight on Conductivity of Polymer Electrolytes. *Solid State Ion.* **2011,** *203*, 18-21.

196. Morioka, T.; Nakano, K.; Tominaga, Y. Ion-Conductive Properties of a Polymer Electrolyte Based on Ethylene Carbonate/Ethylene Oxide Random Copolymer. *Macromol. Rapid Commun.* **2017,** *38*, 1600652.

197. Mindemark, J.; Lacey, M. J.; Bowden, T.; Brandell, D. Beyond PEO–Alternative Host Materials for Li^+-Conducting Solid Polymer Electrolytes. *Prog. Polym. Sci.* **2018,** *81*, 114-143.

198. Villaluenga, I.; Chen, X. C.; Devaux, D.; Hallinan, D. T.; Balsara, N. P. Nanoparticle-Driven Assembly of Highly Conducting Hybrid Block Copolymer Electrolytes. *Macromolecules* **2015,** *48*, 358-364.

199. Webb, M. A.; Jung, Y.; Pesko, D. M.; Savoie, B. M.; Yamamoto, U.; Coates, G. W.; Balsara, N. P.; Wang, Z. G.; Miller, T. F. Systematic Computational and Experimental Investigation of Lithium-Ion Transport Mechanisms in Polyester-Based Polymer Electrolytes. *ACS Cent. Sci.* **2015,** *1*, 198-205.

200. Zheng, Q.; Pesko, D. M.; Savoie, B. M.; Timachova, K.; Hasan, A. L.; Smith, M. C.; Miller, T. F.; Coates, G. W.; Balsara, N. P. Optimizing Ion Transport in Polyether-Based Electrolytes for Lithium Batteries. *Macromolecules* **2018,** *51*, 2847-2858.

201. Seo, Y.; Shen, K.-H.; Brown, J. R.; Hall, L. M. Role of Solvation on Diffusion of Ions in Diblock Copolymers: Understanding the Molecular Weight Effect through Modeling. *J. Am. Chem. Soc.* **2019,** *141*, 18455-18466.

202. Gilbert, J. B.; Luo, M.; Shelton, C. K.; Rubner, M. F.; Cohen, R. E.; Epps, T. H. Determination of Lithium-Ion Distributions in Nanostructured Block Polymer Electrolyte Thin Films by X-Ray Photoelectron Spectroscopy Depth Profiling. *ACS Nano* **2015,** *9*, 512-520.

203. Gartner, T. E.; Morris, M. A.; Shelton, C. K.; Dura, J. A.; Epps, T. H. Quantifying Lithium Salt and Polymer Density Distributions in Nanostructured Ion-Conducting Block Polymers. *Macromolecules* **2018,** *51*, 1917-1926.

204. Chakraborty, S.; Jiang, X.; Hoffman, Z. J.; Sethi, G. K.; Zhu, C.; Balsara, N. P.; Villaluenga, I. Reversible Changes in the Grain Structure and Conductivity in a Block Copolymer Electrolyte. *Macromolecules* **2020,** *53*, 5455-5464.

205. Smilgies, D.-M. Scherrer Grain-Size Analysis Adapted to Grazing-Incidence Scattering with Area Detectors. *J. Appl. Crystallogr.* **2009,** *42*, 1030-1034.

206. Roe, R. J., *Methods of X-Ray and Neutron Scattering in Polymer Science*. Oxford University Press: New York, 2000.

207. Balsara, N. P.; Marques, C. M.; Garetz, B. A.; Newstein, M. C.; Gido, S. P. Anisotropy of Lamellar Block Copolymer Grains. *Phys. Rev. E* **2002,** *66*, 052802.

208. Ryu, H. J.; Fortner, D. B.; Lee, S.; Ferebee, R.; De Graef, M.; Misichronis, K.; Avgeropoulos, A.; Bockstaller, M. R. Role of Grain Boundary Defects During Grain Coarsening of Lamellar Block Copolymers. *Macromolecules* **2013,** *46*, 204-215.

209. Diederichsen, K. M.; Buss, H. G.; McCloskey, B. D. The Compensation Effect in the Vogel−Tammann−Fulcher (VTF) Equation for Polymer-Based Electrolytes. *Macromolecules* **2017,** *50*, 49-49.

210. Matsen, M. W. Kink Grain Boundaries in a Block Copolymer Lamellar Phase. *J. Chem. Phys.* **1997,** *107*, 8110-8119.

211. Shull, K. R.; Kramer, E. J.; Bates, F. S.; Rosedale, J. H. Self-Diffusion of Symmetric Diblock Copolymer Melts near the Ordering Transition. *Macromolecules* **1991,** *24*, 1383-1386.

212. Hamersky, M. W.; Tirrell, M.; Lodge, T. P. Anisotropy of Diffusion in a Lamellar Styrene−Isoprene Block Copolymer. *Langmuir* **1998,** *14*, 6974-6979.

213. Yokoyama, H. Diffusion of Block Copolymers. *Mater. Sci. Eng. R Rep.* **2006,** *53*, 199-248.

214. Yokoyama, H.; Kramer, E. J. Diffusion of Triblock Copolymers in a Spherical Domain Structure. *Macromolecules* **2000,** *33*, 954-959.

215. Yokoyama, H.; Kramer, E. J.; Fredrickson, G. H. Simulation of Diffusion of Asymmetric Diblock and Triblock Copolymers in a Spherical Domain Structure. *Macromolecules* **2000,** *33*, 2249-2257.

216. Khanna, V.; Kim, B. J.; Hexemer, A.; Mates, T. E.; Kramer, E. J.; Li, X.; Wang, J.; Hahn, S. F. Chain Architecture Effects on the Diffusion of Cylinder-Forming Block Copolymers. *Macromolecules* **2007,** *40*, 2443-2452.

217. Takahashi, H.; Laachi, N.; Hur, S.-M.; Weinheimer, C. J.; Shykind, D.; Fredrickson, G. H. Directed Self-Assembly of Laterally Confined Lamellae-Forming Diblock Copolymers: Polydispersity and Substrate Interaction Effects. *Proc. SPIE* **2012,** *8323*, 83231N.

218. Park, M.; Harrison, C.; Chaikin, P. M.; Register, R. A.; Adamson, D. H. Block Copolymer Lithography: Periodic Arrays of ~10^{11} Holes in 1 Square Centimeter. *Science* **1997,** *276*, 1401-1404.

219. Bang, J.; Jeong, U.; Ryu, D. Y.; Russell, T. P.; J Hawker, C. Block Copolymer Nanolithography: Translation of Molecular Level Control to Nanoscale Patterns. *Adv. Mater.* **2009,** *21*, 4769-4792.

220. Carter, K. R.; DiPietro, R. A.; Sanchez, M. I.; Swanson, S. A. Nanoporous Polyimides Derived from Highly Fluorinated Polyimide/Poly(propylene oxide) Copolymers. *Chem. Mater.* **2001,** *13*, 213-221.

221. Carter, K. R.; DiPietro, R. A.; Sanchez, M. I.; Russell, T. P.; Lakshmanan, P.; McGrath, J. E. Polyimide Nanofoams Based on Ordered Polyimides Derived from Poly(amic alkyl esters): PMDA/4-BDAF. *Chem. Mater.* **1997,** *9*, 105-118.

222. Li, Y.; Ito, T. Size-Exclusion Properties of Nanoporous Films Derived from Polystyrene-Poly(methyl methacrylate) Diblock Copolymers Assessed Using Direct Electrochemistry of Ferritin. *Anal. Chem.* **2009,** *81*, 851-855.

223. Rolison, D. R. Catalytic Nanoarchitectures–the Importance of Nothing and the Unimportance of Periodicity. *Science* **2003,** *299*, 1698.

224. Liu, F.; Kong, W.; Qi, C.; Zhu, L.; Xiao, F.-S. Design and Synthesis of Mesoporous Polymer-Based Solid Acid Catalysts with Excellent Hydrophobicity and Extraordinary Catalytic Activity. *ACS Catal.* **2012,** *2*, 565-572.

225. Xu, Y.; Gu, W.; Gin, D. L. Heterogeneous Catalysis Using a Nanostructured Solid Acid Resin Based on Lyotropic Liquid Crystals. *J. Am. Chem. Soc.* **2004,** *126*, 1616-1617.

226. Gupta, P.; Paul, S. Solid Acids: Green Alternatives for Acid Catalysis. *Catal. Today* **2014,** *236*, 153-170.

227. Jones, B. H.; Lodge, T. P. Nanocasting Nanoporous Inorganic and Organic Materials from Polymeric Bicontinuous Microemulsion Templates. *Polym. J.* **2012,** *44*, 131-146.

228. Choi, J. W.; Li, Z.; Black, C. T.; Sweat, D. P.; Wang, X.; Gopalan, P. Patterning at the 10 Nanometer Length Scale Using a Strongly Segregating Block Copolymer Thin Film and Vapor Phase Infiltration of Inorganic Precursors. *Nanoscale* **2016,** *8*, 11595-11601.

229. Vakifahmetoglu, C.; Zeydanli, D.; Colombo, P. Porous Polymer Derived Ceramics. *Mater. Sci. Eng. R Rep.* **2016,** *106*, 1-30.

230. Liang; George, S. M.; Weimer, A. W.; Li, N.-H.; Blackson, J. H.; Harris, J. D.; Li, P. Synthesis of a Novel Porous Polymer/Ceramic Composite Material by Low-Temperature Atomic Layer Deposition. *Chem. Mater.* **2007,** *19*, 5388-5394.

231. Yang, S. Y.; Yang, J. A.; Kim, E. S.; Jeon, G.; Oh, E. J.; Choi, K. Y.; Hahn, S. K.; Kim, J. K. Single-File Diffusion of Protein Drugs through Cylindrical Nanochannels. *ACS Nano* **2010,** *4*, 3817-3822.

232. Rzayev, J.; Hillmyer, M. A. Nanochannel Array Plastics with Tailored Surface Chemistry. *J. Am. Chem. Soc.* **2005,** *127*, 13373-13379.

233. Bailey, T. S.; Rzayev, J.; Hillmyer, M. A. Routes to Alkene and Epoxide Functionalized Nanoporous Materials from Poly(Styrene-*b*-Isoprene-*b*-Lactide) Triblock Copolymers. *Macromolecules* **2006,** *39*, 8772-8781.

234. Mao, H.; Arrechea, P. L.; Bailey, T. S.; Johnson, B. J. S.; Hillmyer, M. A. Control of Pore Hydrophilicity in Ordered Nanoporous Polystyrene Using an AB/AC Block Copolymer Blending Strategy. *Faraday Discuss.* **2005,** *128*, 149-162.

235. Hawker, C. J.; Wooley, K. L. The Convergence of Synthetic Organic and Polymer Chemistries. *Science* **2005,** *309*, 1200-1205.

236. Mao, H.; Hillmyer, M. A. Nanoporous Polystyrene by Chemical Etching of Poly(ethylene oxide) from Ordered Block Copolymers. *Macromolecules* **2005,** *38*, 4038-4039.

237. Cavicchi, K. A.; Zalusky, A. S.; Hillmyer, M. A.; Lodge, T. P. An Ordered Nanoporous Monolith from an Elastomeric Crosslinked Block Copolymer Precursor. *Macromol. Rapid Commun.* **2004,** *25*, 704-709.

238. Utroša, P.; Žagar, E.; Kovačič, S.; Pahovnik, D. Porous Polystyrene Monoliths Prepared from in Situ Simultaneous Interpenetrating Polymer Networks: Modulation of Morphology by Polymerization Kinetics. *Macromolecules* **2019,** *52*, 819-826.

239. Schulze, M. W.; Hillmyer, M. A. Tuning Mesoporosity in Cross-Linked Nanostructured Thermosets via Polymerization-Induced Microphase Separation. *Macromolecules* **2017,** *50*, 997-1007.

240. Hampu, N.; Bates, M. W.; Vidil, T.; Hillmyer, M. A. Bicontinuous Porous Nanomaterials from Block Polymers Radically Cured in the Disordered State for Size-Selective Membrane Applications. *ACS Appl. Nano Mater.* **2019,** *2*, 4567-4577.

241. Hampu, N.; Hillmyer, M. A. Molecular Engineering of Nanostructures in Disordered Block Polymers. *ACS Macro Lett.* **2020,** *16*, 26.

242. Schmidt, S. C.; Hillmyer, M. A. Synthesis and Characterization of Model Polyisoprene-Polylactide Diblock Copolymers. *Macromolecules* **1999,** *32*, 4794-4801.

243. Hanley, K. J.; Lodge, T. P.; Huang, C.-I. Phase Behavior of a Block Copolymer in Solvents of Varying Selectivity. *Macromolecules* **2000,** *33*, 5918-5931.

244. Rytlewski, P.; Zenkiewicz, M.; Malinowski, R. Influence of Dicumyl Peroxide Content on Thermal and Mechanical Properties of Polylactide. *Int. Polym. Process.* **2011,** *26*, 580-586.

245. Huang, Y.; Zhang, C.; Pan, Y.; Wang, W.; Jiang, L.; Dan, Y. Study on the Effect of Dicumyl Peroxide on Structure and Properties of Poly(lactic acid)/Natural Rubber Blend. *J. Polym. Environ.* **2013,** *21*, 375-387.

246. van Oosten, A. S. G.; Chen, X.; Chin, L.; Cruz, K.; Patteson, A. E.; Pogoda, K.; Shenoy, V. B.; Janmey, P. A. Emergence of Tissue-Like Mechanics from Fibrous Networks Confined by Close-Packed Cells. *Nature* **2019,** *573*, 96-101.

247. Seo, J.; Lutkenhaus, J. L.; Kim, J.; Hammond, P. T.; Char, K. Development of Surface Morphology in Multilayered Films Prepared by Layer-by-Layer Deposition Using Poly(acrylic acid) and Hydrophobically Modified Poly(ethylene oxide). *Macromolecules* **2007,** *40*, 4028-4036.

248. Devanand, K.; Selser, J. C. Asymptotic Behavior and Long-Range Interactions in Aqueous Solutions of Poly(ethylene oxide). *Macromolecules* **1991,** *24*, 5943-5947.

249. Muralidharan, V.; Hui, C.-Y. Stability of Nanoporous Materials. *Macromol. Rapid Commun.* **2004,** *25*, 1487-1490.

250. Jinnai, H.; Yasuda, K.; Nishi, T. Three-Dimensional Observations of Grain Boundary Morphologies in a Cylinder-Forming Block Copolymer. *Macromol. Symp.* **2006,** *245-246*, 170-174.

251. Zalusky, A. S.; Olayo-Valles, R.; Wolf, J. H.; Hillmyer, M. A. Ordered Nanoporous Polymers from Polystyrene-Polylactide Block Copolymers. *J. Am. Chem. Soc.* **2002,** *124*, 12761-12773.

252. Feng, X.; Imran, Q.; Zhang, Y.; Sixdenier, L.; Lu, X.; Kaufman, G.; Gabinet, U.; Kawabata, K.; Elimelech, M.; Osuji, C. O. Precise Nanofiltration in a Fouling-Resistant Self-Assembled Membrane with Water-Continuous Transport Pathways. *Sci. Adv.* **2019,** *5*, eaav9308.

Appendix 1. Supporting Information for Chapter 2: Morphological Impact of Segment Dispersity in Lithium Salt-Doped Poly(styrene)/Poly(ethylene oxide) Triblock Polymers

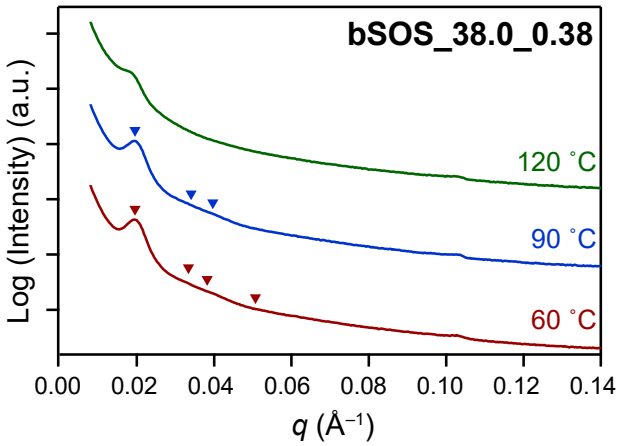

Figure A1. 1. One-dimensional $I(q)$ versus scattering wavevector q synchrotron SAXS profiles the microphase separated yet poorly ordered triblock polymer bSOS_38.0_0.38, for which higher order reflections disappear upon heating to 120 ºC. Note that the peak at q = 0.104 Å^{-1} is an artifact associated with the detector mask.

Table A1. 1. Lamellar *d*-spacings of Salt-Doped bSOS and nSOS Triblocks at *r* = 0.01.

Sample	N^a	d^b (nm)
bSOS_19.6_0.63	308	19.7
bSOS_21.2_0.70	332	20.5
bSOS_24.8_0.60	390	20.3
nSOS_19.0_0.53	300	14.1
nSOS_20.0_0.50	316	14.7
nSOS_42.6_0.47	673	23.1
nSOS_45.2_0.44	715	24.5

[a] Degree of polymerization calculated at 90 ˚C. [b] Calculated from the primary scattering peak position (q^*) at 90 ˚C using $d = 2\pi/q^*$.

Table A1. 2. Lamellar *d*-spacings of Salt-Doped bSOS and nSOS Triblocks at *r* = 0.05.

Sample	N^a	d^b (nm)
bSOS_11.6_0.63	182	13.8
bSOS_12.2_0.60	192	12.4
bSOS_12.8_0.58	202	14.2
bSOS_18.4_0.70	289	18.8
bSOS_19.6_0.66	308	20.3
bSOS_21.2_0.72	332	21.0
bSOS_23.2_0.56	366	21.1
bSOS_23.9_0.55	377	20.2
bSOS_24.8_0.63	390	21.0
nSOS_11.2_0.44	177	10.0
nSOS_19.0_0.56	300	16.6
nSOS_20.0_0.53	316	16.9
nSOS_23.2_0.46	348	18.7
nSOS_22.0_0.48	367	18.3
nSOS_42.6_0.50	673	26.9
nSOS_45.2_0.47	715	27.8

[a] Degree of polymerization calculated at 90 ˚C. [b] Calculated from the primary scattering peak position (q^*) at 90 ˚C using $d = 2\pi/q^*$.

Table A1. 3. Lamellar *d*-spacings of Salt-Doped bSOS and nSOS Triblocks with *r* = 0.09.

Sample	N^a	d^b (nm)
bSOS_11.7_0.55	185	13.6
bSOS_11.6_0.66	182	14.4
bSOS_12.2_0.63	192	12.5
bSOS_12.8_0.61	202	14.9
bSOS_18.4_0.72	289	18.7
bSOS_19.6_0.69	308	21.5
bSOS_20.9_0.65	329	21.1
bSOS_21.2_0.75	332	21.8
bSOS_23.2_0.59	366	22.3
bSOS_23.9_0.58	377	21.8
bSOS_24.8_0.65	390	21.9
nSOS_7.1_0.52	112	8.3
nSOS_8.4_0.60	132	9.1
nSOS_11.2_0.47	177	10.6
nSOS_11.8_0.45	187	10.9
nSOS_12.8_0.41	203	11.9
nSOS_15.0_0.36	239	12.7
nSOS_19.0_0.58	300	16.8
nSOS_20.0_0.56	316	16.8
nSOS_22.0_0.51	348	19.6
nSOS_23.2_0.49	367	19.4
nSOS_42.6_0.53	673	29.3
nSOS_45.2_0.50	715	30.5

[a] Degree of polymerization calculated at 90 ˚C. [b] Calculated from the primary scattering peak position (q^*) at 90 ˚C using $d = 2\pi/q^*$.

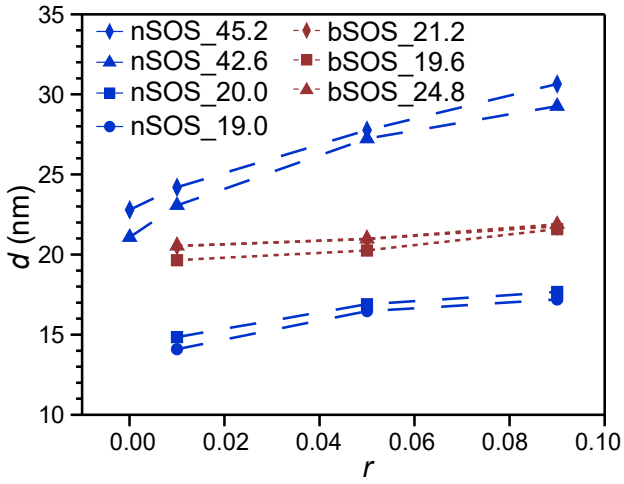

Figure A1. 2. Lamellar *d*-spacing of salt-doped bSOS and nSOS with salt loadings $0 \leq r \leq 0.09$.

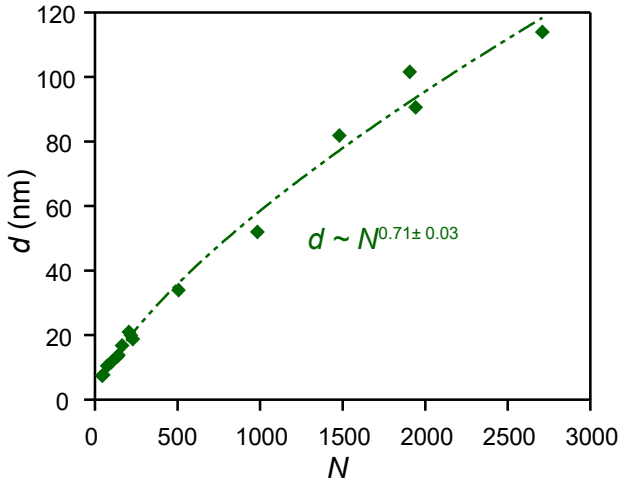

Figure A1.3. Lamellar *d*-spacing of narrow dispersity SO diblock polymers at $r = 0.085$ from Panday et al.[82] and Yuan et al.[91] The dashed line represents the fit to $d \sim N^{0.71 \pm 0.03}$.

Appendix 2. Supporting Information for Chapter 3: Ionic Conductivities of Broad Dispersity Lithium Salt-Doped Poly(styrene)/Poly(ethylene oxide) Triblock Polymers

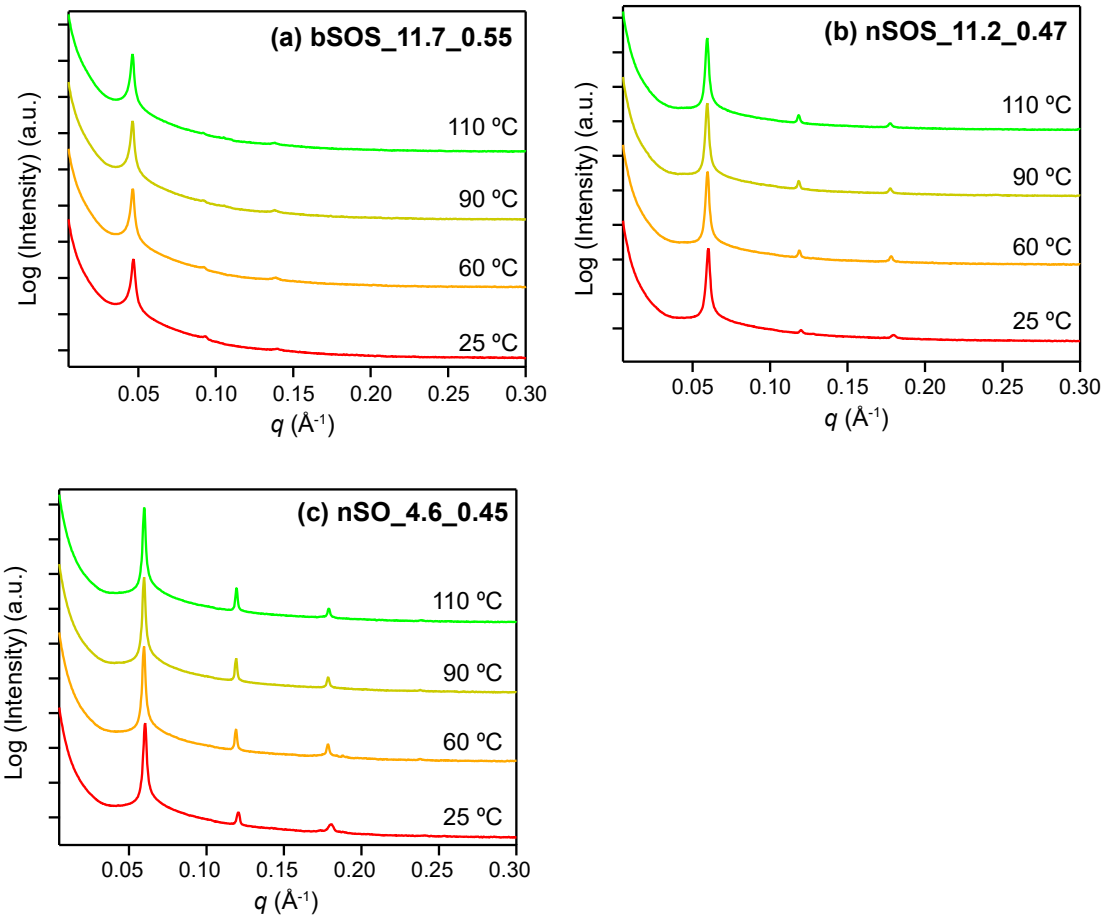

Figure A2. 1. Temperature dependent one-dimensional synchrotron SAXS patterns of the (a) bSOS_11.7_0.55 (b) nSOS_11.2_0.47 and (c) nSO_4.6_0.45 polymers in the range of 25–110 ºC showing no sign of order-disorder transition nor obvious change in peak width.

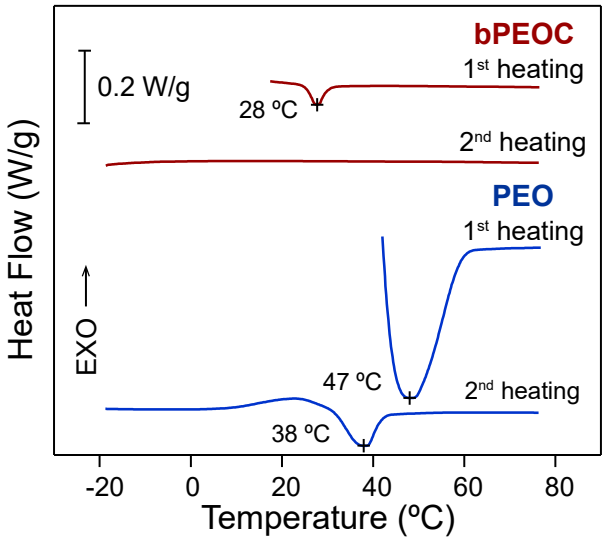

Figure A2. 2. DSC traces of the melting endotherm of salt-doped bPEOC (*red*) and PEO (*blue*) homopolymers (r = 0.09) obtained from the 1st and 2nd heating cycle at 10 ºC/min. While the melting temperatures T_m show thermal history dependence, the lower degree of crystallinity and T_m of LiTFSI-doped bPEOC compared to PEO likely originated from the presence of carbonate functional groups in the poly(ether) segment.

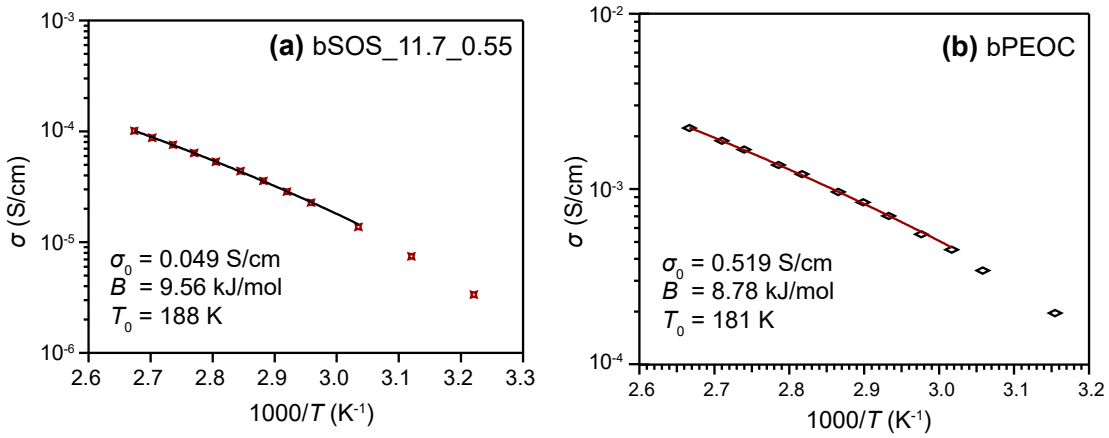

Figure A2. 3. VFT fitting of two representative conductivity results from salt-doped (a) block polymer bSOS_11.7_0.55 and (b) homopolymer bPEOC.

Table A2. 1. VFT Fitting Result from the Temperature Dependent Conductivities of the Salt-Doped Polymers

Sample	σ_0[a] (S/cm)	B[a] (kJ/mol)	T_0[b] (K)
bSOS_11.7_0.55	0.049	9.56	188
	0.094	10.02	
	0.056	9.31	
bSOS_12.8_0.60	0.073	10.63	185
	0.023	8.61	
	0.031	9.39	
bSOS_23.9_0.58	0.128	9.88	184
	0.071	8.83	
	0.098	9.45	
nSOS_11.2_0.47	0.057	9.97	186
	0.040	9.39	
	0.046	9.39	
nSOS_20.0_0.56	0.113	10.13	182
	0.055	9.49	
	0.069	9.48	
nSOS_45.2_0.50	0.177	9.45	180
	0.200	9.68	
	0.174	9.41	
nSO_4.6_0.45	0.032	9.80	186
nSO_14.4_0.48	0.036	9.20	184
bPEOC	0.519	8.78	181
	0.700	9.20	
	0.648	9.07	
PEO	0.578	8.69	179
	0.888	9.23	
	0.823	9.09	

[a] Fitted with conductivity results above 60 ºC using VFT equation. [b] T_0 is determined as $T_0 = T_g - 50$ K, where T_g is obtained via DSC from the second heating cycle at 10 ºC/min.

Appendix 3. Supporting Information of Chapter 4: Flexible Nanoporous Materials from Matrix Domain Etching of Block Polymers

Synthesis and Molecular Characterization of PS-*b*-PLA and PI-*b*-PLAdiblock polymers

Polymer Characterization. ^{1}H NMR was performed on Bruker Avance III HD 400 MHz spectrometer. Spectra were acquired in deuterated chloroform and referenced to the residue solvent peak (δ = 7.26 ppm). SEC analysis were carried on a Viscotek GPCMax System with three Agilent PLgel 10 μm Mixed-BLS columns (300 mm x 7.5 mm) and a differential refractometer, running in THF with a flow rate of 1.0 mL/min. Polymer dispersities were calculated from a polystyrene calibration curve, constructed from 10 narrow molar mass dispersity standards with M_n = 580-377,400 g/mol from Polymer Laboratories (Amherst, MA).

Polymer Synthesis. The mono hydroxyl terminated polyisoprene (**PI-OH**) was synthesized via anionic polymerization in cyclohexane at 40 ºC following the literature procedure.[242] Lactide monomers were recrystallized from acetate, dried under vacuum and stored in an argon filled glove box with [O_2] and [H_2O] < 0.2 ppm. In the glovebox, **PI-OH** (1.04 g, 0.189 mmol), lactide (4.31 g, 29.9 mmol) and tin (II) ethylhexanoate (0.0607 g, 0.150 mmol) were combined with 45 g anhydrous toluene in a 100 ml heavy wall pressure vessel. The reaction vessel was charged with a stir bar, sealed with a PTFE treaded bushing and a Viton O-ring before taken out of the glove box. The reaction was initiated in a 110 ºC oil bath and after 2 h, quenched to room temperature by flushing under tap

water. The PI-*b*-PLA block polymer was isolated by precipitating in 500 ml methanol and dried under vacuum.

Poly(styrene-*block*-lactide) (PS-*b*-PLA) block polymer was synthesized from mono hydroxyl polystyrene (**PS-OH**) via identical procedures as PI-*b*-PLA.

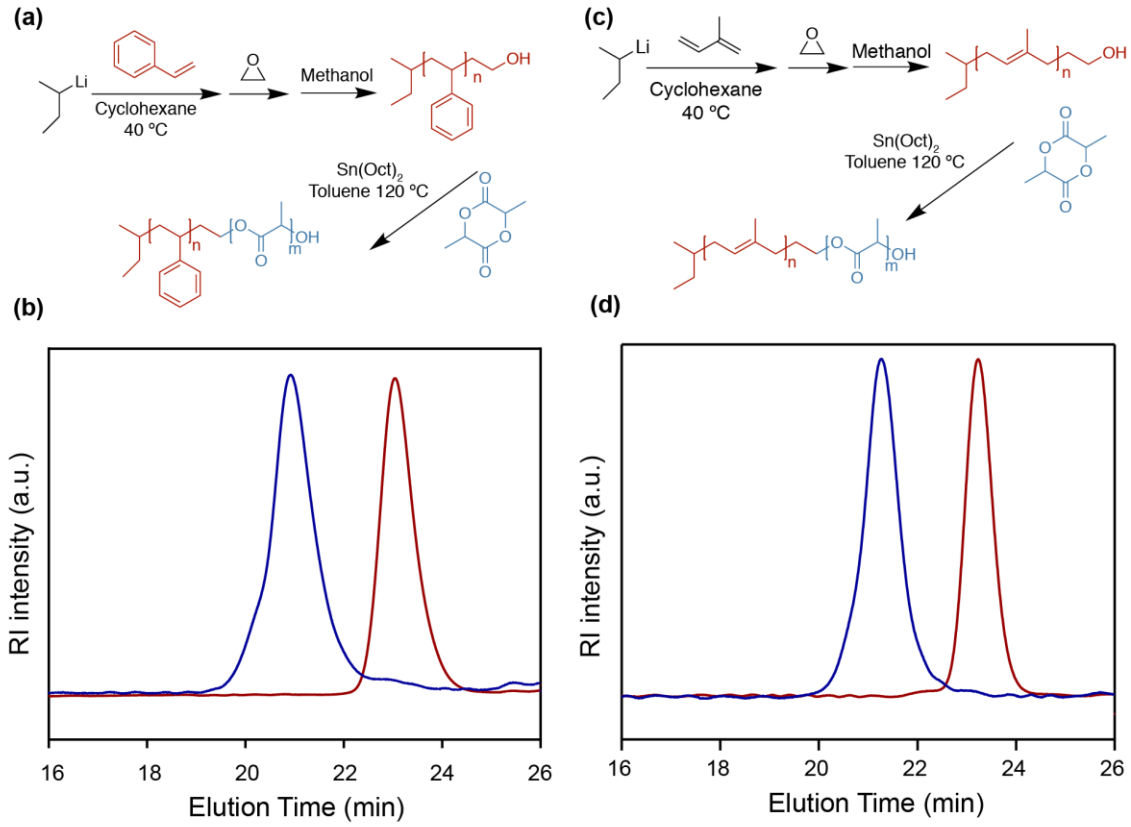

Figure A3. 1. Synthesis routes of (a) PS-*b*-PLA diblock polymer and (c) PI-*b*-PLA diblock polymer via tandem anionic and ring-opening polymerization; Overlaid SEC traces of (b) PS-OH *(red)* with $Đ = 1.03$ and PS-*b*-PLA *(blue)* with $Đ = 1.24$. and (d) PI-OH *(red)* with $Đ = 1.05$ and PI-*b*-PLA *(blue)* with $Đ = 1.17$.

Molecular Characteristics of PS-*b*-PLA. Referenced to the methyl protons on the sec-butyl end group and the methylene protons next to the hydroxyl group in the NMR pattern of **PS-OH** in Figure A3.2a, number averaged molar mass of the PS block was determined as $M_{n,PS}$ = 7.7 kg/mol based on the integral of the aromatic protons of polystyrene (6.3–7.2 ppm, 5H per repeating unit). The value of $M_{n,PS}$ closely agrees with that derived from SEC as $M_{n,PS\ (SEC)}$ = 7.5 kg/mol. Based on Figure A3.2b, molar mass of the PLA block was determined as as $M_{n,PLA}$ = 33.4 kg/mol, which is calculated from the integral of methine proton of PLA (5.1–5.3 ppm, 1H per repeating unit) referenced to the resonance of polystyrene. Thus, the total molecular weight of PS-*b*-PLA is M_n = 41.4 kg/mol as determined by NMR.

The volume fraction of the PS domain was estimated from the molar mass of PS and PLA block calculated via NMR and their room temperature densities: ρ_{PS} = 1.1 g/cm^3 and ρ_{PLA} = 1.25 g/cm^3:

$$f_{PS} = \frac{\frac{M_{n,\,PS}}{\rho_{PS}}}{\frac{M_{n,\,PS}}{\rho_{PS}} + \frac{M_{n,\,PLA}}{\rho_{PLA}}} = \frac{\frac{7.7\ kg/mol}{1.1\ g/cm^3}}{\frac{7.7\ kg/mol}{1.1\ g/cm^3} + \frac{33.4\ kg/mol}{1.25\ g/cm^3}} = 0.21$$

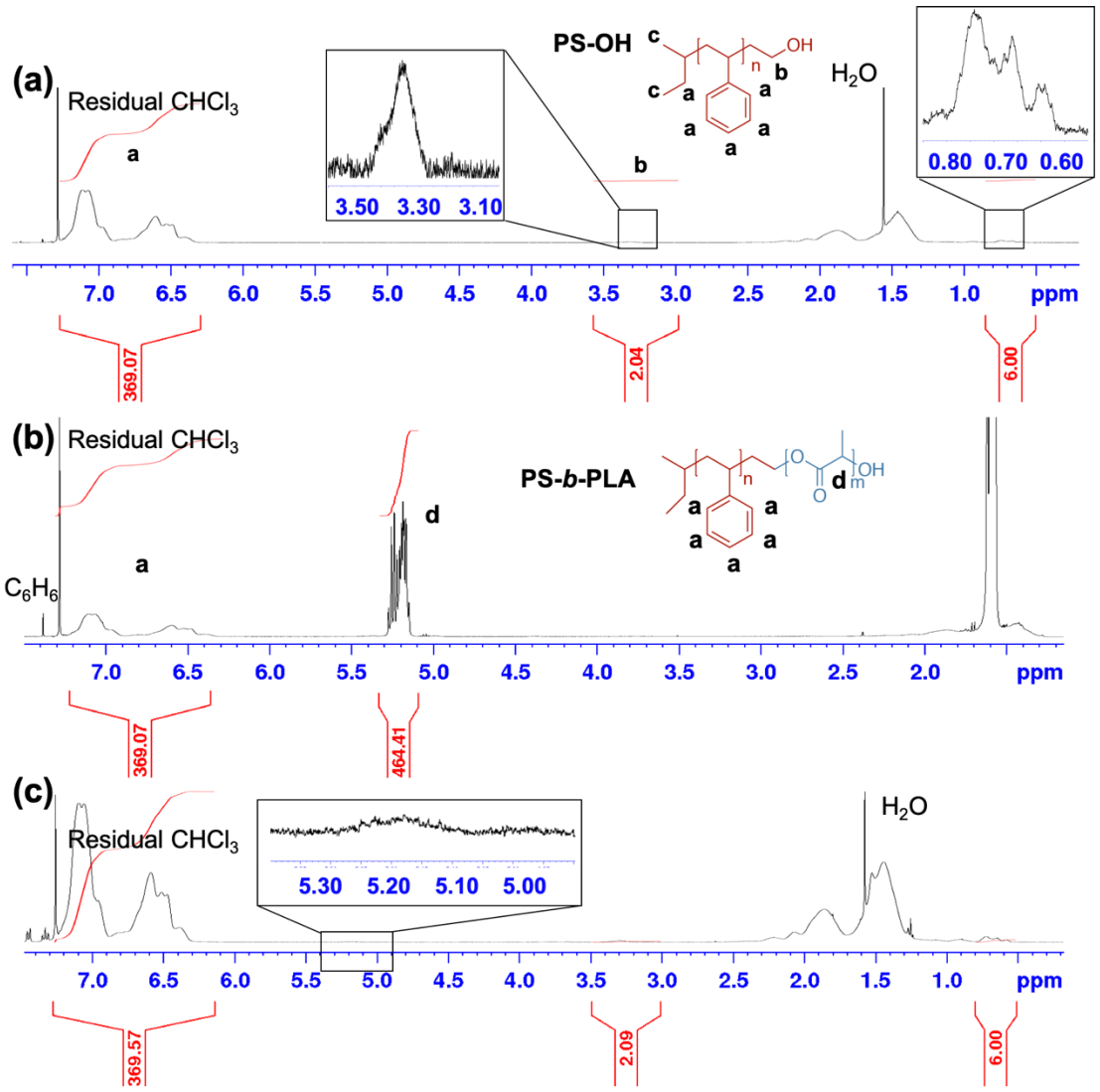

Figure A3. 2. NMR spectra of (a) PS-OH and (b) PS-*b*-PLA block polymer. The resonance signals correspond to the PS-OH end groups, aromatic protons on polystyrene and methane protons of PLA are labeled with respect to the molecular structure. Integrals of the corresponding monomer gives $M_{n,PS}$ = 7.7 kg/mol and $M_{n,PLA}$ = 33.4 kg/mol. (c) The NMR spectrum of after etched PS-*b*-PLA block polymer showing complete removal of PLA segments and the peak integrals in accordance with the PS-OH block.

Molecular Characteristics of PI-*b*-PLA. From the NMR pattern of the **PI-OH** initiating block in Figure A3.3a, number averaged molar mass of the PI block was calculated as $M_{n,PI}$ = 5.5 kg/mol from the integral of the vinylic proton resonance of polyisoprene (1,2 addition at 4.6–4.8 ppm, 2H per repeating unit and 1,4 addition at 4.9–5.4 ppm, 1H per repeating unit) referenced to the methyl protons on the sec-butyl end group and the methylene protons next to the hydroxyl group. The overlapped resonance at 4.9–5.4 ppm contributed by methine proton of PLA (1H per repeating unit) and 1,4 addition of isoprene (1H per repeating unit) in Figure A3.3b was utilized to calculate $M_{n,PLA}$ by referencing to the vinylic proton resonance of isoprene monomer with 1,2 addition at 4.6–4.8 ppm, which yields $M_{n,PLA}$ = 26.5 kg/mol and the total molecular weight of PI-*b*-PLA M_n = 32.0 kg/mol.

f_{PI} is calculated by the molar mass of the polymer segments and their densities at room temperature where ρ_{PI} = 0.9 g/cm^3 and ρ_{PLA} = 1.25 g/cm^3:

$$f_{PI} = \frac{\frac{M_{n,\,PI}}{\rho_{PI}}}{\frac{M_{n,\,PI}}{\rho_{PI}} + \frac{M_{n,\,PLA}}{\rho_{PLA}}} = \frac{\frac{5.5\ kg/mol}{0.9\ g/cm^3}}{\frac{5.5\ kg/mol}{0.9\ g/cm^3} + \frac{26.5\ kg/mol}{1.25\ g/cm^3}} = 0.22$$

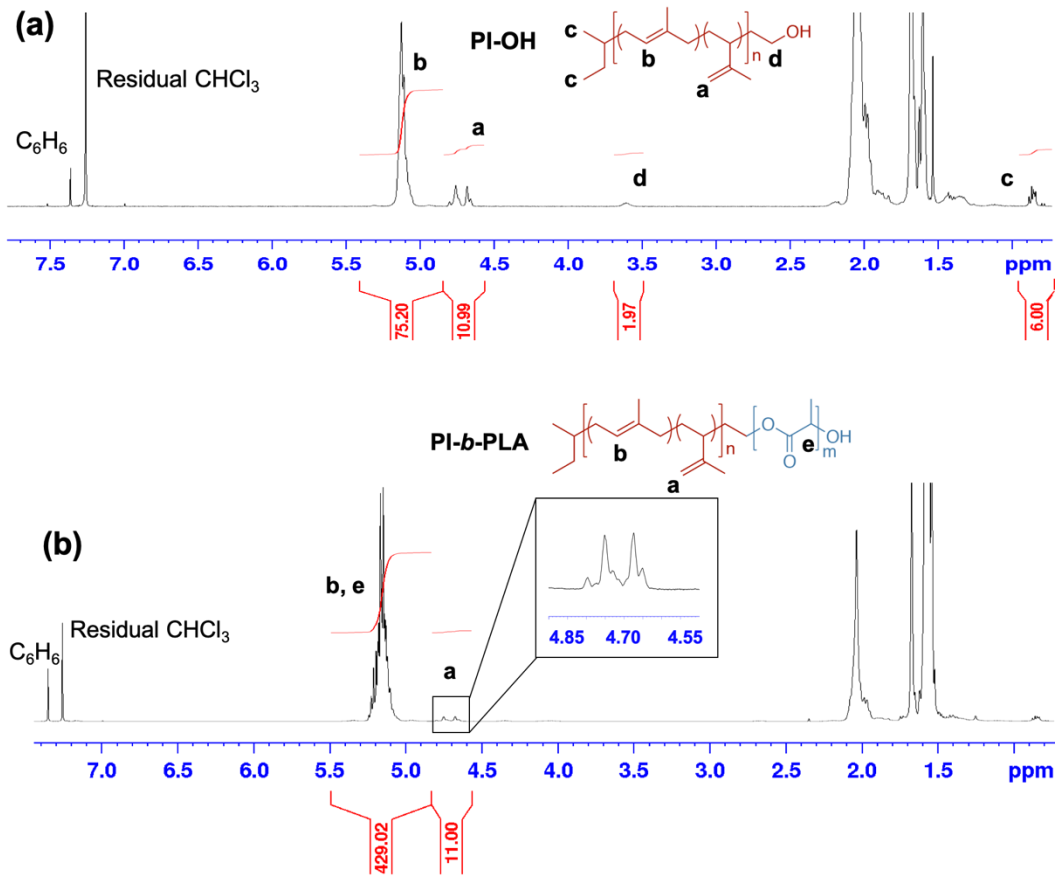

Figure A3. 3. NMR patterns of (a) PI-OH and (b) PI-b-PLA block polymer. The signals correspond to the PI-OH end groups, vinylic protons of isoprene monomers of 1,4, and 1,2 addition and methane protons of PLA are labeled accordingly.

Preparation and Characterization Methods of Polymer Samples Before and After Etching

Sample preparation. PS-*b*-PLA polymer was melt-pressed into stainless steel spacers between Teflon-coated glass fiber sheets in a melt-press (Carver Inc.) at 120 ºC at 40 psi for 1 min. Etching of the PS-*b*-PLA sample (sized 10 mm x 10 mm x 0.7 mm) was performed by immersing it in 10 mL 2.5M NaOH 80/20 (*v/v*) H_2O/MeOH solution heated at 45 ºC on a hot plate. After 12 h, the yielded PS monolith with clear and bluish appearance was washed and stored in DI water before further characterizations.

PI-*b*-PLA (1.0045 g) was mixed with 0.20 g DCP by co-dissolving in 10 g benzene and then freeze-drying the solution. Due to the sublimation of DCP under high vacuum, the ultimate DCP content of 15.7 wt% was determined via ^{1}H NMR analysis. Other polymers with [DCP] = 3.5, 5.9 and 8.6 wt% are prepared similarly by an initial DCP addition of 5, 7.5 and 10 parts per hundred PI-*b*-PLA polymer. The DCP blended PI-*b*-PLA polymer was first melt-pressed into stainless steel spacers sandwiched between Teflon-coated glass fiber fabrics in a melt-press (Carver Inc.) at 60 ºC. The sample was then heated to 155 ºC for 1 h to crosslink the PI-PLA block polymer under compression at 40 psi. The crosslinked PI-*b*-PLA polymer samples (sized 40mm x 10 mm x 0.7 mm) were immersed in 40 mL 2.5M NaOH 80/20 (*v/v*) H_2O/MeOH solution heated at 45 ºC on a hot plate for 12 h. Polymer samples with [DCP] = 8.6 wt% and 15.7 wt% yielded soft and flexible polymer strips with slightly decreased sample thickness to 0.53 ± 0.02 mm. Polymers with [DCP] ≤ 5.9 wt% remained rigid and brittle with little appearance and thickness change after immersion in the base solution. The etched samples were stored in DI water before further

characterizations. All characterizations and discussions are based on PI-*b*-PLA sample with 15.7 wt% unless otherwise noticed. Note that PI-*b*-PLA samples with thickness 1 mm was unable to be completely etched as evident from the mass loss, thus, mechanical tests are performed on samples with thickness ~ 0.5 mm. The permeation test was performed for sample of 0.35 mm thick to yield a better flux.

Small Angle X-ray Scattering. SAXS measurements were performed at 12-ID-B beamline in the Advanced Photon Source (Argonne, IL). Polymer samples were exposed to incident X-ray beam of 14.0 keV for ~1 s and the 2D-SAXS patterns were recorded on a Pilatus 2M area detector (25.4 cm × 28.9 cm active area with 1475 × 1679 pixel resolution). Corresponding one-dimensional SAXS traces with intensity $I(q)$ plotted against scattering wavevector q were obtained at the beamline and calibrated against a silver behenate standard with d = 58.38 Å.

Cyclic Compression. Before compression tests, samples were pat dried using Kimwipes to remove the excess water on the surface. The compression tests were run on an RSA-G2 rheometer using 25 mm parallel plates. As the exact height of the etched samples varies slightly around 0.53 ± 0.02 mm, the initial gap was set as 0.50 mm to ensure a complete contact between the rheometer plates and the sample. The normal force was tared to eliminate the residual stress before the compression test. Five samples with cross-sectional area of 0.48 ± 0.11 cm^2 were tested. Ten consecutive compression/release cycles were run at room temperature at strain rate 0.02 s^{-1}. Engineering stress was recalculated using the initial surface area of the etched PI-*b*-PLA sample and strain was calculated by dividing the absolute value of dislocation by the initial gap distance.

Scanning Electron Microscopy (SEM) Etched PI-*b*-PLA samples were cryofractured from liquid nitrogen, dried under dynamic vacuum, and coated with 2 nm Iridium using a sputter coater (Leica ACE600) to improve electrical conductivity. The cross-sections and surfaces of the samples were imaged by a field emission gun scanning electron microscope (SEM, Hitachi SU8230) at an accelerating voltage of 1.5 kV and a work distance of 9.6 mm.

Thermogravimetric analysis (TGA) was performed on TA Instruments Q500 under nitrogen atmosphere from room temperature to 550 ºC at a heating rate of 10 ºC/min with a sample size of ~ 5 mg.

Attenuated total reflection Fourier transform infrared spectroscopy (ATR-FTIR) was conducted on FTIR spectrometer (Thermo Nicolett 6700) with a scan resolution of 1 cm^{-1} collected over 64 scans per sample.

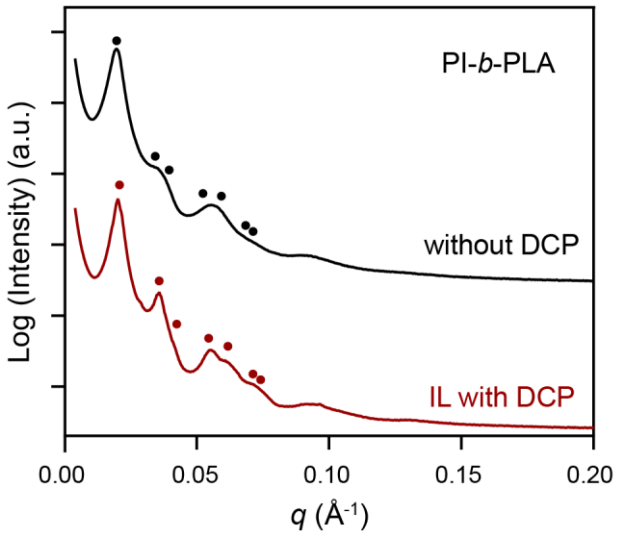

Figure A3. 4. SAXS patterns of PI-*b*-PLA block polymer showing modestly left shifted primary scattering peak from $q^* = 0.0211$ Å^{-1} to $q^* = 0.0204$ Å^{-1} after mixing with initiator DCP. Peak positions corresponding to the hexagonally packed cylinder morphology are marked by circles.

Characterization of residual PLA in etched PI-*b*-PLA sample

Due to the incorporation of large quantities of DCP initiator in the PI-*b*-PLA samples, the residual DCP and the initiation byproducts (i.e. α-cumyl alcohol) might interfere with an accurate determination of the amount of residual PLA present. To better quantify the exact mass loss of PLA, the cross-linked sample (~70 mg, cut in small pieces sized ~4 mm x 2.5 mm x 0.7 mm) was first swelled in 20 mL THF at 55 ºC for 12 h to extract the non-crosslinked moieties that is 7.8±0.7 wt% of the initial cross-linked material. ^{1}H NMR confirms the composition of the extract being mainly DCP and cumyl alcohol, with trace amount of oligo polylactide that likely generated due to partial degradation during curing at high temperatures. The absence of PI proton resonance signals indicates no loss of PI segments during the extraction, which suggests the extent of cross-linking in the PI domain is much higher than the gel point. Meanwhile, the cross-linked PI-*b*-PLA sample only swelled marginally in hot THF with increased thickness from 0.7 mm to 0.9 mm, which suggests a high extent of cross-linking. The cross-linked PI-*b*-PLA after THF extraction was excessively dried in vacuum at 45 ºC for 12 h till constant weight to remove residue THF in the polymer. Then, the cross-linked sample after extraction was etched in the same etching condition (*vide supra*), resulting in a mass loss of 80.3±0.2 wt% with respect to the mass of extracted cross-linked PI-*b*-PLA. The above extraction and etching experiments are performed on three parallel measurements.

On the basis of the 82.8 wt% PLA weight fraction in the PI-*b*-PLA, we deduce the residual PLA content in the dried npPI monolith is 12.6±0.8 wt% as calculated below:

$$residual\ PLA\ wt\% = \frac{residual\ PLA}{residual\ PLA + PI} \cdot 100\ wt\%$$

$$= \frac{82.8 - 80.3}{(82.8 - 80.3) + (100 - 80.3)} \cdot 100\ wt\% = 12.6\ wt\%$$

The amount of residual PLA corroborates with the thermogravimetric analysis (TGA) (Figure A3.5) result, showing 12 wt% weight loss corresponds to PLA residue from the dried npPI samples etched from the crosslinked diblock sample after THF extraction.

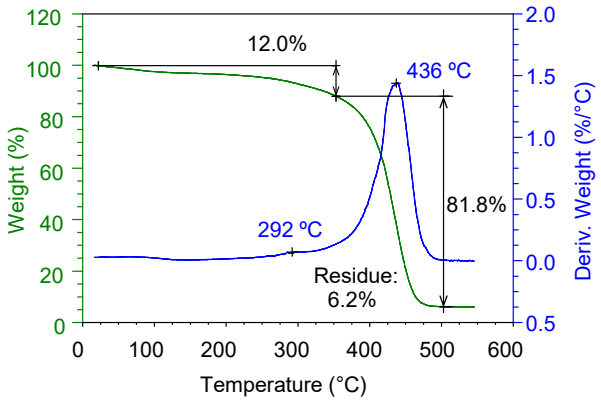

Figure A3. 5. Thermogravimetric analysis (TGA) under N_2 atmosphere of vacuum dried npPI samples etched from the crosslinked PI-*b*-PLA polymer after THF extraction. The weight loss around 436 ºC comes from the crosslinked PI domain and the weight loss below 350 ºC is attributed to the residual PLA in the dried npPI monolith.

IR spectra of cured PI, PLA, PI-*b*-PLA and the npPI monolith

PI and PLA homopolymers are mixed with DCP and cured in the same procedure as the PI-b-PLA diblock polymers. The etched and dried npPI monolith was crushed in mortar and excessively dried again in vacuum at 45 ºC for 12 h prior to IR characterization.

The cross-linking of PLA in the presence of DCP is evident by a swelled but not dissolved PLA sample in THF solution, as typically expected from a cross-linked network. From the IR spectrum, the absorption at 1685 nm^{-1} in Figure A3.6c likely originates from the carbonyl next to a 4º carbon atom due to cross-links that shifts from the initial adsorption of a linear PLA carbonyl functionality at 1750 nm^{-1} (Figure A3.6b). This adsorption is also present in Figure A3.6d for cross-linked PI-*b*-PLA as the DCP is expected to non-selectively present in both domains leading to a cross-linked PLA matrix. The IR spectrum of the dried npPI monolith (Figure A3.6e) shows a very weak adsorption at 1750 nm^{-1} that corresponds to the carbonyl function in linear PLA blocks. Rather, convoluted peaks in the range of 1500–1710 nm^{-1} that match the C=C and C=O absorptions present in cross-linked PI and PLA homopolymers corroborate with our previous expectation of residual PLA in the npPI sample after etching. On this basis, we further surmise that most PLA segments are removed through caustic etching, while the residual PLA largely stems from the tightly cross-linked PLA or covalently bound PLA segments to the PI cylinder surface that restricted its exposure to the base solution.

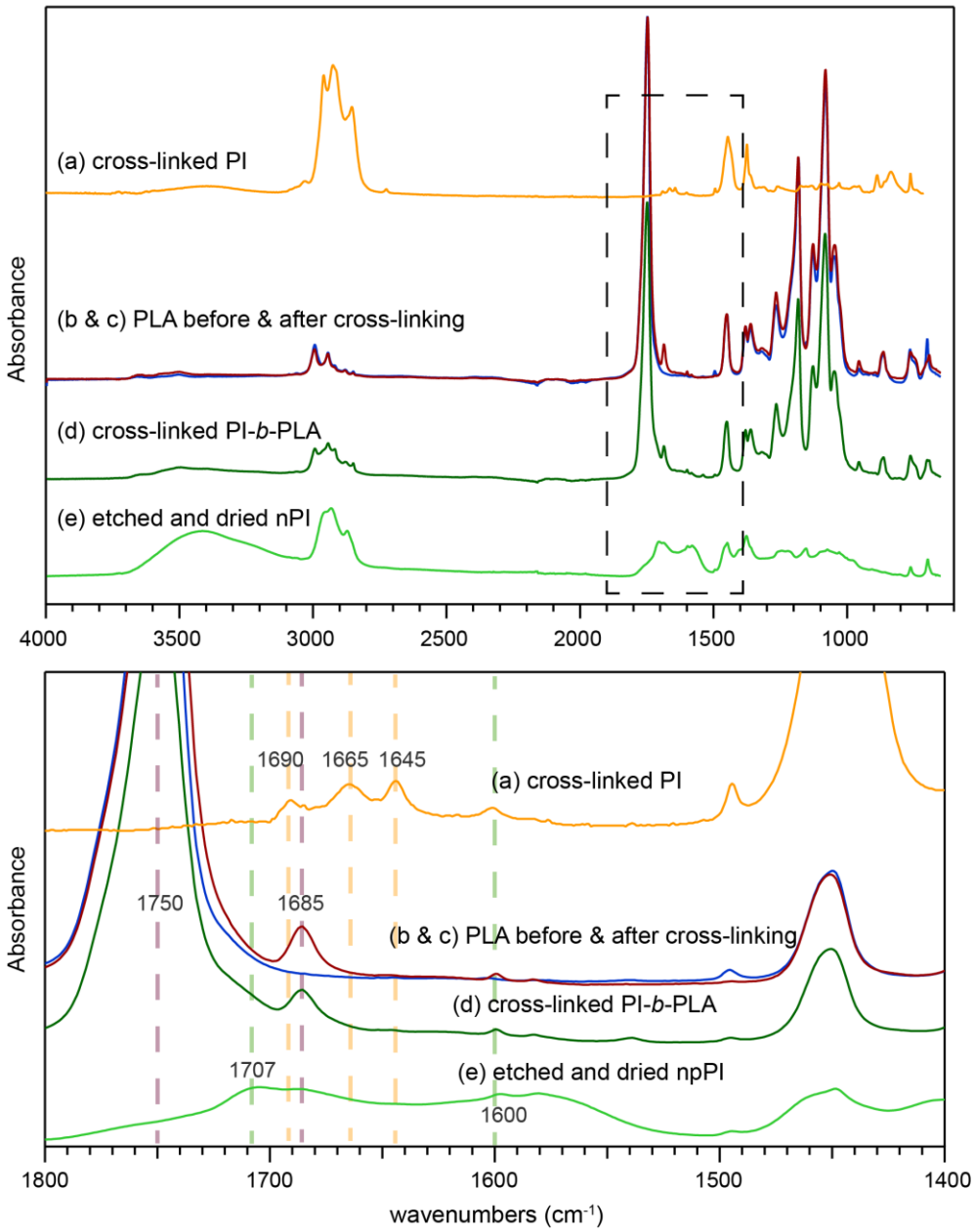

Figure A3. 6. ATR-FTIR traces of (a) cross-linked PI; PLA (b) before (*blue*) and (c) after cross-linking (*red*); (d) cured PI-*b*-PLA and (e) etched npPI sample dried under vacuum. The top diagram displays the full IR spectra of the above-mentioned samples and the bottom diagram enlarges the frequency range of 1400–1800 nm^{-1} that corresponds to C=C and C=O absorptions.

Calculation of Cylinder Diameters from the HEX Morphology

The diameter of the fibrils in the SEM image is averaged from 40 measurements sampled in Figure 4.3b via ImageJ. The result is comparable to the diameter of the PLA coated PI cylinder (d_{cyl}) after etching, which is calculated as below.

First, the diameter of the PI cylinder domain (d_{PI}) was derived from the volume fraction of the PI-*b*-PLA block polymer (f_{PI} = 0.22) and the domain spacing between (100) plane (d_{100} = 29.3 nm) based on the geometry of HEX morphology illustrated in Figure A3.7a:

$$f_{PI} = \frac{3 \cdot \pi \left(\frac{d_{PI}}{2}\right)^2}{2\sqrt{3} d_{100}^2}$$

which yields d_{PI} = 16.6 nm.

Given the content of residual PLA with respect to PI being 12.6 wt% and by assuming the residual PLA is evenly coated on the PI domain after etching, the overall diameter d_{cyl} can be related to the PLA content in the etched PI-*b*-PLA polymer sample as:

$$residual\ PLA\ wt\% = \frac{\left[\pi \left(\frac{d_{cyl}}{2}\right)^2 - \pi \left(\frac{d_{PI}}{2}\right)^2\right] * \rho_{PLA}}{\left[\pi \left(\frac{d_{cyl}}{2}\right)^2 - \pi \left(\frac{d_{PI}}{2}\right)^2\right] * \rho_{PLA} + \pi \left(\frac{d_{PI}}{2}\right)^2 * \rho_{PI}} = 12.6\ wt\%$$

which gets d_{cyl} = 17.4 nm.

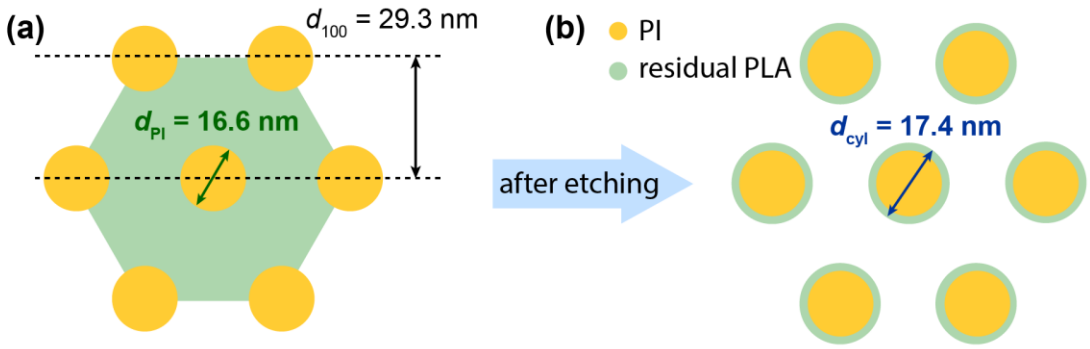

Figure A3. 7. (a)Schematic illustration showing the unit cell of hexagonally packed cylinders. The domain spacing between (100) plane (d_{110}) calculated from the primary peak scattering in SAXS and the diameter of the PI cylinder (d_{PI}) are labeled accordingly. (b) Illustration of PLA coated PI cylinder after etching.

Experimental and Characterization Details of Etched PI-*b*-PLA Polymer Applied as Semi-Permeable Membrane.

U-tube experiment set up. PI-*b*-PLA polymer sample of 0.35 mm thick and 30 mm in diameter was cured in the melt press at 155 ºC for 1hr. The polymer disk was then sandwiched between two O-rings in a U-tube. The U-tube was first filled with 2.5 M NaOH solution on both sides and immersed in a 45 ºC water bath to complete the etching process. The etching solution was then decanted and the U-tube was rinsed with DI water for 3 times to clean up the residual base. To resolve the cut-off poly(ethylene oxide) (PEO) molar mass that can pass through the etched membrane, the left arm was filled with 45 mL PEO solution in 1.0 M KOH, containing equal mass of 0.4 kDa, 1.5 kDa, 3.3 kDa, 10 kDa and 35 kDa with total concentration 30 mg/ml (6.0 mg/ml for each molar mass). The right side of the U-tube was filled with a blank solution of 1.0 M KOH solution till the same height as shown in Figure A3.8a. 1 mL aliquot was taken periodically from both sides to characterize the change of PEO concentration profile over time.

Characterization of PEO composition via SEC. The SEC analysis on PEO was carried out on an Agilent 1200 Series GPC equipped with two Viscotek I-series columns (MBMMW-3078) operating at 50 °C in *N,N*-dimethylformamide (DMF) containing 0.05 M LiBr at eluent flow rate of 1.0 mL/min. Polymer detection relied on a Wyatt Optilab T-rEX differential refractometer combined with a Wyatt DAWN HELEOS II multi-angle laser light scattering detector. To prepare the PEO samples for SEC characterization, the aqueous aliquot solutions in 1.0M KOH were first neutralized by excess trifluoro acetic acid (~ 0.17 g/mL PEO solution) to increase its solubility in the organic solvent. The

resulting PEO mixture and potassium trifluoroacetate was freeze-dried and then dissolved in the SEC mobile phase with known volume. To achieve better signals from the RI detector, aliquots from the left arm were dissolved in 1.5 mL DMF eluent (v_L = 1.5 mL) and the right arm samples were dissolved in 0.5 mL solution (v_R = 0.5 mL). The PEO/DMF solutions were sonicated for 10 mins and filtered through a 0.25 μm PTFE syringe filter before SEC characterization.

Calculation of PEO rejection. To quantify the penetration of PEO molecules through the nanoporous PI-*b*-PLA sample, the percentage rejection of each PEO molar mass (*i*) was calculated by the relative concentration of the PEO solution on each side:

$$\%\ rejection = \frac{V_L * v_L * A_{i,L}}{V_L * v_L * A_{i,L} + V_R * v_R * A_{i,R}} \times 100\ \%$$

where L and R in the subscript refers to aliquot samples taken from the left arm and right arm respectively. V_L and V_R are the volume of PEO solution in each side of the U-tube that recorded each time before taking the aliquot. As illustrated in Figure A3.8b, the level difference originates from the osmotic pressure of PEO solution that drives water diffusion towards the left arm. v_L and v_R accounts for the dilution when preparing the SEC sample and v_L = 1.5 mL, v_R = 0.5 mL. The peak area (A_i) of the SEC refractive index (RI) signal corresponds to each molar mass is directly proportional to the concentration of PEO in the SEC solution as the refractive index increment (d*n*/d*c*) does not change with PEO molar mass in the range discussed here. A_i are fitted by the multi-peak fitting package in Igor software with constant baseline and Gauss peak distributions and an example of the fitting result is shown in Figure A3.8c.

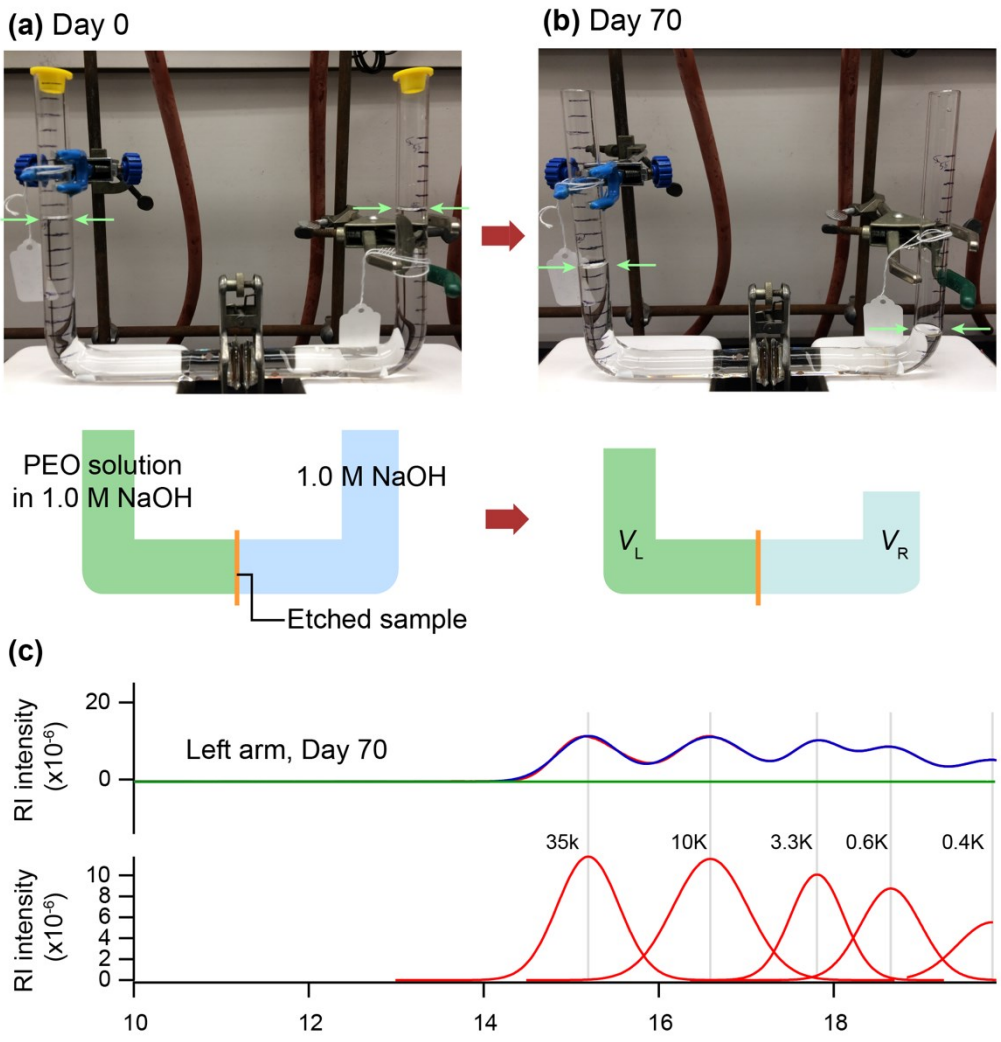

Figure A3. 8. Pictures of the experiment set up and PEO solution levels marked by green arrows on (a) day 0 and (b) day 70. (c) A representative multi-peak fitting of SEC RI trace of the aliquots taken from the left arm on Day 70. The top trace is the original RI signal overlaid with the fitting result and the bottom trace shows the convoluted peak fittings of the elution peak that corresponds to each PEO molar mass.

Calculation of Critical Molecular Radius. The critical molecular radius that can pass through the fibril networks is estimated by assuming the hexagonal symmetry is preserved locally between adjacent cylinders. Similar to the calculation for cylinder diameters in Figure A3.7, the spacing between cylinders (h) is calculated related to the void size $f_{void} \approx 0.55$ as:

$$f_{void} = \frac{3 \cdot \pi \left(\frac{d_{cyl}}{2}\right)^2}{2\sqrt{3}h^2}$$

which gives h = 19.3 nm.

From the geometry of an equilateral triangle shown in Figure A3.9, the critical radius (R_{cal}) equals to:

$$R_{cal} = \frac{2}{3}h - \frac{d_{cyl}}{2} = 4.2\ nm$$

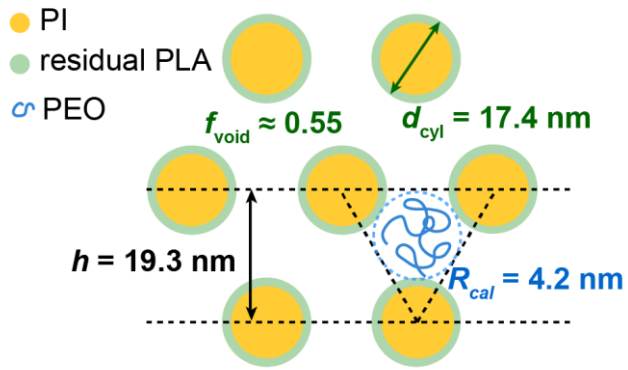

Figure A3. 9. Illustration showing the critical radius (R_{cal} = 4.2 nm) that can pass through hexagonally packed cylinders with cylinder diameter d_{cyl} = 17.4 nm and effective void fraction $f_{void} \approx 0.55$.